UNIVERSITAT DE
BARCELONA

Dynamics of nanoparticles in 3D tumor models

Rodica Alis Olea

Doctoral thesis

Dynamics of nanoparticles
in 3D tumor models

Author:

Rodica Alis Olea
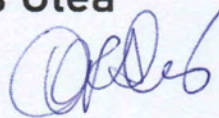
Barcelona, 2023

UNIVERSITAT DE BARCELONA

Dynamics of nanoparticles in 3D tumor models

Memoria presentada para optar al grado de doctor por la

Universitat de Barcelona

Programa de doctorado en nanociencias

Autora:

Rodica Alis Olea

Director:

Dr. Lorenzo Albertazzi

Tutor:

Dr. Josep Samitier Martí

Barcelona, 2023

UNIVERSITAT DE
BARCELONA

pentru Tata Mare

Table of Contents

Abstract

In the last decades, great research effort was focused towards designing nanocarriers for cancer therapy. However, nanoparticle translation from basic research to the clininc has proven to be a challenging task, with only a few successful nanomedicines reaching the clininc. One of the reasons for the poor outcome is that preclinical tests are often not representative for the *in vivo* environment, which comprises of several complex barriers. One of the barriers which is often overlooked is the extracellular matrix of the tumor tissue. The extracellular matrix can trap or destabilize nanocarriers not only through size filtration, but also through hydrophobic and electrostatic interactions of both positively and negatively charged surface moieties of the nanocarrier. In order to improve the nanocarrier design process, we propose a simple microfluidic chip as a model for the tumor tissue barrier, containing two types of extracellular matrix and breast cancer MCF7 spheroids. The chip is designed for testing nanocarrier penetration through ECM and cellular uptake in a 3D setting. Together with smart fluorescence reporter techniques, the chip is an important tool to assess the stability and interactions of the nanocarriers in different parts of the tumor tissue barrier, while remaining a simple and easily replicable model.

In this work, we focus on two types of polymeric nanocarriers with great potential as drug delivery systems: polymeric micelles and single chain polymeric nanoparticles. Both are self-assembly or self-folding structures containing a hydrophobic pocket which can be used for encapsulating lipophilic drugs.

We compared a set of enzymatically degradable polymeric micelles containing three widely-used hydrophilic polymers, poly (ethylene glycol) (PEG), poly (2-ethyl oxazoline) and poly (acrylic acid) – and two types of dendritic hydrophobic core. Using a coumarin fluorescent tag as reporter mechanism for micelle assembly state, we went from a basic testing of their interaction in biological media, with serum albumin and 2D cell cultures, to a more ample assessment of their behavior when encountering the tumor tissue barrier using the dual-ECM microfluidic chip. We observed similar behaviors of PEtOx and PEG, while the PAA micelles were more unstable and showed both increased ECM interaction and higher cellular uptake. Overall, we highlight the importance of the choice of hydrophilic moiety in nanocarrier design.

In the case of single chain polymeric nanoparticles, we compared a small library differing in hydrophobic, hydrophilic, and charged moieties, using covalently-bound Nile Red as a spectrally responsive reporter of SCPNs' folding state. We assessed the interactions and mobility inside the dual-ECM microfluidic chip. While the chosen SCPNs were very stable while passing through ECM, they showed very different spheroid uptake behaviors, with the more charged and hydrophilic formulations having the highest uptake.

All in all, the thesis showcases the testing of nanocarrier stability in biological media, followed by the use of a simple microfluidic platform combined with smart fluorescence reporters for assessing nanocarrier stability, ECM interactions and uptake in cellular spheroids, being important aids in the rational design of nanocarriers for drug delivery by shortening the feedback loop between formulation and testing.

Resumen en castellano

En las últimas décadas, la comunidad científica ha puesto un gran esfuerzo en el desarrollo de nanopartículas para el tratamiento contra el cáncer.[1] La translación de nanopartículas desde el laboratorio hasta el uso clínico ha presentado un gran desafío, siendo pocos los nanofármacos los que han mostrado respuestas satisfactorias. Un motivo importante es que las pruebas preclínicas no tienen en cuenta las complejas barreras que deben cruzar las nanopartículas para llegar a la zona tumoral.[2] Una de las barreras menos representada es la matriz extracelular del tejido canceroso (MEC). La matriz extracelular puede atrapar o desestabilizar las nanopartículas, no solamente filtrándolas e impidiendo su paso, pero también a través de interacciones hidrofobicas y electrostáticas de los elementos superficiales del nanoportador con carga positiva y negativa.[3,4] Para mejorar el proceso de diseño de nanopartículas, proponemos el uso de un chip microfluídico simple como modelo para la barrera del tejido tumoral, conteniendo dos tipos de matrices extracelulares y esferoides de cáncer de mama MCF7. El chip es diseñado para testar la penetración de nanopartículas a través de la MEC y dentro de las células en un entorno 3D. Junto con diferentes técnicas de fluorescencia inteligentes, el chip supondría una herramienta importante para probar la estabilidad y las interacciones de las nanopartículas en diferentes partes de la barrera, siendo al mismo tiempo un modelo fácilmente replicable.

En esta tesis, nos centramos en dos tipos de nanopartículas poliméricas con mucho potencial como sistemas de administración de fármacos: micelas poliméricas y nanopartículas poliméricas de cadena sencilla (SCPNs). Ambas son estructuras autoensamblables o autoplegables que contienen un bolsillo hidrofóbico que puede usarse para encapsular fármacos lipofílicos.

Comparamos un conjunto de micelas poliméricas degradables enzimáticamente que contienen tres polímeros hidrofílicos utilizados ampliamente: poli(etilenglicol) (PEG), poli(2-etil oxazolina) (PEtOx) y poli (ácido acrílico) (PAA), y dos tipos de núcleos hidrofóbicos dendríticos. Usando una etiqueta fluorescente de cumarina como mecanismo informador del estado de ensamblaje de las micelas, pasamos de una prueba básica de su interacción en medios biológicos, con albúmina sérica y cultivos celulares 2D, a una evaluación más amplia de su comportamiento al encontrarse con la barrera del tejido tumoral usando el chip microfluídico. Observamos comportamientos similares de PEtOx y PEG, mientras que las micelas de PAA eran más inestables y mostraban una mayor interacción con MEC y una mayor captación celular. En general, destacamos la importancia de la elección del resto hidrofílico en el diseño de nanopartículas.

En el caso de las nanopartículas poliméricas de una sola cadena, comparamos una pequeña biblioteca que difiere en los restos hidrofóbicos, hidrofílicos y cargados,

utilizando Nile Red como informador espectralmente sensible del estado de plegamiento de las SCPNs. Hemos evaluado las interacciones y la movilidad dentro del chip microfluídico. Los SCPNs elegidos fueron muy estables al pasar por MEC, pero mostraron comportamientos muy diferentes en la absorción dentro del esferoide, donde las formulaciones más cargadas e hidrofílicas tuvieron la mayor absorción.

En resumen, la tesis muestra la prueba de la interacción de nanopartículas en medios biológicos, seguida por el uso de una plataforma microfluídica simple combinado con técnicas de fluorescencia inteligentes para probar tanto la estabilidad y la penetración de nanopartículas en la MEC como la internalización de estas en esferoides celulares, siendo unas ayudas importantes en el diseño racional de nanopartículas para el transporte de fármacos, acortando el ciclo de prueba-error entre la formulación y la prueba.

(1)   Gao, J.; Karp, J. M.; Langer, R.; Joshi, N. The Future of Drug Delivery. *Chem. Mater.* **2023**, *35* (2), 359–363. https://doi.org/10.1021/acs.chemmater.2c03003.
(2)   Nichols, J. W.; Bae, Y. H. Odyssey of a Cancer Nanoparticle: From Injection Site to Site of Action. *Nano Today* **2012**, *7* (6), 606–618. https://doi.org/10.1016/j.nantod.2012.10.010.
(3)   Lieleg, O.; Baumgärtel, R. M.; Bausch, A. R. Selective Filtering of Particles by the Extracellular Matrix: An Electrostatic Bandpass. *Biophysical Journal* **2009**, *97* (6), 1569–1577. https://doi.org/10.1016/j.bpj.2009.07.009.
(4)   Witten, J.; Ribbeck, K. The Particle in the Spider's Web: Transport through Biological Hydrogels. *Nanoscale* **2017**, *9* (24), 8080–8095. https://doi.org/10.1039/C6NR09736G.

Chapter 1. Introduction

1.1. Nanoparticles in nanomedicine

Nanoparticles (NPs) are small chemical entities that can be employed for the encapsulation and transport of other molecules. Generally speaking a nanoparticle is considered to be under 100 nm.

In history, there are various examples of nanoparticles that were used by skilled artisans to create interesting color effects, such as the color-changing Lycurgus cup or stained glass windows in medieval churches, yet the use of nanoparticles has increased substantially in the last century, when several microscopy techniques became available for characterizing nano-sized structures.[1] Then, in the 1970s the first nanostructures were considered for drug delivery purposes: the use of liposomes to deliver antibiotics[2] and an implantable porous polymeric material able to release an angiogenesis blocking agent.[3] These studies pioneered the fields of nanomedicine and controlled release drug carriers. With a lot of enthusiasm and investment into nanomedicine research, there are now (in 2022) up to 100 approved nanomedicines, from several nanoparticle types.[4]
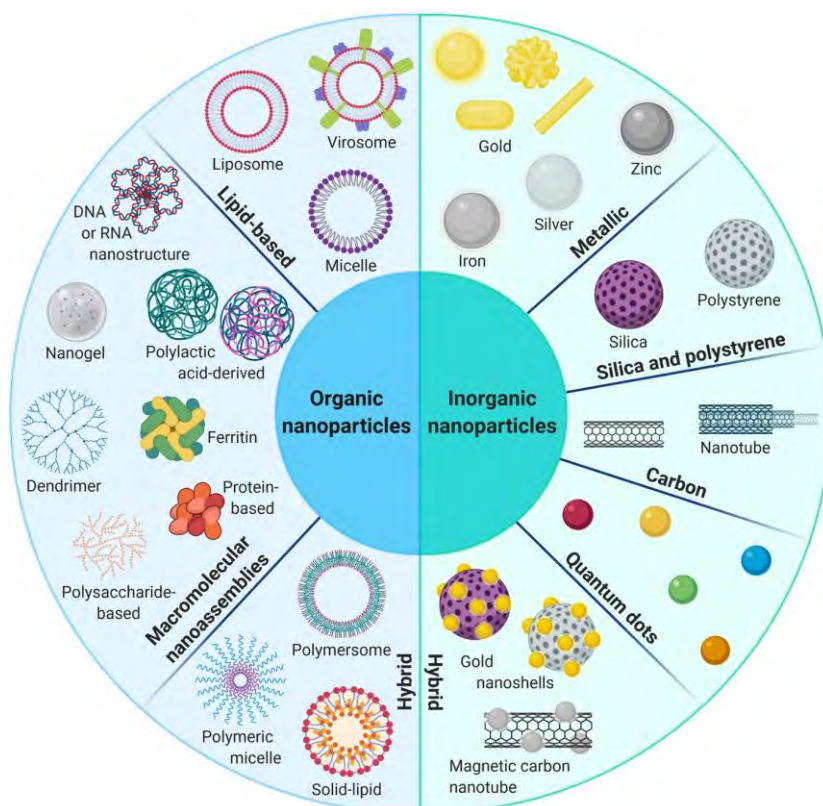
Figure 1.1. Types of nanoparticles developed for cancer therapy, based on chemical engineering. NPs generally divide between inorganic and organic. Reprinted from Briolay et al. (2021)[5] *Copyright Mol Cancer.*

Currently, there is a wide toolbox of available nanoparticles, which vary in size, shape, stiffness, porosity, charge and can be decorated with surface moieties for cell targeting and surface polymers that decrease immunogenicity (such as PEG).[6] NPs central structure can vary from the hard inorganic core, such as gold-NPs or microporous silica particles to very soft structures of organic NPs, such as liposomes, micelles or polymeric nanoassemblies to name a few (Figure 1.1).[5] Also, NPs can be highly ordered and controllable (such as dendrons or DNA cages) or heterogeneous amorphous structures (such as polylactic acid polymeric NPs).

A main difference between inorganic and organic NPs is the possible placement of functional groups, with inorganic NPs typically being functionalized on the surface, which makes them more unstable *in vivo*, while organic NPs can encapsulate molecules both in their outer shell and in their core, which is a great advantage for poorly soluble lipophilic drugs. Besides chemically engineered NPs, a series of biological agents are being developed, including exosomes, virus-like particles or oncolytic viruses.[5]

The applications of nanoparticles and nanotechnology are very diverse. For instance, nanoparticles are being developed for consolidating construction materials[7] or for cleaning water pollutants.[8] Within nanomedicine, the use of nanoparticles ranges from diagnostic tools, imaging agents, therapy complements (such as radioenhancers), to drug carriers or gene carriers. Notable NPs formulations are currently on the market in cardiology, skin care products, infectious diseases, neurological diseases, metabolic dysfunctions and oncology.[4] In 2022 there are around 100 approved nanomedicines on the market, with over 500 in clinical trials, of which half are focused on cancer.[4]

Nanoparticles as promising tools for cancer therapy

Cancer is the general term for diseases involving the uncontrolled multiplication of cells. Usually, the malignant cells have a predominant glucose metabolism,[9,10] are high energy consumers, have hijacked one or several tumor-suppressor genes and DNA repair mechanisms and appear more un-differentiated with disease progression.[11] Cancers are very different depending on location and origin tissue.[12] Generally, disease progression occurs in several steps: in the beginning there is a long lag time until a certain mass of malignant cells is formed and escapes tumor-suppressing mechanisms.[13,14] As the tumor grows, the cells in the middle receive less oxygen and nutrients, creating a necrotic core.[15,16] This leads to the promotion of blood vessel growth within the tumor (through growth factors such as VEGF).[17,18] Sometimes, the fast growth leads to the formation of „leaky vasculature" and the effect termed enhanced permeability and retention effect (EPR),[19–22] accompanied by poor lymphatic drainage (Figure 1.2). In later stages, malignant cells are known to migrate, leading to metastasis in other body locations.[23,24]
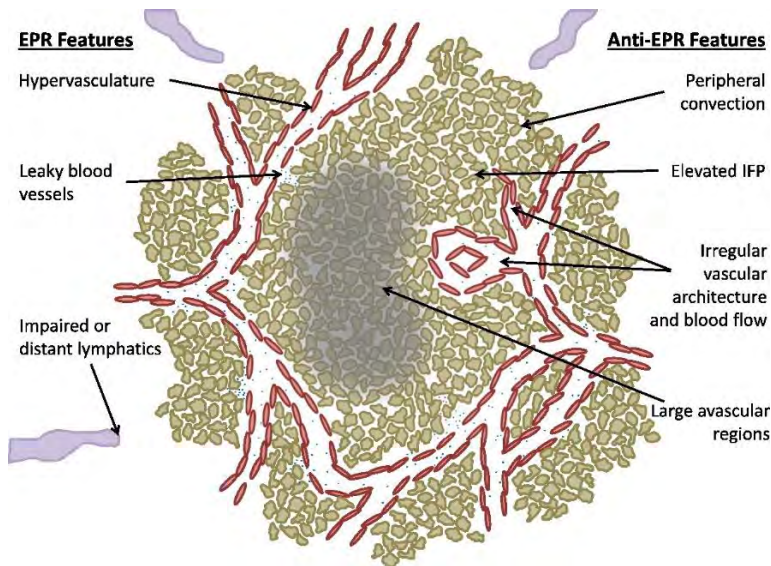
Figure 1.3. Features of the tumor tissue, related to EPR. Reprinted with permission from Nichols and Bae (2014)[20] *Copyright © 2014 Elsevier B.V.*

The current therapeutic approach consists of administering further damage to the cancer cells (which already have mutations) by chemotherapeutic drugs or radiotherapy. However, the toxic effects of chemotherapy are not localized to the cancer site, but systemic, leading to serious side-effects including nausea, pain, hair loss, skin irritations, weakened immune system, accelerated aging etc.

The promise of nanoparticles is a „targeted delivery" of the toxic drug only to the tumor tissue, avoiding unwanted targets and side-effects. However, this goal has proven much more challenging than initially expected. With a tremendous research effort in the last decades, a few successful nanomedicines have been developed for cancer therapy.[25–27] Here is a short description of such nanoformulations.

The first clinically approved nanoparticle was Doxyl, in 1995, the liposome encapsulated form of doxorubicine.[28] The original drug acts by intercalating into DNA to block cancer cell division, but causing increased heart toxicity. Doxyl alleviates the toxicity to the heart and increases circulation time.

Despite the increased scientific enthusiasm in nanomedicine after the release of Doxyl and several other liposomal formulations reaching the clinic, it took ten years for another type of nanoparticle to get clinically approved. Abraxane is an albumin-based nanoparticle encapsulating paclitaxel, approved in 2005 after showing superior results in the treatment of metastatic breast cancer.[29] Another paclitaxel nanocarrier,

Genexol-PM is based on PEG-PLA polymeric micelles,[30] being the only clinically approved polymeric NP.

In 2017, a liposome nanocarrier containing two synergistic drugs was approved for the treatment of acute myeloid leukemia, under the name of Vyxeos.[31] It releases cytarabine and danorubicin at a fixed therapeutic rate of 5:1, which would not have been possible using separate administration due to different pharmacokinetic profiles of the drugs.

Another recent nanomedicine, NBTXR3/Hensify was developed as radioenhancer. It contains hafnium oxide nanoparticles which can be localized in soft tissue sarcoma to produce an increased number of electrons during radiation therapy, correlated with increased death of tumor cell tissue.[32,33]

In recent years there has been a steady increase in the number of approved nanomedicines, which gives an optimistic outlook for the future of the field. Notably, the estimated success rate of NPs for oncology after clinical trials is 6%. Although this seems very low, for comparison, the success rate of novel cancer drugs is only 3.4%.[34] Nevertheless, an increased effort to systemize and overcome the challenges for novel targeted therapies is necessary.

What are the reasons behind the failure of the rest of 94% of nanomedicines? Several challenges can be pinpointed, including:

- Difficult scalability of more complex NP structures
- Patient heterogeneity and the lack of patient stratification – in some cases, NPs proved successful only in a subset of patients[6]
- Differences between currently employed animal models and the human disease progression
- The gap between *in vitro* 2D cell cultures and *in vivo* 3D tumor microenvironment
- The diverse testing methods used, which makes it difficult to compare different types of NPs
- Animal models typically have a fast tumor progression: mice injected with highly aggressive tumor cells develop cancer in a few weeks, compared to the very slow growth of human tumors – sometimes it takes decades before they reach a detectable size. The fast tumor growth in mouse models contributes to a more disorganized microenvironment and more likelihood of developing the EPR effect.[20]
- Small animals have a high tumor to organism size ratio: tumors grown in rodents are very large compared to the small body of the animal (10% versus 0.05% in humans), leading to a much higher blood turnover through the tumor and a higher probability that NPs encounter the tumor.[35]

A way to create a targeted therapeutic effect is using novel approaches beyond the classic paradigm of NP drug encapsulation and targeted release. The current thesis is part of such an initiative, named THERACAT that aimed to propose a novel nanotherapeutic approach based on bioorthogonal catalysis.

1.2. The THERACAT strategy: bioorthogonal catalysis for cancer therapy

The THERACAT project proposed a cancer therapy approach in two steps, using bio-orthogonal chemistry. First, a catalyst will be located at the cancer site. Then, an inactive prodrug will be administered. Only in the presence of the catalyst, the prodrug will be activated through a bioorthogonal reaction into the active drug (Figure 1.3). Thus, we could create a localized therapy, avoiding unwanted side-effects. This could allow higher doses and multiple administrations of the prodrug, thus improving the clinical output.

Within the THERACAT consortium, we had several partners working on catalyst-prodrug pairs and on different types of nanocarriers. My contribution was to create *in vitro* systems for testing such nanocarriers, for a more relevant screening and a faster feedback loop between design and application.
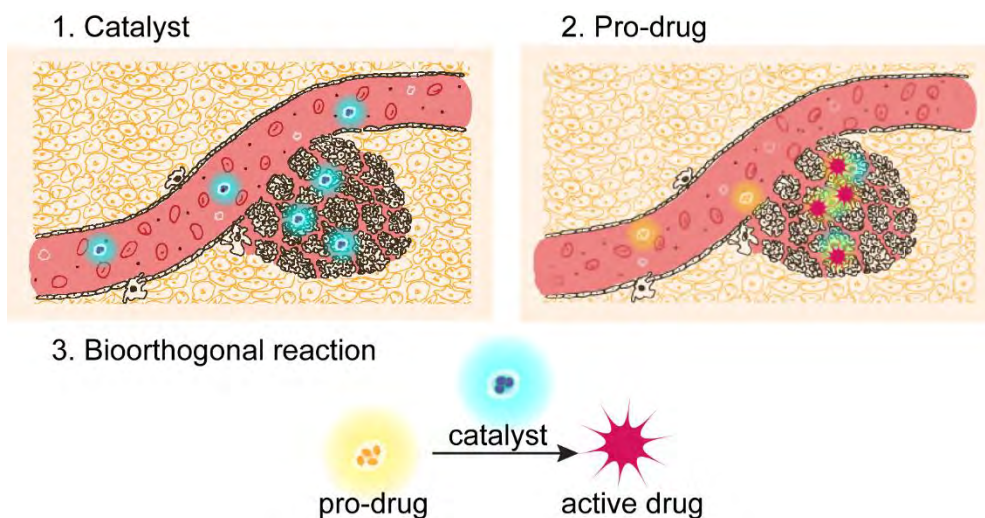
Figure 1.3. The "THERACAT" strategy: an anti-cancer therapy in two steps. First, a catalyst is administered to the tumor site (1), then an inactive pro-drug is administered (2) and activated locally by the catalyst through a bioorthogonal reaction (3), producing a targeted anti-cancer effect.

The term "bioorthogonal" refers to a reaction that does not exist naturally in the human body.[36] Bioorthogonal reactions can be fast, highly selective and produce a very high yield, even in physiological conditions, in parallel to everything that happens in the complex body environment. The group of bioorthogonal reactions partially overlaps with the bigger group of "click chemistry". Through their characteristics, bioorthogonal reactions are a novel class of promising tools with currently developing applications in imaging, diagnosis and drug delivery.[37]

One of the classes of bioorthogonal reactions are the bioorthogonal organometallic reactions (BOOM), which use a transition metal as catalyst, which can be employed within physiological conditions.[38]

An example of "applied" BOOM reaction is the conversion of an inactive prodrug of 5-fluorouracil (5FU) into the active chemotherapeutic agent using a Pd^0-resin particle as catalyst (Figure 1.4).[39] The prodrug contains a biochemically inert group that masks 5FU active sites, thus preventing unwanted toxicity. In the presence of the Pd^0-resin catalyst, extracellularly, the masking group gets cleaved with high efficiency using a BOOM reaction. Then 5FU enters the cells to produce its chemotherapeutic activity.
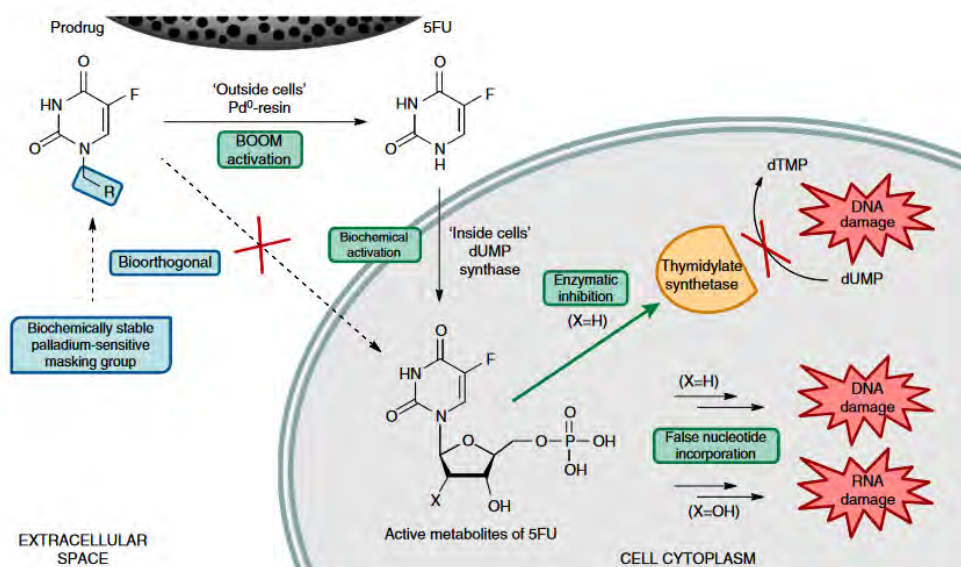
Figure 1.4. Bioorthogonal activation of a 5-fluorouracyl prodrug. An inactive 5FU prodrug is activated by a Pd^0-resin catalyst by a BOOM reaction cleaving a Pd^0 sensitive masking group, resulting in the active 5FU. The drug then enters the cell and acts through false nucleotide incorporation and enzymatic inhibition of tymidylate synthetase, resulting in DNA damage. Reprinted from Weiss et al. (2014)[39] *Copyright © 2014, Weiss et al.*

Within the THERACAT consortium, we proposed to apply the bioorthogonal chemistry approach to create a targeted cancer therapy. The therapy would consist in two distinct administration steps. Fist, a catalyst would be administered to the tumor site. Then, an inactive pro-drug would be administered, which will be activated bioorthogonally by the catalyst, creating active drugs only at the tumor site (Figure 1.3). Thus, we would obtain a localized chemotherapeutic effect. As a consequence, this could allow higher doses of pro-drug administration, which can increase the therapeutic potential. Also, multiple administrations would be possible if the catalyst remains in place.

For the first step, the administration of the catalyst, the distribution can be done intravenously – with a targeting particle design, then allowing the necessary time for clearance from the healthy tissues. Or it can be done surgically – e.g. at the site of tumor removal, for clearing remaining cancer cells – for instance within larger particles that would remain there or even in a surgical bag that can be removed afterwards. In this case, all circulation and targeting issues would be avoided.

The main challenge of the whole two-step system is to have the pro-drug and the catalyst meet inside the highly complex environment of the human body. Both need to be still viable after the interaction with the body environment to be able to perform the catalysis reaction.

In order to tackle this challenging task a comprehensive *in vitro* characterization of the nanocarrier using systems that mimic different parts of the journey through the human organism is necessary. Such characterization must include stability studies in water and in contact with biological media (serum proteins), which were addressed in **chapter 2**, as well as cellular uptake studies in a more relevant 3D setting rather than in 2D cell cultures, which were the focus of **chapters 3** and **4**. Furthermore, a lesser addressed aspect is the nanocarrier transition through ECM, which we intend to tackle in the current thesis.

1.3. The journey of nanoparticles through the body

In order to reach the target cells, such as cancer cells, nanoparticles need to surpass a series of bottlenecks,[40] illustrated in Figure 1.5. Their journey begins in the lab, where smart design and thorough characterization should lead to good formulation candidates. Notably, novel characterization techniques on single particle level can reveal the conformation and efficiency of individual particles, as well as the overall heterogeneity of the formulation.[41] Furthermore, novel tools such as microfluidic set-ups can narrow down the heterogeneous nature of nanoparticle formulations,[42] paving the way towards the personalized approach of precision medicine.[6]
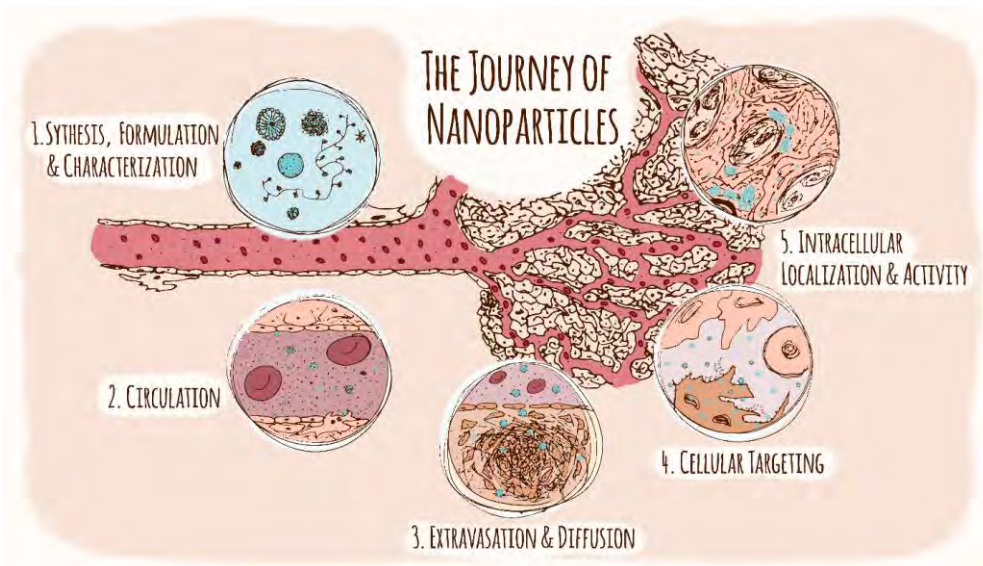
Figure 1.5. The journey of nanoparticles through the body.

There are several routes for NPs to enter the body, from surgical implantation at the disease site to intravenous injection or even oral administration. The most considered is through injecting into the bloodstream. There, NPs immediately encounter sudden dilution, high sheer stress from circulation, serum proteins that tend to attach to any colloidal particles forming the protein corona, later clearance by the kidneys and spleen or removal by the immune system to name a few. Survival time in the bloodstream was proven crucial for drug bioavailability and to allow sufficient accumulation at the target site and can be significantly increased by surface modifications of the NPs such as coating with PEG polymers.[43]

Extravasation is the next step of the journey, which should happen only at the tumor site and not in healthy tissues. Observed NPs accumulation at the tumor site was explained by the phenomenon of leaky blood vessels – enhanced permeability and retention (EPR) effect. The EPR effect sometimes plays an important role in this sense, however this was recently controversial due to differences between natively occurring human tumors to the lab-inoculated tumors in mice that are used as disease models.[20] Also, the stage and location of the tumor determine if the EPR effect can occur – usually being present in later stages, while some locations such as pancreatic tumors do not show leaky vasculature. Instead, some evidence suggests increased transcytosis through the tumor endothelial cells.[44] After extravasation, NPs encounter a dense mesh of cells and extracellular matrix (ECM). To reach the tumor core, NPs need to diffuse through ECM or, alternatively, NPs can be actively transported by the cells through transcytosis.[44–46] ECM itself can act as a filter based on NPs size, surface

charge and hydrophobicity. Also, ECM deposition contributes to the creation of high tumor interstitial fluid pressure (IFP), which can affect NPs entry and retention into the tumor tissue.[47,48] More details regarding the ECM barrier are discussed in the next section.

Once a nanocarrier enters the tissue, it should release its drug cargo only near or inside the target cells. In this regard, a wide array of NPs surface modifications and responsiveness strategies are being developed to create a „targeted delivery". Notably, current strategies are still relying on passive targeting,[49–51] where circulation time is a major limiting factor for allowing the NPs to encounter the desired cells. Antibodies, which are the typically the biological molecules with highest affinity for their target, have tumor accumulation of 1% on average, which ideally should be equaled or surpassed by NPs (while avoiding accumulation in healthy tissues).[52] NPs targeting is obtained through surface functionalization with targeting ligands. Novel strategies such as multivalency allow selecting cells with receptor overexpression or selecting cells which overexpress several receptor types.[53,54] A very important aspect in the preparation of targeted NPs is to characterize ligand functionality. In this sense, recent advances in nano-characterization techniques allow a functional evaluation of NPs targeting molecules on a single-molecule level.[55]

Ideally, tumor cell recognition by the nanocarrer should trigger the release of the drug cargo. Responsive NPs designs allow cargo release through enzymatic cleavage or as a response to redox potential or pH changes (in the acidic microenvironment of the tumor or intracellularly in the endo-lysosomal compartments) or to external stimuli such as light, ultrasound or temperature.[56] Intracellular distribution is yet another bottleneck in the NPs journey, since cells have various defensive mechanisms which are in place to protect them against viruses and unwanted intruders, which need to be surpassed for achieving intracellular activity.[5] Many strategies exist, for example cell penetrating peptides conjugated to NPs surface can mediate the escape from endo-lysosomal vesicles and direct the delivery to specific intracellular compartments.[57] However, depending on the cargo, intracellular transport may not be needed (E.g. fluorouracil drug is transported by itself, being sufficient an administration in the extracellular space).

Within THERACAT consortium there is yet another step to the nanocarrier journey: the prodrug has to meet the catalyst in order to turn into the active drug, which is not trivial considering the small size of both nano-components inside the highly complex tumor microenvironment. Although this step was not addressed during the current thesis due to time limitations, it is one of the next objectives to be tackled in the near future.

The present thesis is focused on two of the many barriers encountered by nanoparticles on their way to the target site: the stability in biological media

(circulation barrier) and the passage through tumor tissue (tissue barrier). The first is addressed in **chapter 2** and the latter in **chapters 3** and **4**.

1.4. Towards testing NPs penetration through the „tumor tissue barrier" – an in-depth focus on the extracellular matrix

Particles can get trapped inside ECM through several mechanisms based on particle size, charge and hydrophobicity.[58] Notably, the basal lamina ECM acts as a selective filter for charged particles of either sign.[59] For tumor delivery, NPs should cross basal lamina and tumor ECM. In contrast to the reticular mesh of laminin, collagen type IV and heparan sulphate of the basal lamina, the tumor ECM (in tumors with high ECM deposition) consists of disorganized fibers of collagen type I, III, V and highly hydrophilic molecules such as hyaluronic acid. To emulate these two barriers in vitro, models exist in the form of reconstituted basement membrane gels and collagen type I.

The complexity of the extracellular matrix

In the wonderfully orchestrated organization of the human body, each tissue has distinct compositions of the extracellular space. The extracellular matrix (ECM) is a mix of several types of macromolecules: proteins (collagens, fibronectin, elastin, laminin), glycosaminoglycans (GAGs, such as hyaluronic acid), proteoglycans, signaling molecules etc.[60] The most well-known role of ECM is the structural one – it gives the specific shape to each organ, supporting cells to perform their local function and providing cues for cell differentiation or migration (as can be seen in experiments with decellularized organs[61,62]). Besides the structural role, ECM has a functional role in directing and modulating the transport of nutrients and signaling molecules[63,64] and also a less understood filtering capacity. Nutrients, as well as nanoparticles and drugs can get trapped inside ECM through several mechanisms including size filtration, charge trapping and hydrophobic interactions.[58]

Biophysics of particle trapping in the ECM

The first mechanism of particle trapping is through size: particles that are larger than the ECM pore size cannot enter. If the particles are in the range of the mesh size, then penetration can be delayed due to steric hindrance, or they can enter then get stuck due to variations in pore sizes. An interesting aspect in this case is that collagen fiber deposition can confer directionality to the movement of particles along the fiber length.[65,66] Although size filtration is generally not relevant for the small sizes of nanoparticles, it depends greatly on local ECM density. For instance, studies by the

group of Kataoka showed that polymeric micelles only up to 30 nm were able to penetrate into the dense ECM of pancreatic tumor.[67]

Another way of particle trapping into ECM is through interactions with the ECM components. Due to the intrinsically disordered nature of most ECM polymers, it is difficult to know precisely the biochemical architecture of the gel (they have no crystal structure) and to precisely define the occurring forces. However, knowing the ECM composition it is possible to speculate that generally the most important interactions are the electrostatic and hydrophobic ones.[58] Van der Waal forces and hydrogen bonding are also important, but their effect being more difficult to predict, except for the hydrogen bonding shown in mucoadhesion of hydrophilic polymers such as poly(acrylic acid).[68]

An interesting study by Lieleg et al. revealed a charge-dependent filtering capacity of the basal lamina ECM: both positively charged and negatively charged liposomal particles above a certain threshold were effectively retained (Figure 1.6).[69] Furthermore, the integrity of the native ECM gel (basal lamina in this case) is crucial for the charge filtration capacity – taking independent gel components does not recapitulate this feature.
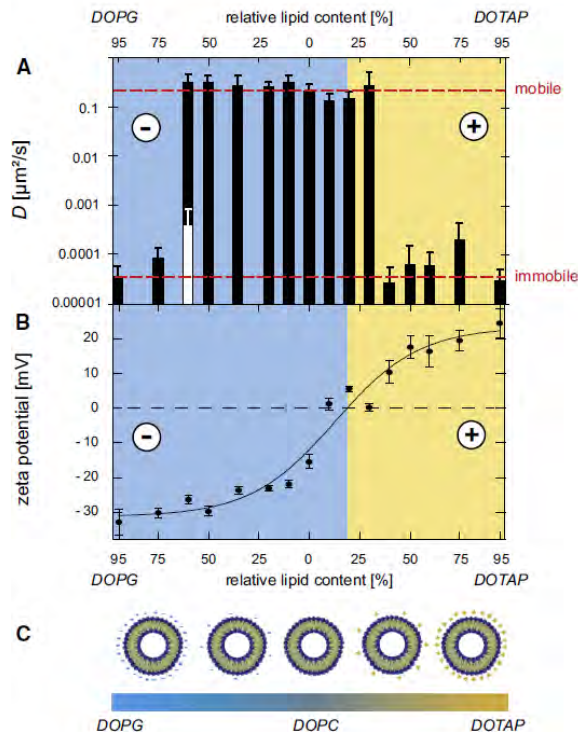
Figure 1.6. Selective filtering of charged lipidic nanoparticles in reconstituted basal lamina. Reprinted from Lieleg et al (2009)[69] *Copyright © 2009 Biophysical Society. Published by Elsevier Inc.*

This unspecific electrostatic bandpass effect is caused by the presence of charged regions within the ECM mesh: positive charges of the proteic components (for instance onto collagen) and negative charges of the glucose-amino-glycans (heparan sulphate). To the NPs, the charged gel regions appear either attractive or repulsive. Hansing et al. (2018) explained how a disordered gel – one that has attractive and repulsive forces arranged in a disorganized manner, such as the ECM in living tissues – has a much stronger trapping effect for charged particles compared to a theoretical ordered gel model (Figure 1.7).[70] Such a conceptual model, backed both by computational and experimental data, is important to consider for understanding the biophysical functionality of ECM.

Very important in determining the strength of attractive interactions is the presence of salts. The presence of ions in solution can shield the positive/negative charges of ECM, allowing the re-mobilization of trapped particles.[71]
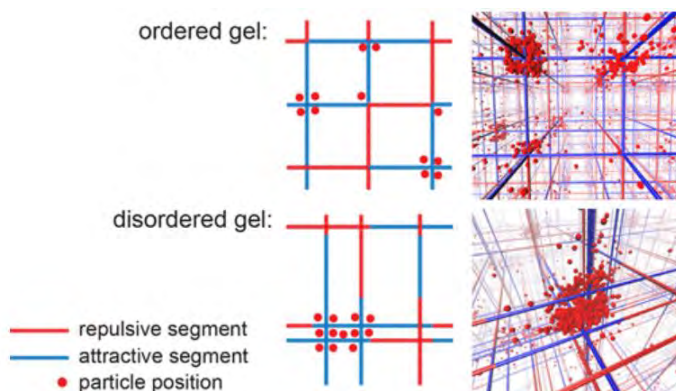
Figure 1.7. Conceptual model of particle diffusion through a polymeric mesh containing both attractive and repulsive forces. Reprinted with permission from Hansing et al. (2018)[70] *Copyright © 2018, American Chemical Society*

Overall, when reaching the ECM barrier, one of four cases can happen, as reviewed by Witten and Ribbeck (2017).[58] If the particle is larger than the ECM mesh size, it will not enter due to steric hindrance (Figure 1.8a). For smaller particles, if there is no interaction with the gel (either due to charge or hydrophobicity) the particles shall diffuse unhindered (Figure 1.8b). If a weak interaction is present, an accumulation of particles into the gel occurs, compared to solution (Figure c). In this case, gel penetration can be enhanced, with more particles partitioning into the gel than the non-interacting ones.[72] This can be desirable or not, depending on the specific nanocarrier application. If the binding is very strong, on the other hand, it causes a high accumulation at the edge of the gel, preventing subsequent penetration (Figure 1.8d).
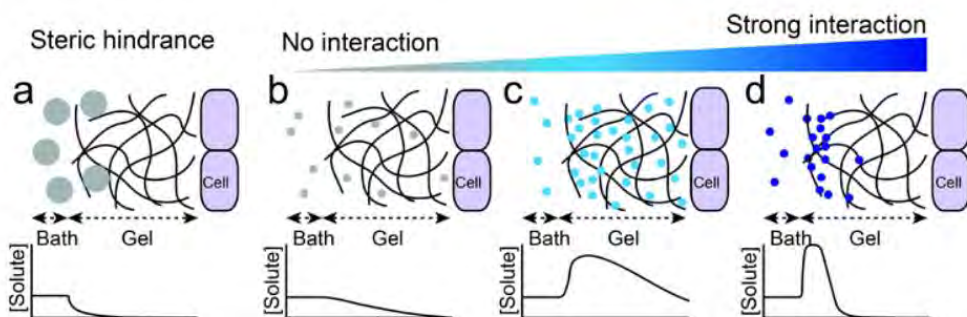
Figure 1.8. Overview of possible cases in nanoparticle gel penetration. (a) Particles larger than gel pore size cannot enter due to steric hindrance; (b) smaller particles which are inert penetrate gels through diffusion; (c) in some cases, weak interactions with the gel determine particle partitioning into the gel and faster penetration. The schematics assumes a fixed particle concentration in bath. (d) Strong interactions cause particle accumulation at the bath-gel interface while slowing the gel penetration. Reprinted with permission from Witten and Ribbeck (2017)[58] *Copyright 2017 The Royal Society of Chemistry*

Examples of ECM composition. Tumor ECM similar to "wound healing".

The extracellular matrix can vary dramatically in composition and function in different body locations.[73] For example, the ECM in the brain has a high content of glucose-amino glycans (GAGs), especially hyaluronic acid and chondroitin sulphate. In some regions, GAGs are arranged in highly regular structures termed perineuronal nets. In these regions, chondroitin sulphate proteoglycans are arranged as a "hairbrush" onto hyaluronic acid backbones, crosslinked by tenascin molecules. Chondroitin sulphate proteoglycans in the ECM bind to their homologs on the cell surfaces contributing to a tight regulation of cell behavior.[73–75]

An example on the opposite side of the stiffness regimen is the ECM of cartilages. For instance the hyaline cartilage consists mainly of fibrous collagen type II, intercalated by proteoglycans (mainly aggrecan) bound onto hyaluronic acid – which create a network capable of withstanding high compressive forces.[76] Dense and aligned collagen fibers create in this case diffusion anisotropy, directing the flow of nutrients along the fibers.[66]

On the contrary to the highly ordered ECM structures, the most typical example of ECM is the lax composition of connective tissue such as dermal tissue. Here, ECM consists mainly of proteins such as fibrillary collagens type I, III and V, elastic fibers

(consisting of elastin and fibrillins), fibronectin, tenascin C, intercalated by proteoglycans (such as collagen-binding decorin and biglycan) and GAGs such as hyaluronic acid and dermatan sulphate.[77] This loose arrangement confers the elasticity and plasticity specific to the skin.

In the body, while the cells of the connective tissue (fibroblast family) are in direct contact with collagen fibrils, the muscle and epithelial cells are separated from collagen fibrils by sheet-like structures named basal laminae.[78] Basal lamina together with the endothelial or epithelial cell layer acts as a double barrier for various macromolecules, hormones, and particles. In the skin, the barrier prevents entry of pathogens and substances from outside. In the kidney, the barrier performs the selective blood filtration function. In the brain, it makes the highly selective blood-brain barrier. In the blood vessels, the endothelium plus basal lamina prevents the entry of many blood components into the tissue, including nanoparticles. At the site of a tumor, in some cases the endothelium becomes leaky due to the EPR effect, leaving basal lamina as the sole barrier to tumor entry.[79]

As discussed in the previous section, basal lamina acts as a filter for charged particles, but what is the underlying composition that confers such selectivity? Basal lamina consists of two intertwined independent meshes: collagen type IV and laminin, bound together by several connecting molecules, the most important being enactin and the perlecan complex. Enactin is a small glycoprotein which has binding sites for both collagen IV and laminin. The perlecan complex consists of a proteic core (perlecan protein) onto which are attached 2-15 heparan sulphate side chains. The highly negatively charged heparan sulphate is the main actor for the entrapment of positively charged particles.[69,79]
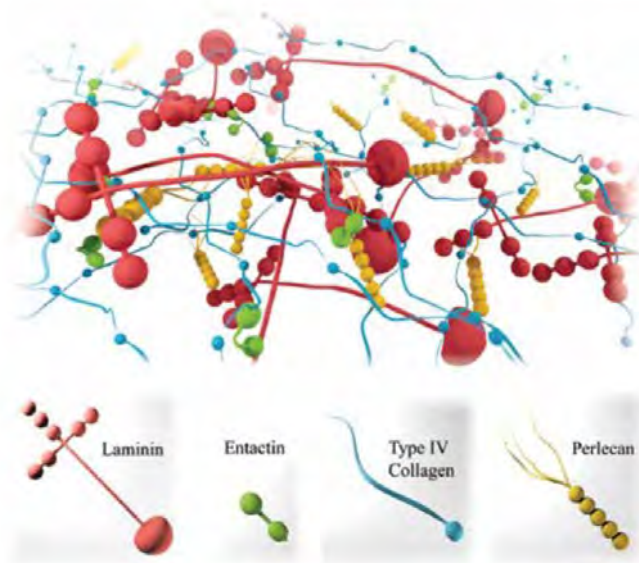
Figure 1.9. Basal lamina composition. Basal lamina consists of two intertwined meshes: collagen type IV and laminin, bound together by connecting molecules such as enactin and the perlecan complex. Reprinted from Arends and Lieleg (2016)[79] *Copyright 2016 Travascio, Arends and Lieleg. Licensee InTech.*

In addition, basal laminae contain and are transited by a series of growth factors (such as transforming growth factor beta (TGF-β), insulin-like growth factor (IGF) and fibroblast growth factor (FGF)), hormones and other signaling molecules as well as proteases such as matrix metalloproteinase-2 and 9.

Beyond the endothelium basal lamina, a solid tumor has a distinct ECM composition. Tumors with an increased deposition of ECM are named desmoplastic, such as a.o. pancreatic, breast or prostate cancer. In this case, the ECM contains mainly fibrillary collagens (type I, III, V), hyaluronic acid, fibronectin, fibulin, decorin and other components in a smaller percentage.[80] Collagen fibers are deposited in a disorganized manner, similar to wound healing sites. In wound healing, collagen fibers are produced as structural support for fibroblast tissue contraction with the purpose of closing the wound and aiding in the subsequent tissue remodeling. Hyaluronic acid is also an important component in wound healing and tumor microenvironment. Unlike the typical tissue HA which has high molecular weight and has anti-inflammatory effects, at tumor sites HA is cut into low molecular weight segments which were shown to promote inflammation, as well as cancer cell multiplication and migration by acting on HA cell surface receptors (CD44, RHAMM).[81] Increased production of high-molecular weight HA sometimes contributes in itself to cancer cell resistance, while also being a source for low-molecular weight HA (through cleavage by hyaluronidases and oxidative stress).[82] Another effect of increased HA content is a high retention of water molecules due to the hygroscopic nature of HA. This contributes, together with poor lymphatic drainage, to the creation of high intratumoral fluid pressure.[47,48] The intratumoral pressure acts two-ways: by drawing more nutrients inside the tumor (which support the increased metabolic requirements of the cancer cells) and by excluding the entry of bigger molecules (such as nanoparticles). Furthermore, intratumoral pressure was linked to increased cancer cell motility, leading to metastasis. All in all, the ECM inside solid tumors can be considered as that of a wound that does not heal.

Fundamental questions regarding ECM timeline, deposition, remodeling and ultrastructural details still remain unanswered. This is one of the reasons that makes studying NPs interactions with ECM a challenging task. The other reason is that such studies are limited to the current *in vitro* models for mimicking ECM environment.

In vitro ECM models

In an *in vitro* setting, ECM gels can be generated either by themselves or within more complex designs such as the organ-on-a-chip devices (OOAC).[83,84] OOAC are

microfluidic cell-culture devices which are intended to replicate key physiological and pathological features of human organs. The technology makes use of miniaturized architectures and controlled conditions such as flow rate, oxygen supply or tensile forces and is a very promising tool especially for drug development.[85]

Currently, the most used ECM models for *in vitro* OOAC platforms are Matrigel and collagen type I.[86] The development of Matrigel – reconstituted basement membrane from Engelbreth–Holm–Swarm (EHS) mouse sarcoma cell line,[87,88] was a tremendous breakthrough. The EHS sarcoma cells secrete a large amount of ECM very similar to basal lamina, which can support 3D *in vitro* cell growth. Thanks to Matrigel, a wide variety of cell studies in 3D became available. Limitations however arise from the innate variability of reconstituted gels and from variability in manufacturing procedures – gels produced by different companies, with slight variations in extraction protocols, can show significant differences in supporting cellular growth and in obtained gel microarchitecture.[89] Despite such limitations, for studies of particle trapping it is crucial to use a gel that preserves native filtering capabilities, since a simple mix of basal lamina components does not recapitulate its innate features.[69]

Among the single-component gels, collagen type I is by far the most studied and used gel model when it comes to *in vitro* testing platforms.[90] Collagen I gel properties, including microarchitecture, fiber thickness and tensile strength, can be easily tuned by adjusting collagen concentration, gelation temperature and pH. Obtained gels can mimic the porosity and stiffness of ECM in cancer tissues and support the observation of tumor progression, angiogenesis, cell motility or tumor-stroma interactions to name a few.

Other ECM alternatives exist on the market, from specific animal organ ECM extracts to synthetic polymer gels. However, when choosing a gel model, the gel complexity needed to maintain ECM innate particle filtering capabilities has to be balanced with the simplicity required by a versatile *in vitro* chip setup.

Importantly, thanks to the relatively simple gelation protocols, both Matrigel and collagen gels have been used inside microfluidic systems to create more complex 3D models. While many labs choose to create their own in-house 3D chips made of various materials from PDMS polymer to paper,[91] there are some commercially available models which can aid in reproducibility and ease of use. A nice example is the commercial three-channel chip from AIM Biotech, which supports a great variety of *in vitro* assays such as cancer cell invasion and migration, cell extravasation, immune interactions or angiogenesis.

In our study, we adapted the AIM Biotech chip to assess nanoparticle entry through the tumor tissue, taking into account the different ECM compositions of basal lamina and tumor environment.

Models & Methods for particle diffusion inside ECM

To study particle diffusion inside ECM, current models divide between purely gel models, *in vivo* animal studies and the *in vitro* models in-between those two, containing cells and ECM with various complexities. Typically, diffusion was studied with dextran molecules or standard gold or polystyrene nanoparticles with controlled size.

On the methods employed to study particle diffusion inside ECM, three stand out as the most common: fluorescence recovery after photobleaching (FRAP), fluorescence correlation spectroscopy (FCS) and single-particle tracking (SPT) (a few examples are shown in Table 1.1). FRAP is the oldest and simpler of the three methods.[92,93] It consists of shining a high intensity beam to a region of interest in order to bleach the fluorescent particles. Then, the recovery of fluorescence in the bleach area is recorded, extrapolating information on the diffusion of fluorescent particles. The limiting factor is the diffusion of the bleached molecules out of the bleach area, allowing the replacement with bright counterparts. If molecules are bound or interacting with other molecular species, then diffusion will be slower or reaching a plateau before complete recovery. The time window of measurable diffusion ranges from miliseconds to minutes. Although particle concentration does not directly affect the diffusion constant, typically a high concentration is required in a FRAP experiment to measure an accurate recovery.

FCS[94,95] is a more sensitive but also more complex technique. In a confocal microscope, a very small measuring volume is set. Fluorescent molecules entering or exiting the measuring volume change the overall fluorescent signal. From these small changes in signal, the diffusion rate can be determined with an autocorrelation function of the fluctuating fluorescent signal. Being able to accurately assess interactions such as protein dimerization or receptor clustering. In this case, a decreased concentration of fluorescent molecules is preferred, allowing to better distinguish distinct events of enter/exit in the measuring volume. FCS typically applies for small molecules and fast diffusion rates.

Single or multiple particle tracking[96] is a single-particle video measurement using light or fluorescence microscopy. The center of the particles is determined using a gaussian fitting and tracked over time. A mean square displacement is then calculated from the particle's movement. In this case a high dilution of the probes is required, to distinguish between single particles. Challenges arise when using this method in a 3D environment, since the probe can escape the field of view. SPT is a highly computational technique, requiring thousands of measurements for an accurate assessment of diffusion. Typically, bigger particles can be tracked better, which limits the range of sizes to 10-1000 nm, but with current advancements in microscopy, tracking becomes more and more easy also for very small probes. A worthy example

is the novel MINFlux microscopy which can track a fluorescent probe with 1 nm accuracy,[97] however this was not used on ECM up to date.

An interesting application of particle tracking is for microrheology – the biophysical mapping of nanometer-sized spaces, including the intracellular and extracellular environments. Interestingly, the influence of NPs surface charge on their ability to cross ECM was first determined of high importance for microrheological studies, which recommend PEG coating as a passivation of the NPs surface and the use of two different particles for a good microrheological study.[98]

For the ease of measurement, with the intention to create a simple model, we chose the FRAP technique in our study, considering that our nanoparticles were in the correct size range for FRAP (15-25 nm polymeric micelles and 5-10 nm SCPNs) and labeled with bleachable fluorophores (coumarin and Nile Red respectively).

Table 1.1. Studies of NPs diffusion inside ECM

Article	Diffusion molecules	ECM model	Diffusion measuring method	Comments
FCS				
Reitan, 2008[99]	IgG (150 kDa)\n\nDextrans (155kDa, 2 MDa)	5% gelatin;\n\nMulticellular spheroids	One photon FCS\n\n+ Two photon FRAP	FCS reveals anomalous or multicomponent diffusion in gel and spheroids, which are not resolvable with FRAP.
Kihara, 2013[100]	Alexa488 labeled: dextran (3 and 10)kDa, alkyne (774kDa), steptavidin, IgG	Collagen (FITC-labeled, type I) seeded with fibroblasts (TIG-1) – rearranged & condensed structures	FCS: determine the collagen condensation ratio by fibroblasts	Diffusion highly reduced by collagen rearrangement.\n\nFCS advantages: specificity of sampling space, short measurement time
Stylianopoulos 2010[101]	Quantum dots (DHLA-PEG, DHLA-PEG-NH2)	Collagen gel 9.15 mg/mL	Multiphoton FCS	Modeling the effect of repulsive electrostatic interactions

Zhang, 2015;[102] Hansing, 2016;[103] Hansing, 2018[70]	Alexa488 (net negative charge), Alexa488-NHS esther, Phycoerythrin, Rhodamins	PEG and dextran (neutral dextran, CM-dextran(−), and DEAE-dextran(+)) polymer solutions (formed with MES buffer)	FCS: dissociate the effect of size and charge (SPT discussed from other experiments)	FCS data is complemented by simulations that explain experimental data (offers several models)
FRAP				
Leddy, Gilak, 2003[104]	fluorescent dextran molecules (3, 40, 70, and 500 kDa)	Porcine articular cartilage	FRAP	3, 500kDa: 1.6–2.4 times higher D in surface. 40, 70kDa 0.2–0.3 times lower D in surface
Pluen, 2001[105]	Proteins, dextrans, liposomes	2 human tumor xenografts implanted either in the dorsal chamber or cranial window in mice	FRAP	Diffusion coefficients were related to the distribution and relative levels of collagen type I, decorin, and HA
Magzoub 2017[106]	Albumin, FITC-dextran 500kDa,	Melanoma cells injected in mice, forming a tumor	FRAP Microfiberoptic epifluorescence photobleaching: slower diffusion deeper into tumor; ECM digestion (collagenases) increased the penetration greatly	Assessment of diffusion in deep tumor: "FITC-dextran diffusion in superficial tumor (≤0.2 mm) was slowed mildly compared to that in saline (~2 to 3-fold), but greatly slowed by > 10-fold in deeper tumor (≥1 mm)." and recovery was not complete

				in deep tumor (immobile fraction)
Netti, 2000[107]	IgG	Tumors grown in mice: implanted cell lines in dorsal skinfold chamber	FRAP Interstitial diffusion coefficient measured *in situ*.	+ elastic modulus and hydraulic conductivity of tumors; correlated with presence of extra collagen
Tomasetti 2016[108]	PEG-ylated NPs (different degree) 120nm	Collagen I (5mg/mL), Matrigel (7.4 mg/mL)	FRAP (35.3 µm ROIs); and AFM for NPs structure	More PEG → faster penetration
SPT				
Godin, 2017[109]	Near-infrared luminescent single-walled carbon nanotubes (SWCNTs)	Acute brain slices from mouse	Single nanotube tracking in live brain	The nanotube is more stiff → moves slower → better for mapping extracellular space
Tada, 2007[110]	Quantum dot functionalized with anti-tumor antibody	*In vivo*: nude mouse with xenograft tumor, dorsal skinfold chamber; fast confocal imaging (3D; 30 fps), high resolution (30nm)	SPT reveals Qdot speed, direction and transport mode. Highly variable speed. Movement was "stop-and-go".	Tracking a single quantum dot through all stages from blood circulation to perinuclear localization, *in vivo*.
Mair, 2014[111]	Magnetic nanorods	Matrigel	SPT shows a biphasic transport of magnetic naorods – lateral diffusion is necessary for small ones to escape ECM "pockets"	(method-specific conclusion)
Lieleg, 2009[69]	Various size and charge: fluorescent PS-COOH 1 µm, 105nm, 50nm;	ECM reconstituted from basal membrane of mice (complex	Multiple particle tracking (diffusion coefficients from trajectories; ECM mesh size) Well defined charge threshold for passing	The ECM is an effective barrier for both positively and negatively charged particles. Uncharged

	PEGylated Latex 1.1 µm; liposomes 160-170nm (tunable surface charge),	ECM matrigel purified from the EHS sarcoma of mice) 4.55mg/mL final protein	through ECM – filtering performed by heparan sulphate chains	particles go through ECM easily. Heterogeneity in liposome formation is enough for some of them to cross and others not.
Other methods				
Li, 2016[112]	NPs: PS 40nm coupled to transferrin, PEG coating	In live cos-7 cells (no ECM)	PALM + SPT in live cells, intracellular	"Super-resolution imaging-based single particle tracking reveals dynamics of nanoparticle internalization by live cells"
Tchoryk, 2019[113]	Various sizes and surface coatings of PS particles, fluorescently labeled	Colorectal cancer spheroids,	FACS – creating a Hoechst labeling gradient to assess depth into spheroid	Penetration of non-charged particles is higher than that of charged ones. Significantly improved penetration by PEGylation

References

(1) Bayda, S.; Adeel, M.; Tuccinardi, T.; Cordani, M.; Rizzolio, F. The History of Nanoscience and Nanotechnology: From Chemical–Physical Applications to Nanomedicine. *Molecules* **2019**, *25* (1), 112. https://doi.org/10.3390/molecules25010112.

(2) Gregoriadis, G. Drug Entrapment in Liposomes. *FEBS Letters* **1973**, *36* (3), 292–296. https://doi.org/10.1016/0014-5793(73)80394-1.

(3) Langer, R.; Folkman, J. Polymers for the Sustained Release of Proteins and Other Macromolecules. *Nature* **1976**, *263* (5580), 797–800. https://doi.org/10.1038/263797a0.

(4) Shan, X.; Gong, X.; Li, J.; Wen, J.; Li, Y.; Zhang, Z. Current Approaches of Nanomedicines in the Market and Various Stage of Clinical Translation. *Acta Pharmaceutica Sinica B* **2022**, *12* (7), 3028–3048. https://doi.org/10.1016/j.apsb.2022.02.025.

(5) Briolay, T.; Petithomme, T.; Fouet, M.; Nguyen-Pham, N.; Blanquart, C.; Boisgerault, N. Delivery of Cancer Therapies by Synthetic and Bio-Inspired Nanovectors. *Molecular Cancer* **2021**, *20* (1), 55. https://doi.org/10.1186/s12943-021-01346-2.

(6) Gao, J.; Karp, J. M.; Langer, R.; Joshi, N. The Future of Drug Delivery. *Chem. Mater.* **2023**, *35* (2), 359–363. https://doi.org/10.1021/acs.chemmater.2c03003.

(7) Mohajerani, A.; Burnett, L.; Smith, J. V.; Kurmus, H.; Milas, J.; Arulrajah, A.; Horpibulsuk, S.; Abdul Kadir, A. Nanoparticles in Construction Materials and Other Applications, and Implications of Nanoparticle Use. *Materials* **2019**, *12* (19), 3052. https://doi.org/10.3390/ma12193052.

(8) Dimapilis, E. A. S.; Hsu, C.-S.; Mendoza, R. M. O.; Lu, M.-C. Zinc Oxide Nanoparticles for Water Disinfection. *Sustainable Environment Research* **2018**, *28* (2), 47–56. https://doi.org/10.1016/j.serj.2017.10.001.

(9) Warburg, O. On the Origin of Cancer Cells. *Science* **1956**, *123* (3191), 309–314. https://doi.org/10.1126/science.123.3191.309.

(10) Bose, S.; Le, A. Glucose Metabolism in Cancer. In *The Heterogeneity of Cancer Metabolism*; Le, A., Ed.; Advances in Experimental Medicine and Biology; Springer International Publishing: Cham, 2018; pp 3–12. https://doi.org/10.1007/978-3-319-77736-8_1.

(11) Baba, A. I.; Câtoi, C. TUMOR CELL MORPHOLOGY. In *Comparative Oncology*; The Publishing House of the Romanian Academy, 2007.

(12) Faubert, B.; Solmonson, A.; DeBerardinis, R. J. Metabolic Reprogramming and Cancer Progression. *Science* **2020**, *368* (6487), eaaw5473. https://doi.org/10.1126/science.aaw5473.

(13) Michor, F.; Iwasa, Y.; Nowak, M. A. Dynamics of Cancer Progression. *Nat Rev Cancer* **2004**, *4* (3), 197–205. https://doi.org/10.1038/nrc1295.

(14) Bissell, M. J.; Hines, W. C. Why Don't We Get More Cancer? A Proposed Role of the Microenvironment in Restraining Cancer Progression. *Nat Med* **2011**, *17* (3), 320–329. https://doi.org/10.1038/nm.2328.

(15) Karsch-Bluman, A.; Feiglin, A.; Arbib, E.; Stern, T.; Shoval, H.; Schwob, O.; Berger, M.; Benny, O. Tissue Necrosis and Its Role in Cancer Progression. *Oncogene* **2019**, *38* (11), 1920–1935. https://doi.org/10.1038/s41388-018-0555-y.

(16) Mukomoto, R.; Nashimoto, Y.; Terai, T.; Imaizumi, T.; Hiramoto, K.; Ino, K.; Yokokawa, R.; Miura, T.; Shiku, H. Oxygen Consumption Rate of Tumour Spheroids during Necrotic-like Core Formation. *Analyst* **2020**, *145* (19), 6342–6348. https://doi.org/10.1039/D0AN00979B.

(17) Muz, B.; de la Puente, P.; Azab, F.; Azab, A. K. The Role of Hypoxia in Cancer Progression, Angiogenesis, Metastasis, and Resistance to Therapy. *Hypoxia (Auckl)* **2015**, *3*, 83–92. https://doi.org/10.2147/HP.S93413.

(18) Madu, C. O.; Wang, S.; Madu, C. O.; Lu, Y. Angiogenesis in Breast Cancer Progression, Diagnosis, and Treatment. *Journal of Cancer* **2020**, *11* (15), 4474–4494. https://doi.org/10.7150/jca.44313.

(19) Matsumura, Y.; Maeda, H. A New Concept for Macromolecular Therapeutics in Cancer Chemotherapy: Mechanism of Tumoritropic Accumulation of Proteins and the Antitumor Agent Smancs1. *Cancer Research* **1986**, *46* (12_Part_1), 6387–6392.

(20) Nichols, J. W.; Bae, Y. H. EPR: Evidence and Fallacy. *Journal of Controlled Release* **2014**, *190*, 451–464. https://doi.org/10.1016/j.jconrel.2014.03.057.

(21) Fang, J.; Islam, W.; Maeda, H. Exploiting the Dynamics of the EPR Effect and Strategies to Improve the Therapeutic Effects of Nanomedicines by Using EPR Effect Enhancers. *Advanced Drug Delivery Reviews* **2020**, *157*, 142–160. https://doi.org/10.1016/j.addr.2020.06.005.

(22) New Insights into "Permeability" as in the Enhanced Permeability and Retention Effect of Cancer Nanotherapeutics. *ACS Nano* **2017**, *11* (10), 9567–9569. https://doi.org/10.1021/acsnano.7b07214.

(23) ElShamy, W. M.; Duhé, R. J. Overview: Cellular Plasticity, Cancer Stem Cells and Metastasis. *Cancer Letters* **2013**, *341* (1), 2–8. https://doi.org/10.1016/j.canlet.2013.06.020.

(24) Entenberg, D.; Oktay, M. H.; Condeelis, J. S. Intravital Imaging to Study Cancer Progression and Metastasis. *Nat Rev Cancer* **2023**, *23* (1), 25–42. https://doi.org/10.1038/s41568-022-00527-5.

(25) Wicki, A.; Witzigmann, D.; Balasubramanian, V.; Huwyler, J. Nanomedicine in Cancer Therapy: Challenges, Opportunities, and Clinical Applications. *Journal of Controlled Release* **2015**, *200*, 138–157. https://doi.org/10.1016/j.jconrel.2014.12.030.

(26) van der Meel, R.; Lammers, T.; Hennink, W. E. Cancer Nanomedicines: Oversold or Underappreciated? *Expert Opinion on Drug Delivery* **2017**, *14* (1), 1–5. https://doi.org/10.1080/17425247.2017.1262346.

(27) Anselmo, A. C.; Mitragotri, S. Nanoparticles in the Clinic: An Update. *Bioeng Transl Med* **2019**, *4* (3), e10143. https://doi.org/10.1002/btm2.10143.

(28) Doxil (R) - The First FDA-Approved Nano-Drug: Lessons Learned. *Journal of controlled release : official journal of the Controlled Release Society* **2012**, *160*, 117–134. https://doi.org/10.1016/j.jconrel.2012.03.020.

(29) Gradishar, W. J.; Tjulandin, S.; Davidson, N.; Shaw, H.; Desai, N.; Bhar, P.; Hawkins, M.; O'Shaughnessy, J. Phase III Trial of Nanoparticle Albumin-Bound Paclitaxel Compared with Polyethylated Castor Oil-Based Paclitaxel in Women with Breast Cancer. *J Clin Oncol* **2005**, *23* (31), 7794–7803. https://doi.org/10.1200/JCO.2005.04.937.

(30) Werner, M. E.; Cummings, N. D.; Sethi, M.; Wang, E. C.; Sukumar, R.; Moore, D. T.; Wang, A. Z. Preclinical Evaluation of Genexol-PM, a Nanoparticle Formulation of Paclitaxel, as a Novel Radiosensitizer for the Treatment of Non-Small Cell Lung Cancer. *Int J Radiat Oncol Biol Phys* **2013**, *86* (3), 463–468. https://doi.org/10.1016/j.ijrobp.2013.02.009.

(31) Krauss, A. C.; Gao, X.; Li, L.; Manning, M. L.; Patel, P.; Fu, W.; Janoria, K. G.; Gieser, G.; Bateman, D. A.; Przepiorka, D.; Shen, Y. L.; Shord, S. S.; Sheth, C. M.; Banerjee, A.; Liu, J.; Goldberg, K. B.; Farrell, A. T.; Blumenthal, G. M.; Pazdur, R. FDA Approval Summary: (Daunorubicin and Cytarabine) Liposome for Injection for the Treatment of Adults with High-Risk Acute Myeloid Leukemia. *Clinical Cancer Research* **2019**, *25* (9), 2685–2690. https://doi.org/10.1158/1078-0432.CCR-18-2990.

(32) Bonvalot, S.; Le Pechoux, C.; De Baere, T.; Kantor, G.; Buy, X.; Stoeckle, E.; Terrier, P.; Sargos, P.; Coindre, J. M.; Lassau, N.; Ait Sarkouh, R.; Dimitriu, M.; Borghi, E.; Levy, L.; Deutsch, E.; Soria, J.-C. First-in-Human Study Testing a New Radioenhancer Using Nanoparticles (NBTXR3) Activated by Radiation Therapy in Patients with Locally Advanced Soft Tissue Sarcomas. *Clin Cancer Res* **2017**, *23* (4), 908–917. https://doi.org/10.1158/1078-0432.CCR-16-1297.

(33) Bonvalot, S.; Rutkowski, P. L.; Thariat, J.; Carrère, S.; Ducassou, A.; Sunyach, M.-P.; Agoston, P.; Hong, A.; Mervoyer, A.; Rastrelli, M.; Moreno, V.; Li, R. K.; Tiangco, B.; Herraez, A. C.; Gronchi, A.; Mangel, L.; Sy-Ortin, T.; Hohenberger, P.; de Baère, T.; Le Cesne, A.; Helfre, S.; Saada-Bouzid, E.; Borkowska, A.; Anghel, R.; Co, A.; Gebhart, M.; Kantor, G.; Montero, A.; Loong, H. H.; Vergés, R.; Lapeire, L.; Dema, S.; Kacso, G.; Austen, L.; Moureau-Zabotto, L.; Servois, V.; Wardelmann, E.; Terrier, P.; Lazar, A. J.; Bovée, J. V. M. G.; Le Péchoux, C.; Papai, Z. NBTXR3, a First-in-Class Radioenhancer Hafnium Oxide Nanoparticle, plus Radiotherapy versus Radiotherapy Alone in Patients with Locally Advanced Soft-Tissue Sarcoma (Act.In.Sarc): A Multicentre, Phase 2-3, Randomised, Controlled Trial. *Lancet Oncol* **2019**, *20* (8), 1148–1159. https://doi.org/10.1016/S1470-2045(19)30326-2.

(34) Germain, M.; Caputo, F.; Metcalfe, S.; Tosi, G.; Spring, K.; Åslund, A. K. O.; Pottier, A.; Schiffelers, R.; Ceccaldi, A.; Schmid, R. Delivering the Power of Nanomedicine to Patients Today. *Journal of Controlled Release* **2020**, *326*, 164–171. https://doi.org/10.1016/j.jconrel.2020.07.007.

(35) Nichols, J. W.; Bae, Y. H. Odyssey of a Cancer Nanoparticle: From Injection Site to Site of Action. *Nano Today* **2012**, *7* (6), 606–618. https://doi.org/10.1016/j.nantod.2012.10.010.

(36) Mitry, M. M. A.; Greco, F.; Osborn, H. M. I. In Vivo Applications of Bioorthogonal Reactions: Chemistry and Targeting Mechanisms. *Chemistry – A European Journal* **2023**, *29* (20), e202203942. https://doi.org/10.1002/chem.202203942.

(37) Scinto, S. L.; Bilodeau, D. A.; Hincapie, R.; Lee, W.; Nguyen, S. S.; Xu, M.; Am Ende, C. W.; Finn, M. G.; Lang, K.; Lin, Q.; Pezacki, J. P.; Prescher, J. A.; Robillard, M. S.; Fox, J. M. Bioorthogonal Chemistry. *Nat Rev Methods Primers* **2021**, *1*, 30. https://doi.org/10.1038/s43586-021-00028-z.

(38) van de L'Isle, M. O. N.; Ortega-Liebana, M. C.; Unciti-Broceta, A. Transition Metal Catalysts for the Bioorthogonal Synthesis of Bioactive Agents. *Current Opinion in Chemical Biology* **2021**, *61*, 32–42. https://doi.org/10.1016/j.cbpa.2020.10.001.

(39) Weiss, J. T.; Dawson, J. C.; Macleod, K. G.; Rybski, W.; Fraser, C.; Torres-Sánchez, C.; Patton, E. E.; Bradley, M.; Carragher, N. O.; Unciti-Broceta, A. Extracellular Palladium-Catalysed Dealkylation of 5-Fluoro-1-Propargyl-Uracil as a Bioorthogonally Activated Prodrug Approach. *Nature Communications* **2014**, *5* (1). https://doi.org/10.1038/ncomms4277.

(40) Nichols, J. W.; Bae, Y. H. Odyssey of a Cancer Nanoparticle: From Injection Site to Site of Action. *Nano Today* **2012**, *7* (6), 606–618. https://doi.org/10.1016/j.nantod.2012.10.010.

(41) Dhiman, S.; Andrian, T.; Santiago Gonzalez, B.; E. Tholen, M. M.; Wang, Y.; Albertazzi, L. Can Super-Resolution Microscopy Become a Standard Characterization Technique for Materials Chemistry? *Chemical Science* **2022**, *13* (8), 2152–2166. https://doi.org/10.1039/D1SC05506B.

(42) Khizar, S.; Zine, N.; Errachid, A.; Jaffrezic-Renault, N.; Elaissari, A. Microfluidic-Based Nanoparticle Synthesis and Their Potential Applications. *ELECTROPHORESIS* **2022**, *43* (7–8), 819–838. https://doi.org/10.1002/elps.202100242.

(43) Owens, D. E.; Peppas, N. A. Opsonization, Biodistribution, and Pharmacokinetics of Polymeric Nanoparticles. *Int J Pharm* **2006**, *307* (1), 93–102. https://doi.org/10.1016/j.ijpharm.2005.10.010.

(44) Liu, X.; Jiang, J.; Meng, H. Transcytosis - An Effective Targeting Strategy That Is Complementary to "EPR Effect" for Pancreatic Cancer Nano Drug Delivery. *Theranostics* **2019**, *9* (26), 8018–8025. https://doi.org/10.7150/thno.38587.

(45) Zhou, Q.; Dong, C.; Fan, W.; Jiang, H.; Xiang, J.; Qiu, N.; Piao, Y.; Xie, T.; Luo, Y.; Li, Z.; Liu, F.; Shen, Y. Tumor Extravasation and Infiltration as Barriers of

Nanomedicine for High Efficacy: The Current Status and Transcytosis Strategy. *Biomaterials* **2020**, *240*, 119902. https://doi.org/10.1016/j.biomaterials.2020.119902.

(46) Pandit, S.; Dutta, D.; Nie, S. Active Transcytosis and New Opportunities for Cancer Nanomedicine. *Nat. Mater.* **2020**, *19* (5), 478–480. https://doi.org/10.1038/s41563-020-0672-1.

(47) Böckelmann, L. C.; Schumacher, U. Targeting Tumor Interstitial Fluid Pressure: Will It Yield Novel Successful Therapies for Solid Tumors? *Expert Opinion on Therapeutic Targets* **2019**, *23* (12), 1005–1014. https://doi.org/10.1080/14728222.2019.1702974.

(48) Heldin, C.-H.; Rubin, K.; Pietras, K.; Östman, A. High Interstitial Fluid Pressure — an Obstacle in Cancer Therapy. *Nat Rev Cancer* **2004**, *4* (10), 806–813. https://doi.org/10.1038/nrc1456.

(49) Bazak, R.; Houri, M.; El Achy, S.; Hussein, W.; Refaat, T. Passive Targeting of Nanoparticles to Cancer: A Comprehensive Review of the Literature. *Molecular and Clinical Oncology* **2014**, *2* (6), 904–908. https://doi.org/10.3892/mco.2014.356.

(50) Patel, J. K.; Patel, A. P. Passive Targeting of Nanoparticles to Cancer. In *Surface Modification of Nanoparticles for Targeted Drug Delivery*; Pathak, Y. V., Ed.; Springer International Publishing: Cham, 2019; pp 125–143. https://doi.org/10.1007/978-3-030-06115-9_6.

(51) Attia, M. F.; Anton, N.; Wallyn, J.; Omran, Z.; Vandamme, T. F. An Overview of Active and Passive Targeting Strategies to Improve the Nanocarriers Efficiency to Tumour Sites. *Journal of Pharmacy and Pharmacology* **2019**, *71* (8), 1185–1198. https://doi.org/10.1111/jphp.13098.

(52) Lammers, T. Macro-Nanomedicine: Targeting the Big Picture. *Journal of Controlled Release* **2019**, *294*, 372–375. https://doi.org/10.1016/j.jconrel.2018.11.031.

(53) Woythe, L.; Tito, N. B.; Albertazzi, L. A Quantitative View on Multivalent Nanomedicine Targeting. *Advanced Drug Delivery Reviews* **2021**, *169*, 1–21. https://doi.org/10.1016/j.addr.2020.11.010.

(54) Makhani, E. Y.; Zhang, A.; Haun, J. B. Quantifying and Controlling Bond Multivalency for Advanced Nanoparticle Targeting to Cells. *Nano Convergence* **2021**, *8* (1), 38. https://doi.org/10.1186/s40580-021-00288-1.

(55) Woythe, L.; Madhikar, P.; Feiner-Gracia, N.; Storm, C.; Albertazzi, L. A Single-Molecule View at Nanoparticle Targeting Selectivity: Correlating Ligand Functionality and Cell Receptor Density. *ACS Nano* **2022**, *16* (3), 3785–3796. https://doi.org/10.1021/acsnano.1c08277.

(56) Tayo, L. L. Stimuli-Responsive Nanocarriers for Intracellular Delivery. *Biophys Rev* **2017**, *9* (6), 931–940. https://doi.org/10.1007/s12551-017-0341-z.

(57) Delehanty, J. B.; Boeneman, K.; Bradburne, C. E.; Robertson, K.; Bongard, J. E.; Medintz, I. L. Peptides for Specific Intracellular Delivery and Targeting of Nanoparticles: Implications for Developing Nanoparticle-Mediated Drug

Delivery. *Therapeutic Delivery* **2010**, *1* (3), 411–433. https://doi.org/10.4155/tde.10.27.

(58) Witten, J.; Ribbeck, K. The Particle in the Spider's Web: Transport through Biological Hydrogels. *Nanoscale* **2017**, *9* (24), 8080–8095. https://doi.org/10.1039/C6NR09736G.

(59) Lieleg, O.; Baumgärtel, R. M.; Bausch, A. R. Selective Filtering of Particles by the Extracellular Matrix: An Electrostatic Bandpass. *Biophysical Journal* **2009**, *97* (6), 1569–1577. https://doi.org/10.1016/j.bpj.2009.07.009.

(60) Karamanos, N. K.; Theocharis, A. D.; Piperigkou, Z.; Manou, D.; Passi, A.; Skandalis, S. S.; Vynios, D. H.; Orian-Rousseau, V.; Ricard-Blum, S.; Schmelzer, C. E. H.; Duca, L.; Durbeej, M.; Afratis, N. A.; Troeberg, L.; Franchi, M.; Masola, V.; Onisto, M. A Guide to the Composition and Functions of the Extracellular Matrix. *The FEBS Journal* **2021**, *288* (24), 6850–6912. https://doi.org/10.1111/febs.15776.

(61) Hoshiba, T.; Lu, H.; Kawazoe, N.; Chen, G. Decellularized Matrices for Tissue Engineering. *Expert Opinion on Biological Therapy* **2010**, *10* (12), 1717–1728. https://doi.org/10.1517/14712598.2010.534079.

(62) Nakamura, N.; Kimura, T.; Kishida, A. Overview of the Development, Applications, and Future Perspectives of Decellularized Tissues and Organs. *ACS Biomater. Sci. Eng.* **2017**, *3* (7), 1236–1244. https://doi.org/10.1021/acsbiomaterials.6b00506.

(63) Tsang, K. Y.; Cheung, M. C. H.; Chan, D.; Cheah, K. S. E. The Developmental Roles of the Extracellular Matrix: Beyond Structure to Regulation. *Cell Tissue Res* **2010**, *339* (1), 93–110. https://doi.org/10.1007/s00441-009-0893-8.

(64) Huang, G.; Greenspan, D. S. ECM Roles in the Function of Metabolic Tissues. *Trends in Endocrinology & Metabolism* **2012**, *23* (1), 16–22. https://doi.org/10.1016/j.tem.2011.09.006.

(65) Stylianopoulos, T.; Diop-Frimpong, B.; Munn, L. L.; Jain, R. K. Diffusion Anisotropy in Collagen Gels and Tumors: The Effect of Fiber Network Orientation. *Biophysical Journal* **2010**, *99* (10), 3119–3128. https://doi.org/10.1016/j.bpj.2010.08.065.

(66) Travascio, F.; Gu, W. Y. ANISOTROPIC DIFFUSIVE TRANSPORT IN ANNULUS FIBROSUS: EXPERIMENTAL DETERMINATION OF THE DIFFUSION TENSOR BY FRAP TECHNIQUE. *Ann Biomed Eng* **2007**, *35* (10), 1739–1748. https://doi.org/10.1007/s10439-007-9346-2.

(67) Cabral, H.; Matsumoto, Y.; Mizuno, K.; Chen, Q.; Murakami, M.; Kimura, M.; Terada, Y.; Kano, M. R.; Miyazono, K.; Uesaka, M.; Nishiyama, N.; Kataoka, K. Accumulation of Sub-100 Nm Polymeric Micelles in Poorly Permeable Tumours Depends on Size. *Nature Nanotech* **2011**, *6* (12), 815–823. https://doi.org/10.1038/nnano.2011.166.

(68) Shaikh, R.; Raj Singh, T. R.; Garland, M. J.; Woolfson, A. D.; Donnelly, R. F. Mucoadhesive Drug Delivery Systems. *J Pharm Bioallied Sci* **2011**, *3* (1), 89–100. https://doi.org/10.4103/0975-7406.76478.

(69) Lieleg, O.; Baumgärtel, R. M.; Bausch, A. R. Selective Filtering of Particles by the Extracellular Matrix: An Electrostatic Bandpass. *Biophysical Journal* **2009**, *97* (6), 1569–1577. https://doi.org/10.1016/j.bpj.2009.07.009.

(70) Hansing, J.; Duke, J. R.; Fryman, E. B.; DeRouchey, J. E.; Netz, R. R. Particle Diffusion in Polymeric Hydrogels with Mixed Attractive and Repulsive Interactions. *Nano Lett.* **2018**, *18* (8), 5248–5256. https://doi.org/10.1021/acs.nanolett.8b02218.

(71) Hansing, J.; Ciemer, C.; Kim, W. K.; Zhang, X.; DeRouchey, J. E.; Netz, R. R. Nanoparticle Filtering in Charged Hydrogels: Effects of Particle Size, Charge Asymmetry and Salt Concentration. *Eur Phys J E Soft Matter* **2016**, *39* (5), 53. https://doi.org/10.1140/epje/i2016-16053-2.

(72) Bajpayee, A. G.; Quadir, M. A.; Hammond, P. T.; Grodzinsky, A. J. Charge Based Intra-Cartilage Delivery of Single Dose Dexamethasone Using Avidin Nano-Carriers Suppresses Cytokine-Induced Catabolism Long Term. *Osteoarthritis Cartilage* **2016**, *24* (1), 71–81. https://doi.org/10.1016/j.joca.2015.07.010.

(73) Mouw, J. K.; Ou, G.; Weaver, V. M. Extracellular Matrix Assembly: A Multiscale Deconstruction. *Nat Rev Mol Cell Biol* **2014**, *15* (12), 771–785. https://doi.org/10.1038/nrm3902.

(74) Rauti, R.; Renous, N.; Maoz, B. M. Mimicking the Brain Extracellular Matrix in Vitro: A Review of Current Methodologies and Challenges. *Israel Journal of Chemistry* **2020**, *60* (12), 1141–1151. https://doi.org/10.1002/ijch.201900052.

(75) Nicholson, C.; Kamali-Zare, P.; Tao, L. Brain Extracellular Space as a Diffusion Barrier. *Comput. Visual Sci.* **2011**, *14* (7), 309–325. https://doi.org/10.1007/s00791-012-0185-9.

(76) Sophia Fox, A. J.; Bedi, A.; Rodeo, S. A. The Basic Science of Articular Cartilage: Structure, Composition, and Function. *Sports Health* **2009**, *1* (6), 461–468. https://doi.org/10.1177/1941738109350438.

(77) Pfisterer, K.; Shaw, L. E.; Symmank, D.; Weninger, W. The Extracellular Matrix in Skin Inflammation and Infection. *Frontiers in Cell and Developmental Biology* **2021**, *9*.

(78) Hay, E. D. *Cell Biology of Extracellular Matrix: Second Edition*; Springer Science & Business Media, 1991.

(79) Travascio, F.; Arends, F.; Lieleg, O. *Composition and Function of the Extracellular Matrix in the Human Body*; IntechOpen, 2016. https://doi.org/10.5772/61601.

(80) Whatcott, C. J.; Posner, R. G.; Von Hoff, D. D.; Han, H. Desmoplasia and Chemoresistance in Pancreatic Cancer. In *Pancreatic Cancer and Tumor Microenvironment*; Grippo, P. J., Munshi, H. G., Eds.; Transworld Research Network: Trivandrum (India), 2012.

(81) Schwertfeger, K. L.; Cowman, M. K.; Telmer, P. G.; Turley, E. A.; McCarthy, J. B. Hyaluronan, Inflammation, and Breast Cancer Progression. *Front. Immunol.* **2015**, *6*. https://doi.org/10.3389/fimmu.2015.00236.

(82) Liu, M.; Tolg, C.; Turley, E. Dissecting the Dual Nature of Hyaluronan in the Tumor Microenvironment. *Front Immunol* **2019**, *10*. https://doi.org/10.3389/fimmu.2019.00947.

(83) Koyilot, M. C.; Natarajan, P.; Hunt, C. R.; Sivarajkumar, S.; Roy, R.; Joglekar, S.; Pandita, S.; Tong, C. W.; Marakkar, S.; Subramanian, L.; Yadav, S. S.; Cherian, A. V.; Pandita, T. K.; Shameer, K.; Yadav, K. K. Breakthroughs and Applications of Organ-on-a-Chip Technology. *Cells* **2022**, *11* (11), 1828. https://doi.org/10.3390/cells11111828.

(84) Ingber, D. E. Human Organs-on-Chips for Disease Modelling, Drug Development and Personalized Medicine. *Nat Rev Genet* **2022**, 1–25. https://doi.org/10.1038/s41576-022-00466-9.

(85) Danku, A. E.; Dulf, E.-H.; Braicu, C.; Jurj, A.; Berindan-Neagoe, I. Organ-On-A-Chip: A Survey of Technical Results and Problems. *Frontiers in Bioengineering and Biotechnology* **2022**, *10*.

(86) Osório, L. A.; Silva, E.; Mackay, R. E. A Review of Biomaterials and Scaffold Fabrication for Organ-on-a-Chip (OOAC) Systems. *Bioengineering* **2021**, *8* (8), 113. https://doi.org/10.3390/bioengineering8080113.

(87) Kleinman, H. K.; McGarvey, M. L.; Hassell, J. R.; Star, V. L.; Cannon, F. B.; Laurie, G. W.; Martin, G. R. Basement Membrane Complexes with Biological Activity. *Biochemistry* **1986**, *25* (2), 312–318. https://doi.org/10.1021/bi00350a005.

(88) Kleinman, H. K.; Martin, G. R. Matrigel: Basement Membrane Matrix with Biological Activity. *Seminars in Cancer Biology* **2005**, *15* (5), 378–386. https://doi.org/10.1016/j.semcancer.2005.05.004.

(89) Arends, F.; Nowald, C.; Pflieger, K.; Boettcher, K.; Zahler, S.; Lieleg, O. The Biophysical Properties of Basal Lamina Gels Depend on the Biochemical Composition of the Gel. *PLoS One* **2015**, *10* (2). https://doi.org/10.1371/journal.pone.0118090.

(90) Brown, R. A. In the Beginning There Were Soft Collagen-Cell Gels: Towards Better 3D Connective Tissue Models? *Experimental Cell Research* **2013**, *319* (16), 2460–2469. https://doi.org/10.1016/j.yexcr.2013.07.001.

(91) D. Castiaux, A.; M. Spence, D.; Scott Martin, R. Review of 3D Cell Culture with Analysis in Microfluidic Systems. *Analytical Methods* **2019**, *11* (33), 4220–4232. https://doi.org/10.1039/C9AY01328H.

(92) Axelrod, D.; Koppel, D. E.; Schlessinger, J.; Elson, E.; Webb, W. W. Mobility Measurement by Analysis of Fluorescence Photobleaching Recovery Kinetics. *Biophys J* **1976**, *16* (9), 1055–1069. https://doi.org/10.1016/S0006-3495(76)85755-4.

(93) Deschout, H.; Raemdonck, K.; Demeester, J.; De Smedt, S. C.; Braeckmans, K. FRAP in Pharmaceutical Research: Practical Guidelines and Applications in Drug Delivery. *Pharm Res* **2014**, *31* (2), 255–270. https://doi.org/10.1007/s11095-013-1146-9.

(94) Hess, S. T.; Huang, S.; Heikal, A. A.; Webb, W. W. Biological and Chemical Applications of Fluorescence Correlation Spectroscopy: A Review. *Biochemistry* **2002**, *41* (3), 697–705. https://doi.org/10.1021/bi0118512.

(95) Magde, D.; Elson, E.; Webb, W. W. Thermodynamic Fluctuations in a Reacting System---Measurement by Fluorescence Correlation Spectroscopy. *Phys. Rev. Lett.* **1972**, *29* (11), 705–708. https://doi.org/10.1103/PhysRevLett.29.705.

(96) Suh, J.; Dawson, M.; Hanes, J. Real-Time Multiple-Particle Tracking: Applications to Drug and Gene Delivery. *Advanced Drug Delivery Reviews* **2005**, *57* (1), 63–78. https://doi.org/10.1016/j.addr.2004.06.001.

(97) Schmidt, R.; Weihs, T.; Wurm, C. A.; Jansen, I.; Rehman, J.; Sahl, S. J.; Hell, S. W. MINFLUX Nanometer-Scale 3D Imaging and Microsecond-Range Tracking on a Common Fluorescence Microscope. *Nat Commun* **2021**, *12* (1), 1478. https://doi.org/10.1038/s41467-021-21652-z.

(98) Valentine, M. T.; Perlman, Z. E.; Gardel, M. L.; Shin, J. H.; Matsudaira, P.; Mitchison, T. J.; Weitz, D. A. Colloid Surface Chemistry Critically Affects Multiple Particle Tracking Measurements of Biomaterials. *Biophysical Journal* **2004**, *86* (6), 4004–4014. https://doi.org/10.1529/biophysj.103.037812.

(99) Reitan, N. K.; Juthajan, A.; Lindmo, T.; Davies, C. de L. Macromolecular Diffusion in the Extracellular Matrix Measured by Fluorescence Correlation Spectroscopy. *JBO* **2008**, *13* (5), 054040. https://doi.org/10.1117/1.2982530.

(100) Kihara, T.; Ito, J.; Miyake, J. Measurement of Biomolecular Diffusion in Extracellular Matrix Condensed by Fibroblasts Using Fluorescence Correlation Spectroscopy. *PLoS One* **2013**, *8* (11). https://doi.org/10.1371/journal.pone.0082382.

(101) Stylianopoulos, T.; Poh, M.-Z.; Insin, N.; Bawendi, M. G.; Fukumura, D.; Munn, L. L.; Jain, R. K. Diffusion of Particles in the Extracellular Matrix: The Effect of Repulsive Electrostatic Interactions. *Biophysical Journal* **2010**, *99* (5), 1342–1349. https://doi.org/10.1016/j.bpj.2010.06.016.

(102) Zhang, X.; Hansing, J.; Netz, R. R.; DeRouchey, J. E. Particle Transport through Hydrogels Is Charge Asymmetric. *Biophys. J.* **2015**, *108* (3), 530–539. https://doi.org/10.1016/j.bpj.2014.12.009.

(103) Hansing, J.; Ciemer, C.; Kim, W. K.; Zhang, X.; DeRouchey, J. E.; Netz, R. R. Nanoparticle Filtering in Charged Hydrogels: Effects of Particle Size, Charge Asymmetry and Salt Concentration. *Eur. Phys. J. E* **2016**, *39* (5), 53. https://doi.org/10.1140/epje/i2016-16053-2.

(104) Leddy, H. A.; Guilak, F. Site-Specific Molecular Diffusion in Articular Cartilage Measured Using Fluorescence Recovery after Photobleaching. *Annals of Biomedical Engineering* **2003**, *31* (7), 753–760. https://doi.org/10.1114/1.1581879.

(105) Pluen, A.; Boucher, Y.; Ramanujan, S.; McKee, T. D.; Gohongi, T.; di Tomaso, E.; Brown, E. B.; Izumi, Y.; Campbell, R. B.; Berk, D. A.; Jain, R. K. Role of Tumor–Host Interactions in Interstitial Diffusion of Macromolecules: Cranial vs.

Subcutaneous Tumors. *Proceedings of the National Academy of Sciences* **2001**, *98* (8), 4628–4633. https://doi.org/10.1073/pnas.081626898.

(106) Magzoub, M.; Jin, S.; Verkman, A. S. Enhanced Macromolecule Diffusion Deep in Tumors after Enzymatic Digestion of Extracellular Matrix Collagen and Its Associated Proteoglycan Decorin. *FASEB J.* **2008**, *22* (1), 276–284. https://doi.org/10.1096/fj.07-9150com.

(107) Netti, P. A.; Berk, D. A.; Swartz, M. A.; Grodzinsky, A. J.; Jain, R. K. Role of Extracellular Matrix Assembly in Interstitial Transport in Solid Tumors. *Cancer Res* **2000**, *60* (9), 2497–2503.

(108) Tomasetti, L.; Liebl, R.; Wastl, D. S.; Breunig, M. Influence of PEGylation on Nanoparticle Mobility in Different Models of the Extracellular Matrix. *European Journal of Pharmaceutics and Biopharmaceutics* **2016**, *108*, 145–155. https://doi.org/10.1016/j.ejpb.2016.08.007.

(109) Godin, A. G.; Varela, J. A.; Gao, Z.; Danné, N.; Dupuis, J. P.; Lounis, B.; Groc, L.; Cognet, L. Single-Nanotube Tracking Reveals the Nanoscale Organization of the Extracellular Space in the Live Brain. *Nature Nanotechnology* **2017**, *12* (3), 238–243. https://doi.org/10.1038/nnano.2016.248.

(110) Tada, H.; Higuchi, H.; Wanatabe, T. M.; Ohuchi, N. In Vivo Real-Time Tracking of Single Quantum Dots Conjugated with Monoclonal Anti-HER2 Antibody in Tumors of Mice. *Cancer Res* **2007**, *67* (3), 1138–1144. https://doi.org/10.1158/0008-5472.CAN-06-1185.

(111) Mair, L. O.; Superfine, R. Single Particle Tracking Reveals Biphasic Transport during Nanorod Magnetophoresis through Extracellular Matrix. *Soft Matter* **2014**, *10* (23), 4118–4125. https://doi.org/10.1039/C4SM00611A.

(112) Li, Y.; Shang, L.; Nienhaus, G. U. Super-Resolution Imaging-Based Single Particle Tracking Reveals Dynamics of Nanoparticle Internalization by Live Cells. *Nanoscale* **2016**, *8* (14), 7423–7429. https://doi.org/10.1039/C6NR01495J.

(113) Tchoryk, A.; Taresco, V.; Argent, R. H.; Ashford, M.; Gellert, P. R.; Stolnik, S.; Grabowska, A.; Garnett, M. C. Penetration and Uptake of Nanoparticles in 3D Tumor Spheroids. *Bioconjugate Chem.* **2019**, *30* (5), 1371–1384. https://doi.org/10.1021/acs.bioconjchem.9b00136.

Objectives and Thesis Content

Chapter 1 described the current challenges in nanoparticle development as drug carriers for cancer therapy. A key aspect in the process of designing nanocarriers is to be able to quickly assess their ability to cross the different barriers faced on their way through the body. In this sense, there is a growing need for *in vitro* platforms that can mimic different parts of the nanocarriers' journey in order to provide timely feedback for the rational design of nanocarriers.

The main aim of the thesis is to test nanocarriers' ability to overcome several barriers, with a particular focus on the crossing of tumor tissue, for which to provide a 3D testing platform simple enough for repetitive use as a tool in testing different types of nanocarriers, for observing their interactions and mobility inside ECM as well as cellular uptake into matrix-embedded spheroids.

In order to provide valuable insights onto different parts of the nanocarriers' journey for our specific NPs, we started with the characterization of the behavior in biological media and 2D cell cultures for a small library of polymeric micelles, differing in hydrophilic shell and in the length of the hydrophobic end. **Chapter 2** describes the physicochemical characteristics of the micelle design, then focuses on micelle interaction with serum albumin as a main component of protein corona. Through a fluorescence reporter mechanism, the micelle assembly state is then correlated with imaging data, allowing an in-depth characterization of micelle internalization into HeLa cell cultures and of the drug release behavior, which showed how important is the choice of hydrophilic shell for the polymeric micelle properties.

After the thorough characterization of the micelles in 2D, we moved on to a 3D testing platform. **Chapter 3** presents a simple microfluidic chip that mimics the "tumor ECM" environment containing two types of extracellular matrix and MCF7 spheroids. Polymeric micelles were tested in this platform, bringing further insights into their mobility and interactions inside ECM as well as spheroid internalization. The micelle design is then taken further, with a tri-block copolymer bringing new insights into the ECM passage mechanism.

In **chapter 4**, another type of nanocarrier is tested in the dual-ECM microfluidic chip, namely single chain polymeric nanoparticles (SCPNs). The chapter shows the comparison of a small SCPNs library comprised of different hydrophobic, hydrophilic and charged groups, assessing their effect on SCPNs interactions with ECM and internalization into spheroids. A covalently attached spectral reporter allowed the localized monitoring of particle folding state, providing valuable clues on the interplay of SCPNs stability and cellular interactions.

Specific objectives can be listed as follows:

O1 – Test the behavior of polymeric micelles in biological media

O2 – Test the uptake of polymeric micelles in 2D cultures of HeLa cells

O3 – Test the disencapsulation of a fluorescent dye from polymeric micelles in biological media and in 2D HeLa cell culture

O4 – Develop a simple 3D model for testing nanocarriers' penetration through tumor tissue, including ECM

O5 – Validate the 3D model

O6 – Test the behavior of polymeric micelles inside the 3D model

O7 – Adjust the design of polymeric micelles according to the results in O6 and test the new formulations

O8 – Test Single Chain Polymeric Nanoparticles inside the 3D model

Chapter 2. Micelles interactions in biological environments

The content of this chapter reproduces almost identically parts of the article: *Judging Enzyme-Responsive Micelles by Their Covers: Direct Comparison of Dendritic Amphiphiles with Different Hydrophilic Blocks.* <u>Gadi Slor</u>, <u>Alis R. Olea</u>, Sílvia Pujals, Ali Tigrine, Victor R. De La Rosa, Richard Hoogenboom, Lorenzo Albertazzi, and Roey J. Amir. Biomacromolecules 2021 22 (3), 1197–1210. DOI: 10.1021/acs.biomac.0c01708

As a joint first author of the article, my contribution was the biological part, consisting of all cellular and BSA experiments, while G. Slor performed the micelle synthesis, physico-chemical characterization and drug encapsulation experiments. The article manuscript was revised by all authors.

INTRODUCTION

Polymeric nano-assemblies, amongst them polymeric micelles, have shown great potential as drug delivery systems (DDS) as well as in many other biomedical applications.[1–3] This is due to the ability to dramatically increase the very low water solubility of lipophilic drug molecules by encapsulating them inside the hydrophobic cavities of the assemblies, simultaneously shielding them from the hostile biological environment. In addition, in many cases these assemblies have sizes that allow passive accumulation in cancerous or inflamed tissues due to the enhanced permeability and retention (EPR) effect.[4,5]

Despite the substantial advantages proven in numerous scientific reports, there are still challenges to overcome in order to increase the clinical translation of polymeric DDS.[6] Hence it is essential to further conduct fundamental research in this important field in order to gain a deeper understanding of the parameters that govern the stability and functionality of such nanocarriers and open the way for their broader application in biomedicine.

On one hand, DDSs should be extremely stable to withstand the high dilution and interactions with blood components in order to allow their circulation in the body while maintaining their cargo of active drug molecules.[7] On the other hand, the nanocarriers should be able to release the drugs when the DDS has reached the target site.[8–11] To address this need, over the last three decades there has been a great interest in utilizing stimuli-responsive polymeric micelles as DDS to allow selective release of their therapeutic cargo.[12,13] There are many reported examples of polymeric micelles that disassemble due to changes in pH,[14–17] temperature[18–21] or redox potential,[22–25] while there are significantly fewer examples of polymeric nanocarriers that can disassemble due to the presence of a designated enzyme.[26–29] Enzymes are very appealing for triggering the disassembly of drug containing micelles since they are already present in the body, known for their high substrate specificity and in many cases specific enzymes are overexpressed in diseased tissues.[30–32]

Polymeric micelles are typically formed by the self-assembly of amphiphilic di-block copolymers so that the hydrophobic block forms the micellar core and the hydrophilic block forms the micellar corona. It is clear that in biological environment most of the interactions between the micelle and its surroundings occur through the micelle's corona.[33,34] It is interesting to note that although most reported DDS are based on PEG,[35,36] the usage of additional types of promising hydrophilic polymers such as

polyoxazoline[37–39] and polyacrylates[40] have also been reported. To allow the rational design of DDS it is critical to compare and study the behavior of different corona forming polymers in order to rationally select the most suited hydrophilic block.

For a direct comparison between different hydrophilic polymers as micellar shells, it is essential that the hydrophobic core-forming block will be identical. Using dendrons as the core forming block provides many advantages due to their well-defined structure and monodispersity,[41–44] and hence can be ideal for the purpose of the above mentioned comparison.

In this chapter we report a direct comparison regarding the biological interactions of a customized library of fluorescently labeled polymeric micelles varying in hydrophilic shell and in the length of a dendritic hydrophobic core. We studied three types of commonly used hydrophilic polymers: poly(ethylene glycol) (PEG), poly(2-ethyl-2-oxazoline) (PEtOx) and poly(acrylic acid) (PAA). PEG and PEtOx, which are non-charged polymers, were selected as they are considered as "stealth" polymers that decrease interaction with native proteins and other biomolecules and hence elongate circulation time of their conjugates *in vivo*.[45–47] PAA is polyanionic at physiological pH and is much more hydrophilic than the other two polymers. Each type of polymer was combined with two types of dendrons that differ in their hydrophobicity: one had four hexyl and the other one four nonyl ester end-groups (Fig. 1). This allowed both a head-to-head comparison between the three hydrophilic polymers and also to understand how altering the hydrophilic/ hydrophobic ratio affects the micelles' properties and interactions in biological media and in the presence of cell cultures.

RESULTS & DISCUSSION

Part 1: Micelle design and physico–chemical characterization

Our collaborators Gadi Slor and Prof. Roey Amir kindly provided us with 6 polymeric micelles for characterizing their interactions in biological environment. The micelles were obtained using a highly modular and high yielding synthesis approach.

We chose 7-(diethylamino)coumarin-3-carboxylic acid (7-DEAC) as the fluorescent tag due to its excimer formation ability that allows to distinguish whether the amphiphiles disassembled into unimers or remained as micelles under various

conditions.[48,49] Once 7-DEAC dyes are forced to be in close proximity within the micelles, their emission maxima shifts from 480 to ∼540 nm, and once the micelles disassemble, the emission shifts back to 480 nm. The synthetic methodology allowed a simple preparation of libraries of amphiphilic diblock copolymers that can be examined and compared in many aspects ranging from micellar stability and enzymatic degradability to more complex biological studies that are enabled due to the dendron's unique fluorescent response.

Briefly, the micelles were obtained using a high yelding converging synthesis. A dendron containing degradable end-groups with four chains of either six carbons (hexyl) or nine carbons (nonyl) was obtained and labeled with 7-DEAC dye. The labeled dendron was then coupled to one of the hydrophilic polymers using a copper(I)-catalyzed azide−alkyne cycloaddition (CuAAC). Three types of hydrophilic polymers were used: poly(2-ethyl-2-oxazoline) (PEtOx), poly(ethylene glycol) (PEG) and poly(acrylic acid) (PAA). Because of the comparative nature of this work, the polymers had similar molecular weights of approximately 5 kDa. The structure of the final amphiphiles obtained after the click reaction is shown in Figure 2.1.
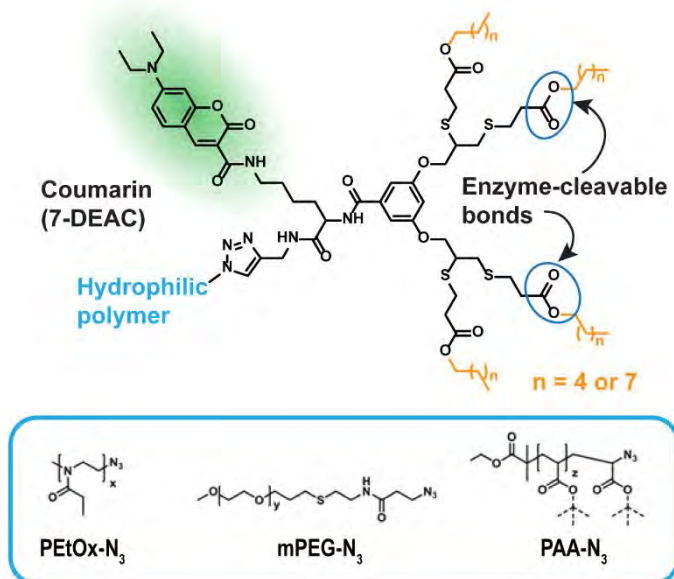
Figure 2.1: Chemical structure of dendritic amphiphiles. The hydrophobic block consists of an enzyme-cleavable dendron with four branches of either 6 or 9 carbons (hexyl or nonyl respectively). Each amphiphile is covalently labeled with a coumarin

fluorescent dye. Three types of hydrophilic polymers (shown in blue box) were added to the ampiphile structure through a CuAAC click reaction.

The synthetic methodology, as well as amphiphile purification and characterization are described in detail in the published article.

Micellization

The obtained amphiphiles are self-assembling in aqueous media (PB, pH 7.4, at 37 °C). To characterize the self-assembly, the critical molar concentration (CMC) of each polymer was determined using the Nile Red method.[50] The CMC values of the amphiphiles with hexyl end-groups were determined to be 5 ± 1, 6 ± 1, and 10 ± 2 µM for PEtOx-Hex, PEG-Hex, and PAA-Hex, respectively. This elucidates the tremendous effect of the hydrophobic block on the thermodynamic stability of polymeric micelles. The CMC values of the more hydrophobic nonyl amphiphiles were, as expected, slightly lower than those of the hexyl polymers and were determined to be 3 ± 1, 5 ± 1, and 9 ± 1 µM for PEtOxNon, PEG-Non, and PAA-Non, respectively. Even though there is a substantial difference in the chemical composition of the micelle coronas, the CMCs of the three amphiphiles in each series are very similar with slightly higher CMC value for the PAA-based amphiphiles, most likely due to the greater hydrophilicity and repulsion of the charged PAA chains.

Next, DLS was used to measure the diameters of the different micelles (Figure 2.2). The hexyl polymers self-assembled into micelles with diameters of 20 ± 2, 21 ± 2, and 20 ± 4 nm for PEtOxHex, PEG-Hex, and PAA-Hex, respectively, and the nonyl ones into 28 ± 5, 26 ± 5, and 32 ± 5 nm for PEtOx-Non, PEG-Non, and PAA-Non, respectively. It was fascinating to see the similar sizes of the micelles despite the different hydrophilic shells, demonstrating the key contribution of the hydrophobic block in directing the self-assembly of these polymeric amphiphiles into micelles.
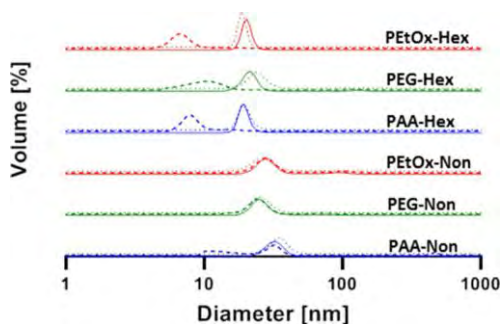
Figure 2.2. DLS measurements of the different micelles ([amphiphile] = 160 µM) before (solid lines) and after 24 h incubation in PB 7.4 with (dashed lines) and without (dotted lines) PLE (1.4 µM) at 37 °C.
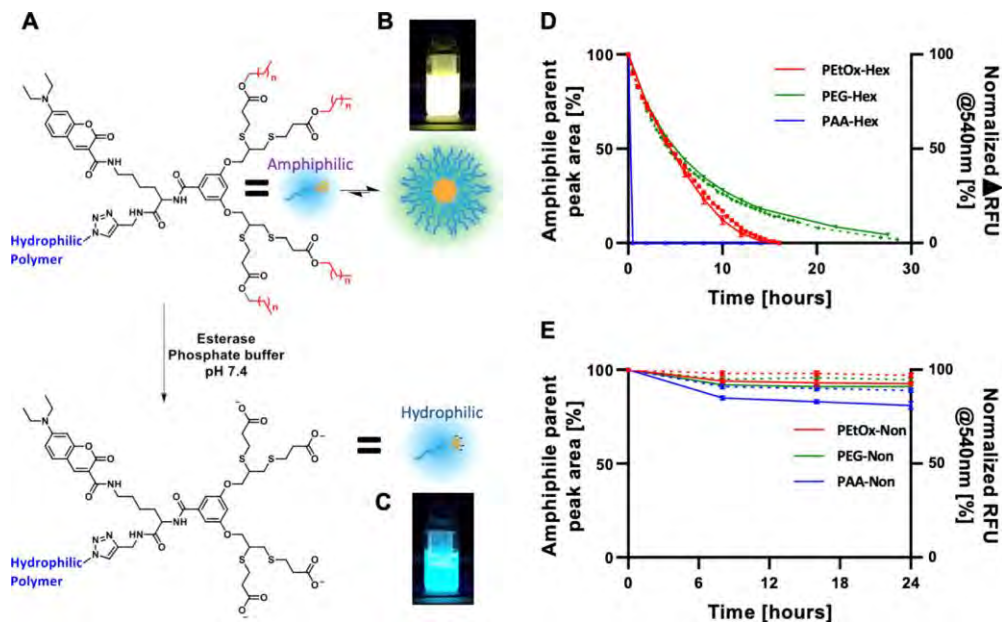
Enzymatic Degradation Rate

Furthermore, the enzymatic degradation rates of the six amphiphiles were studied in the presence of porcine liver esterase (PLE). PLE can selectively cleave the ester bonds between the dendron and the hydrophobic end-groups, exposing highly hydrophilic carboxylic acids on the dendron chain ends. This enzymatically induced modification will turn the polymer from amphiphilic into fully hydrophilic and therefore should cause the disassembly of the micelles (Figure 2.3A).

The enzymatic degradation was monitored by three independent methods: HPLC, fluorescence spectroscopy and DLS, showing high overlap of the measured degradation (by HPLC) and micelle disassembly rates (by fluorescence at 540 nm and DLS) (Figures 2.2 and 2.3).

Due to the high precision and purity of the polymers, we could directly monitor the degradation of the starting material and the appearance of the degraded polymer using HPLC (Figure 2.3D,E, solid lines). Simultaneously, we followed the enzymatically induced disassembly by monitoring 7-DEAC fluorescent response under the same conditions. Once an amphiphile's end-groups are cleaved, it becomes fully hydrophilic and diffuses away from the micelle. This leads to a decrease in 7-DEAC excimer formation, and this spectral response can be quantified by measuring the decrease in fluorescence emission at 540 nm and the increase at 480 nm (Figure 2.3B−E, dashed lines). Finally, DLS was used to determine whether micelles are present in solution before and after 24 h incubation at 37 °C with or without PLE (Figure 2.2, dashed lines). Notably, the nonyl amphiphiles showed high stability in the presence of PLE even at concentration as high as 1.4 µM. PEtOx-Non and PEG-Non showed approximately 10% degradation over 24 h, and around 20% degradation was observed for PAA-Non (Figure 2.3E).

Strikingly, although the change in the hydrophilic to hydrophobic ratio is relatively small for the nonyl and hexyl series as reflected by the small differences in CMC values, the hexyl-based amphiphiles were significantly more susceptible to enzymatic degradation. While full degradation of PEG-Hex required longer time than PEtOx-Hex, their t1/2 was almost identical. PAA-Hex, in contrast, showed ultrafast response

Figure 2.3. Enzymatic degradation. (A) Schematic representation of the enzymatic degradation of the hydrophobic end-groups turning the polymeric amphiphile into fully hydrophilic polymers leading to micelle disassembly. Pictures of the fluorescence of PEG-Hex after 30 h incubation without (B) and with (C) PLE demonstrating the system's spectral response. Enzymatic degradation profiles of hexyl- (D) and nonyl- (E) based micelles as monitored by HPLC (solid lines) and fluorescence spectroscopy (normalized decrease of emission intensity at 540 nm, dashed lines). [amphiphile] = 160 μM, [PLE] = 1.4 μM.

to PLE and was fully degraded after less than 30 min (Figure 2.3D, full lines). The faster degradation of the PAA amphiphile may be related to the higher hydrophilicity of the PAA compared to PEG and PEtOx, while the longer chain length of PEG-5k compared to PEtOx-5k and/or the slightly better anti-fouling behavior of PEG[51] may be responsible for the slower degradation of the PEG amphiphile. Fluorescence measurements showed a decrease in the longer wavelength emission of the micelle and increase in unimer emission, indicating that the enzyme led to disassembly of the micelles. Excellent correlations were observed between the degradation kinetics obtained by HPLC and the decrease in fluorescence intensity at 540 nm (Figure 2.3D,E, dashed lines), which is indicative of the disassembly of the cleaved polymers into unimers. This clearly demonstrates that, indeed, it is the cleavage of the hydrophobic end-groups by the enzyme that caused the micelles to disassemble. Last, DLS measurements after incubation with PLE confirmed the disassembly of the hexylbased micelles, while the nonyl-based series stayed intact (Figure 2.2, dashed

lines). In the control experiments conducted in the absence of PLE, all amphiphiles showed micelles with similar sizes to the ones measured at t0 after 24 h incubation (Figure 2.2, dotted lines). The similarities in CMCs and micelle sizes did not hint at the extreme difference in enzymatic degradation kinetics between the hexyl and nonyl polymers. The best example for this difference is seen for the two PAA-based amphiphiles, whereby PAA-Hex degraded in minutes while PAA-Non showed a very limited degree of degradation even after 24 h of incubation. This shows once more the tremendous effect of the hydrophobic block on the micellar dynamics and the importance of molecular precision when designing enzyme responsive polymeric amphiphiles.[52,53]

Part 2: Micelle interaction with biological media (BSA and cell culture experiments)

Interaction with Blood Proteins

After analyzing the *in vitro* properties of the six types of micelles, we moved on to study how these structural features influence their biological interactions. One of the first phenomena that occur upon introduction of nanoparticles into the bloodstream, in addition to significant dilution, is the interaction with proteins and their adsorption resulting in the formation of a protein corona,[61–64] which has been demonstrated to be key for shielding DDS from the immune system.[65] Therefore, we investigated the interactions between the different micelles and albumin, which is the most abundant serum protein,[66] as an initial evaluation of micelle–protein interactions.

In order to understand the differences in protein adsorption, we incubated the micelles with BSA labeled with Cy5, which serves as a FRET acceptor for the micelle fluorescence (and much less with the shorter wavelength unimer's fluorescence).[49] FRET is highly dependent on spatial proximity (1–10 nm)[67] and therefore the intensity of Cy5 emission qualitatively correlates with the interaction between the micelles and BSA. BSA is known to have hydrophobic regions that can interact with unimers and therefore significantly destabilize the micelles.[68–70] This type of interaction translates into an increase in the unimer emission (480 nm) and a decrease in micelle emission (540 nm), as illustrated in Figure 2.5A and B. The increase in the hydrophobicity of the dendron changes the unimer–micelle equilibrium and decreases the interactions between unimers and BSA, indicating an increase in micellar stability (Figure 2.5C). PEtOx and PEG micelles showed overall similar behavior with slightly
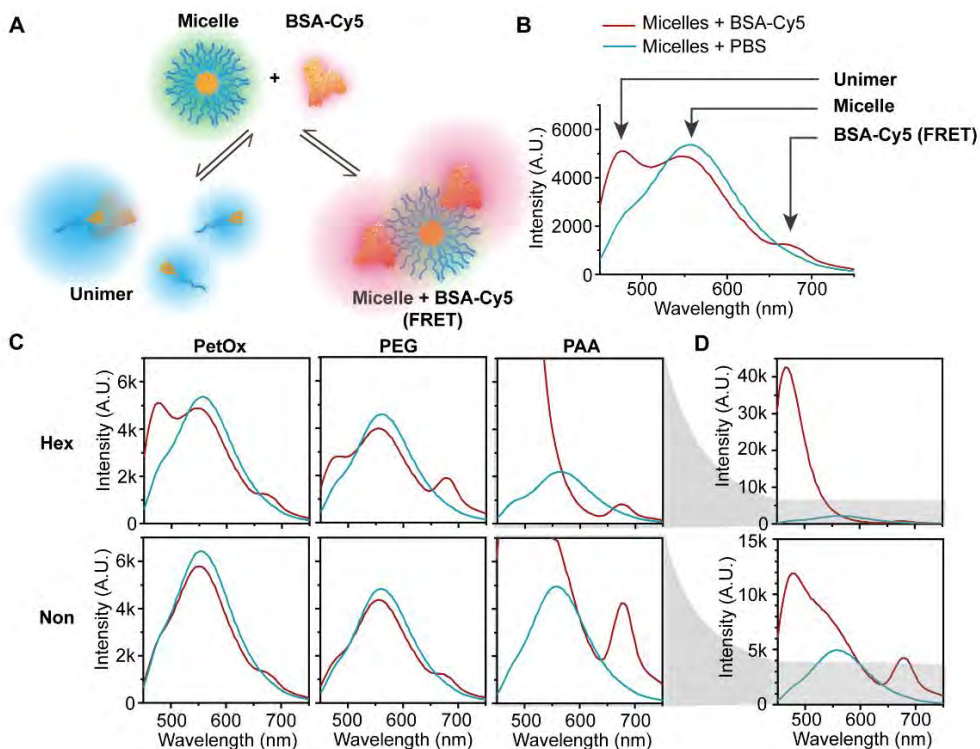
Figure 2.5. Micelle interaction with BSA-Cy5. (A) Illustration of the two main possible interaction pathways with Cy5 labeled BSA: interaction of BSA either with unimer (left) or micelle (right). (B) Selected fluorescence emission spectrum with arrows highlighting the contribution of the different species to the spectrum. (C) Fluorescence spectra of the micelles with (red lines) and without (blue lines) BSA-Cy5 and (D) Zoom out into PAA amphiphiles emission spectra. [amphiphile] = 160 μM, [BSA-Cy5] = 5.5 mg/ml, λ_{Ex} = 420 nm.

weaker interactions of PEtOx micelles with BSA indicated by a smaller peak of the FRET signal. For both PEtOx and PEG hexyl micelles, there was a moderate increase in the unimer emission, which is indicative of their interaction with BSA (Figure 2.5C). Almost no changes were observed for PEtOx and PEG nonyl micelles, which did not show an increase in the unimer peak upon incubation with BSA. On the other hand, PAA-Hex showed complete disassembly due to interactions with BSA as indicated by the total disappearance of the micelle fluorescence in addition to a significant increase in the unimer signal intensity (Figure 2.5C and D). The reason for this increase might be the change in the 7-DEAC microenvironment that can influence its quantum yield dramatically. PAA-Non also showed an increase in the unimer signal intensity, but the micelle signal still partially remains, and the Cy5 signal is the most intense amongst all micelles, suggesting the strongest micelle–BSA

interactions among the different amphiphiles. To monitor the destabilization of the micelles over time, we calculated the unimer to the micelle fluorescence ratio (Figure 2.6). All ratios were nearly constant during 5 h, except for PAA-Non, which showed an increase in the unimer/micelle ratio. Overall, this suggests that for all micelles, the interactions with BSA happen almost immediately after addition, leading to various types and degrees of interactions. While the more hydrophobic nonyl micelles generally interact less with BSA, the PAA-Non showed significantly stronger interaction of both micelles and unimers with BSA.
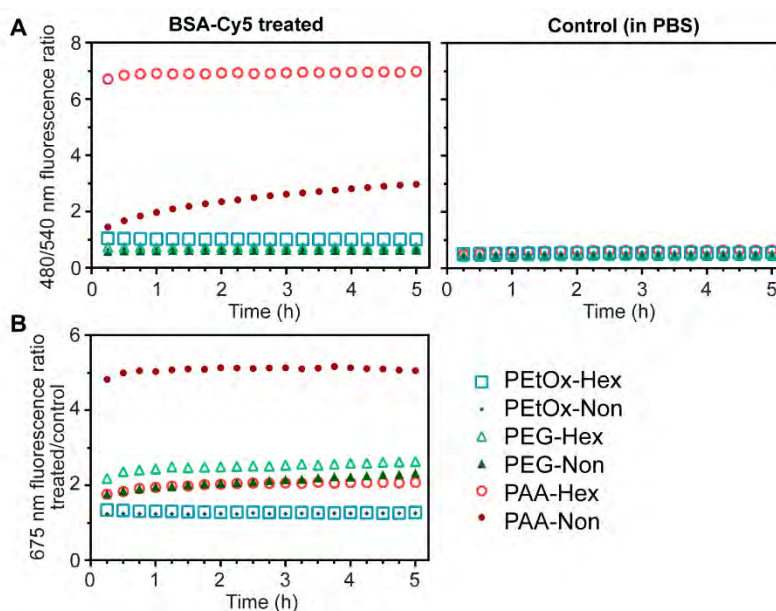
Figure 2.6. Time evolution of micelles incubation with BSA-Cy5. The evolution of fluorescent signal in time, excited with 420nm, is shown as ratio of unimer/micelle fluorescence (480nm/540nm) in BSA-Cy5 treated sample (A) or ratio of BSA-Cy5 FRET fluorescence (675 nm) in BSA-Cy5 treated sample over control sample in PBS (B). First measurement time-point is 15 minutes.

Cell Internalization

After assessing the micellar stability in the presence of BSA and confirming the lack of cytotoxicity of the different micelles (Figure 2.7), the next step was to investigate the internalization of micelles into HeLa cells. Therefore, the micelles were incubated with cells in full DMEM medium (with 10% fetal bovine serum) at a final micelle concentration of 160 μM and imaged with confocal microscopy.
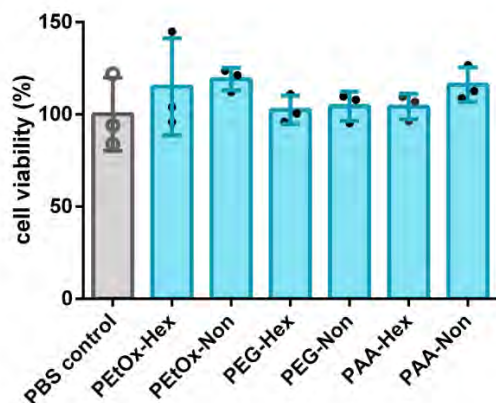
Figure 2.7. Cytotoxicity assay (PrestoBlue) on HeLa cells incubated with 160 µM micelles. The fluorescence signal was normalized with negative and positive controls.

Upon 405 nm excitation, we could differentiate the assembly states by separating the signal into two distinct channels: one for the unimer signal (400–500 nm) and one for the micelle signal (500–700 nm). Finally, we obtained total fluorescence and ratiometric images, by either combining the two channels or by dividing the unimer to micelle signal after background removal. Images with total fluorescence allowed a direct comparison of the internalization efficiency of the different amphiphiles as unimers and/or micelles, also showing the distribution inside different cellular compartments.

Ratiometric images allowed the visualization of the assembly state of the amphiphiles within any given pixel, enabling a deeper understanding of the behavior of the different micelles.

Looking at the total intensity inside cells, we could see a remarkable difference in the degree of internalization of the different micelles (Figure 2.8A top row and 5B). The micelles of PEtOx-Non and PEG-Non that were shown to be more stable showed a very weak signal within the cells. While PEtOx-Hex and PEG-Hex had similar distributions in intracellular vesicles, PAA-Hex and PAA-Non bound mostly to the cell membrane and had the most intense fluorescence emissions, similar to the trend observed for the incubation with BSA. Thus, we can assume that the hydrophilic block directs the cellular fate of the micelles toward the endo-lysosomal compartments for PEtOx and PEG and membrane-bound for PAA. Interestingly, the

relatively small change in hydrophobicity causes a notable decrease in internalization efficiency for the nonyl micelles.
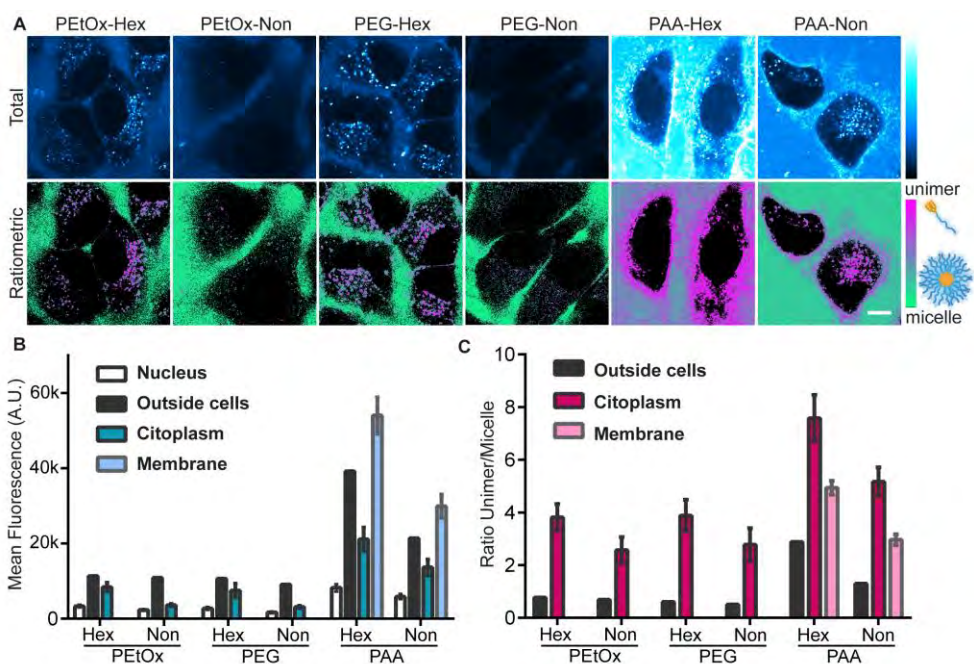

Figure 2.8. Internalization of micelles into HeLa cells, after 1 hour incubation in DMEM with 10% FBS. Images show total fluorescence signal with 405nm excitation (A, top row) or ratiometric images of unimer/ micelle pixel ratio after background removal (A, bottom row). Green color indicates micellar form and magenta the unimer form. Scale bar is 10 μm. The median fluorescence for control areas (inside nucleus as negative control and in solution outside cells as positive control) were plotted along with the mean fluorescence inside the cytoplasm or in the membrane area (n=8-10 cells) for either total fluorescence (B) or unimer/micelle ratio (C).

To assess whether this difference is due to disassembly of the micelles outside or inside the cells, we analyzed the ratiometric images (Figure 2.8A bottom row). For all amphiphiles except PAA-Hex, the ratiometric analysis indicated the presence of micelles outside the cells, while inside cells or on the cell membrane, all amphiphiles were mostly in their unimer form (Figure 2.8C). However, slightly more micelles were observed inside the cells for the more stable PEtOx-Non and PEG-Non (Figure 2.8B,C). We can assume that the less stable PAA micelles disassembled outside the cells more readily into unimers that could then intercalate into the plasma membrane. For the polymers that were localized in endosomal vesicles, it may be that they

internalized as micelles and very rapidly disassembled inside the endosomal vesicles into unimers.

To achieve higher degree of internalization and obtain more intense fluorescence signal inside the cells, the experiment was repeated with a longer incubation time of 6 h (Figure 2.9). The longer incubation time indeed led to a stronger signal within the cells, which was mostly observed in the unimer channel. Although the ratiometric images indicated the presence of unimers inside the cells, it is most likely that the increased internalization cannot be attributed to the disassembly of the micelles outside of the cells over time. This assumption is based on the high micellar stability for PEtOx-Non and PEG-Non, which remained highly stable when incubated with BSA, PLE, and outside of the cells.

The degree of internalization was further validated by spectral flow cytometry after incubation times of 1 h and 6 h using both unimer and micelle channels (Figure 2.10). In this case, the measured fluorescence spectra was analysed with two gates corresponding to unimer and micelle fluorescence. The resulting hystograms and mean fluorescence reflected the microscopy results.
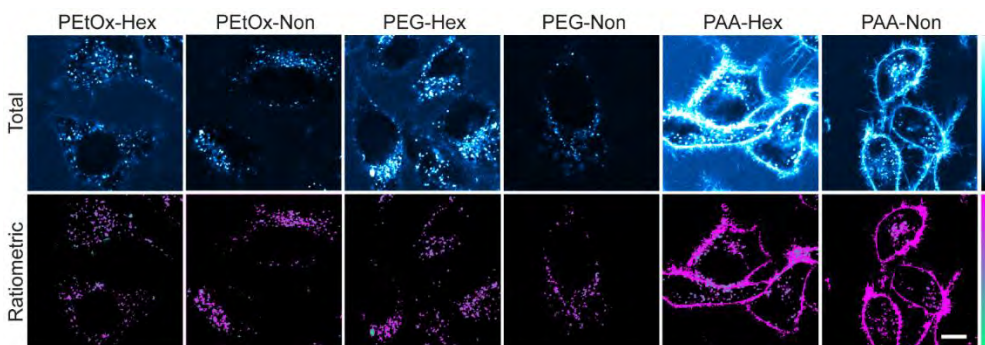
Figure 2.9. Micelles incubated with HeLa cells for 6 hours at 160 µM in full DMEM (10% FBS), then washed with PBS. Sum images of total fluorescence (first row) and ratiometric images (second row), where magenta represents unimer form and green represents micelle form. Scale bar is 20 µm.
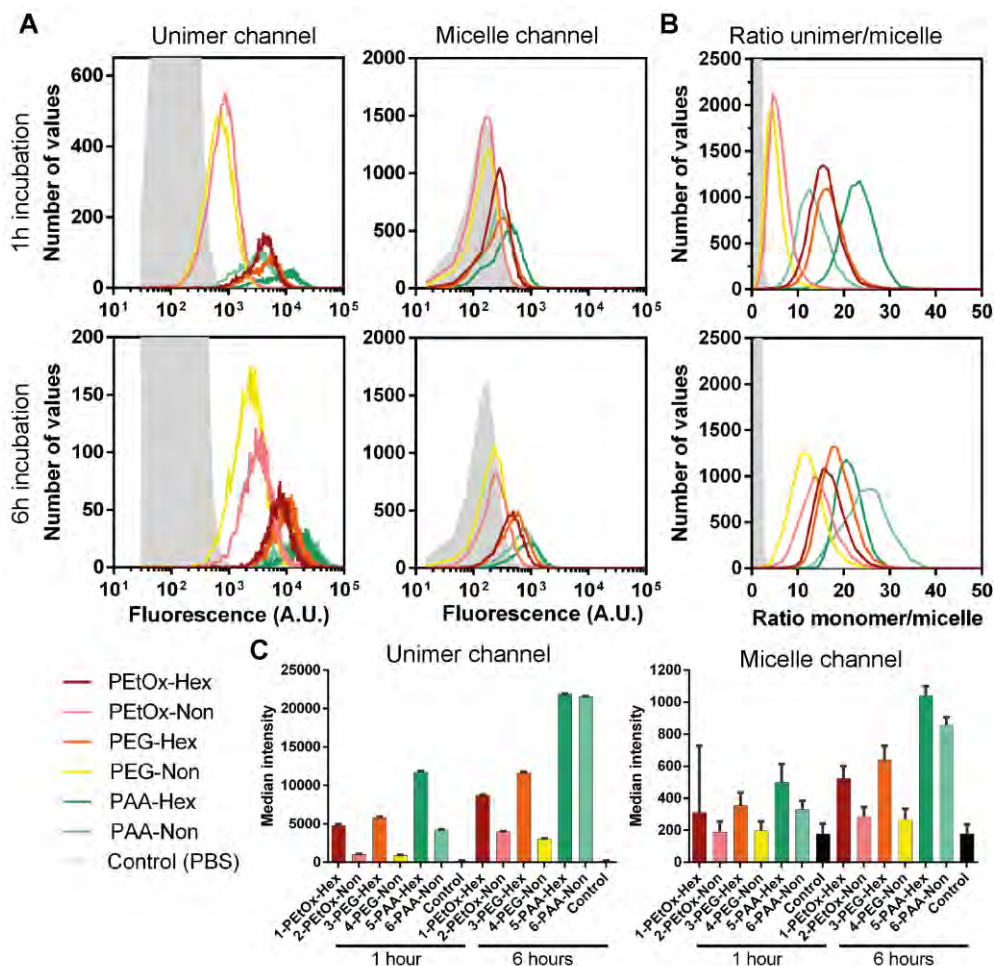
Figure 2.10. Flow cytometry analysis of micelle internalization in HeLa cells for 1h or 6h incubation at 160 μM. A spectral flow cytometer was set with two gates. Histograms of either unimer or micelle channels (A) and histograms of the unimer/monomer ratios in each cell (B) are shown, as well as median intensity (C) for either 1h or 6h incubation.

## Part 3: Encapsulation Stability and Cargo Release in the Presence of BSA and Cell Culture

In addition to the crucial effect of micellar stability on the ability of the micelles to retain their molecular cargo, one of the major drawbacks in physical encapsulation of hydrophobic compounds is the possibility of premature leakage, that is, before reaching the tumor through passive targeting via the EPR effect, due to migration of

the cargo into native hydrophobic regions in the surroundings of the carrier such as proteins or membranes.[71] Hence, after studying the stability of the micelles, we evaluated their ability to retain their cargo of hydrophobic molecules in a biological environment. Therefore, another FRET-based experimental setup was designed in order to study how encapsulated hydrophobic cargo behaves in the presence of BSA. A hydrophobic Cy5 derivative (Figure 2.11A), which served as a model for an encapsulated lipophilic drug, was physically encapsulated within the different micelles, and non-labeled BSA was added to the micellar solution. The encapsulated Cy5-derivative undergoes significant FRET with the fluorescence of the micelles while its migration from the micelles to BSA or its precipitation due to micelle disassembly into unimers should translate into a reduction in FRET efficiency (Figure 2.12A).

Prior to the fluorescence measurements, the absorbance spectra was measured for all tested solutions containing micelles with encapsulated Cy5, in the presence of cellular media (DMEM with 10% FBS) to verify that the concentrations of the polymers and Cy5 were similar for all solutions (Figure 2.11B).

Next, fluorescence spectra were measured every 30 min over 2 h. Upon addition of BSA, both PEtOx and PEG micelles showed a decrease of ~30% in FRET-related emission, while a slight increase in both the micelle and unimer emission was
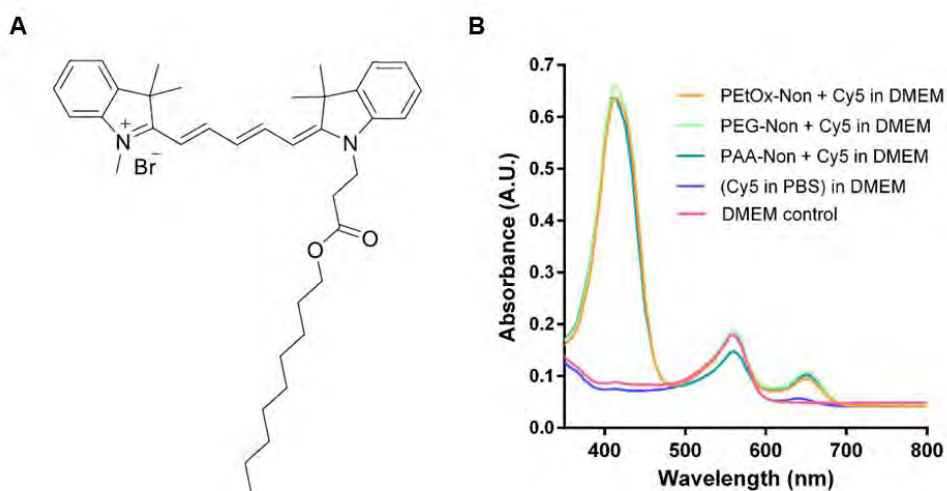

Figure 2.11. (A) A hydrophobic Cy5 derivative. (B) Absorbance of solutions with encapsulated Cy5 and control solution without micelles taken prior to imaging experiments.
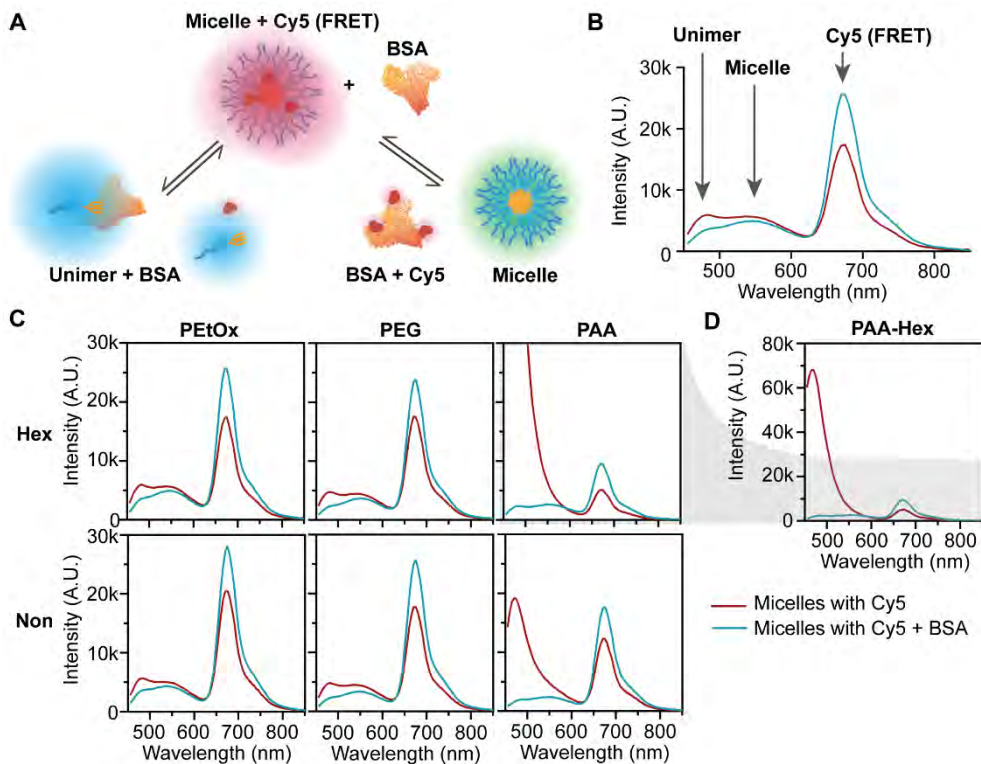
Figure 2.12. (A) Illustration of the two main possible interaction pathways between micelles with encapsulated Cy5 and BSA. (B) Selected fluorescence emission spectrum with arrows highlighting the contribution of the different species to the spectrum. (C) Fluorescence spectra of the micelles with encapsulated Cy5 with (red lines) and without (blue lines) BSA and (D) Zoom out into PAA-Hex emission spectra. [amphiphile] = 160 µM, [Cy5] = 4 µM, [BSA] = 5.5 mg/ml, λEx = 420 nm.

observed (Figure 2.12B,C). These results indicate that the majority of encapsulated Cy5 molecules remained entrapped inside the micelles as complete Cy5 release would lead to a complete disappearance of the FRET signal and a substantial increase in micelle fluorescence would be expected. A slight increase in unimer emission is attributed to the interaction of the micelles with the BSA, as described above (Figure 2.5). Interestingly, the least stable PAA-Hex micelles showed a significantly lower FRET signal in the absence of BSA, which was sustainably reduced by 50% upon the addition of BSA. In addition, a strong increase in the unimer emission was also observed, indicating the low stability of the PAA-Hex micelles and their tendency to disassemble due to interaction with BSA. Unlike the PAA-Hex, the PAA-Non-based micelles showed only a moderate decrease of ~30% of the FRET signal in the presence of BSA, similar to the PEG and PEtOx micelles. The notable increase in the

unimer emission of the PAA-Non can again be attributed to the stronger interaction with BSA (Figure 2.12A). The response to BSA was extremely fast in this experiment as noted before in the Cy5-labeled BSA assay, and no major changes were observed over time, which is indicative of the high encapsulation stability of the PEG, PEtOx, and PAA-Non micelles (Figure 2.13).
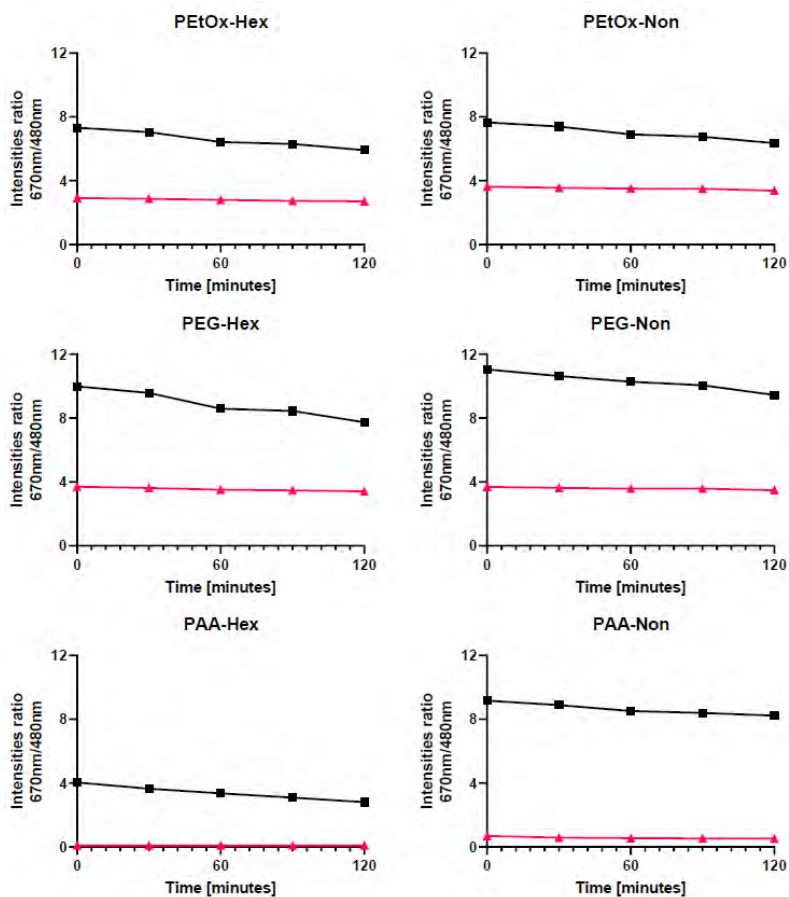
Figure 2.13. Fluorescence intensities ratio of Cy5 (670 nm) and unimer (480 nm) overtime at incubation with (pink lines) and in the absence (black lines) of BSA.

Intrigued by the encapsulation stability of the micelles in the presence of BSA, we decided to study the release of the Cy5 dyes in HeLa cell culture. Two possible mechanisms for the release of physically encapsulated cargo from polymeric micelles can be envisioned: (i) spontaneous leakage or (ii) disassembly and release. Spontaneous leakage would leave the micelles intact, while the Cy5 molecules would exit and accumulate inside cells. On the other hand, disassembly based release could

occur outside the cells followed by internalization of the unimers together with the released Cy5 dyes. Alternatively, the Cy5 containing micelles could be internalized followed by disassembly and cargo releasing in the endosomal vesicles. Based on the inferior stability noted in all previous experiments for the PAA micelles, we expected that the release of encapsulated cargo would be significantly faster in the presence of cells as a large fraction of PAA micelles disassembled in the presence of HeLa cell culture.

To study the effect of micellar corona composition on the release kinetics of hydrophobic cargo, we decided to prepare micelles only from the more stable nonyl amphiphiles. The three types of micelles were loaded with Cy5 and incubated with HeLa cells. The same cells were followed for 1 h, measuring the fluorescence of the unimer and micelle (excitation at 405 nm) as well as directly following the Cy5 (excited at 640 nm, Figure 2.14A). For every time point, the fluorescence was measured inside the cytoplasm of 10 cells and the mean values were compared to the signal outside the cells (Figure 2.14B). This unique setup provided important new insights regarding the behavior of the different micelles. By monitoring the ratio of unimer/micelle fluorescence, the assembly state of the amphiphiles in each pixel is revealed (Figure 2.14C). In addition, the Cy5 channel enabled direct monitoring of the cell internalization kinetics of the encapsulated cargo (Figure 2.14B). We hypothesized that the combination of the ratiometric data together with the direct tracking of Cy5 release would shed light on the release mechanism of the different micelles. First, we examined the assembly state of the micelles. As seen in the previous internalization experiments (Figure 2.8), PAA-Non micelles showed significant disassembly both outside and inside the cells, which increased over time (Figure 2.14C).

As expected, the PEtOx-Non and PEG-Non micelles were much more stable than the PAA-Non micelles and almost no disassembly was observed, as indicated by the nearly constant unimer/micelle fluorescence ratio (Figure 2.14C). Therefore, we were rather surprised to discover that the release and internalization of Cy5 was significantly slower from PAA-Non micelles compared with PEG-Non and PEtOx-Non. While both PEtOx-Non and PEG-Non samples showed dramatic increase in the Cy5 signal inside the cells, PAA-Non showed delayed and more gradual increase, even though its tendency to undergo micellar disassembly is much higher. The results of these experiments demonstrate that lower micellar stability does not always correlate with faster release kinetics, and that disassembly of the carrier is not essential for cargo release (Figure 2.15). Furthermore, these findings clearly

emphasize the importance of tracking both the carrier and the cargo when studying the internalization mechanism and kinetics of DDS.
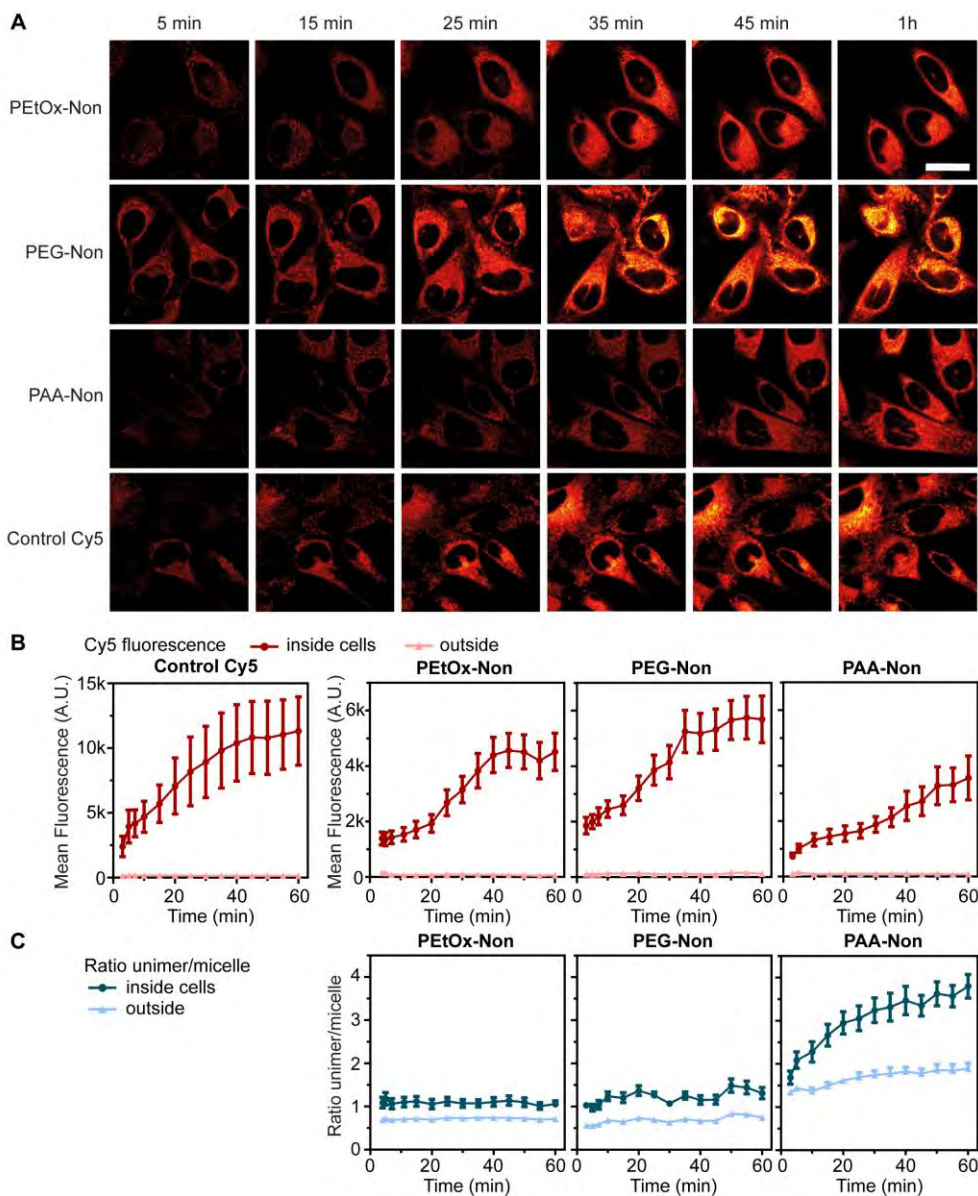
Figure 2.14. Release of encapsulated Cy5 onto HeLa cells over time. (A) Fluorescence with 640 nm excitation is shown inside HeLa cells at different time points for hydrophobic Cy5 encapsulated in micelles or free, in full DMEM (10% FBS), scale bar is 20 μm. The quantification of fluorescence from confocal images with (B) as mean fluorescence intensity in the Cy5 channel, with 640 nm excitation

or (C) 405 nm excitation is shown as ratio of unimer/micelle signal. Regions of interest were manually drawn around cell cytoplasm, including the cell membrane and excluding the nucleus; n = 10 cells. [amphiphile] = 160 µM, [Cy5] = 4 µM.
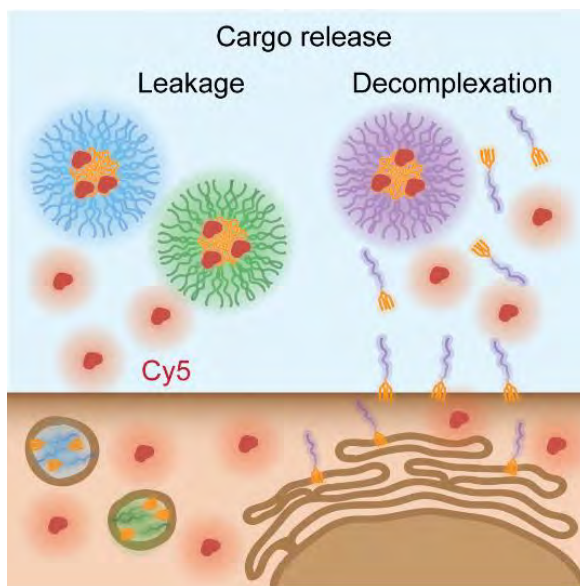
Figure 2.15. Schematic illustration of two types of cargo release by either leakage from stable micelles or disassembly of the polymeric carrier.

CONCLUSIONS

In summary, we compared a set of six polymeric micelles consisting of three widely-used hydrophilic polymers (PEtOx, PEG and PAA) and two types of enzymatically-degradable hydrophobic dendron (Hex or Non). The amphiphiles were obtained using a highly modular syntesis, allowing a direct one-to-ne comparison of the effect of different hydrophilic polymers onto micelle properties. Notably, the important stabilizing effect of the hydrophobic core was observable in the micelle's CMCs which were all below 10 µM, as well as in the enzymatic degradation which was very low for the more hydrophobic nonyl micells and was also greatly affected by the hydrophilic shell composition.

In addition, the composition of the hydrophilic block had a strong effect on the interactions of both unimers and micelles with BSA, which in the case of PAA-Hex led to the complete disassembly of the micelles (Figure 2.16). Cell internalization

experiments revealed a great difference in membrane binding and internalization rate between PAA amphiphiles and the PEtOx and PEG ones. PAA based amphiphiles localized more on the cell membrane and internalized to greater extent than the PEG and PEtOx based amphiphiles. In all cases, the more hydrophobic nonyl amphiphiles internalized significantly slower than the hexyl ones.

Using Cy5 dye as a model for encapsulated drug molecules, it was interesting to see its slower release and cell internalization in the case of the less stable PAA-Non based micelles, while much faster release was observed for the PEG-Non and PEtOx-Non, which seemed to have significantly more stable micelles. These encapsulation and release experiments in cell culture revealed the complexity of studying release mechanisms and the importance of directly tracking both the carrier and the cargo.

Overall, the ability to directly compare micelles with different shell and the resulting comparative results provide striking insight into how the composition of the shell and core of polymeric micelles can affect their properties and potential to serve as nanocarriers for DDS.
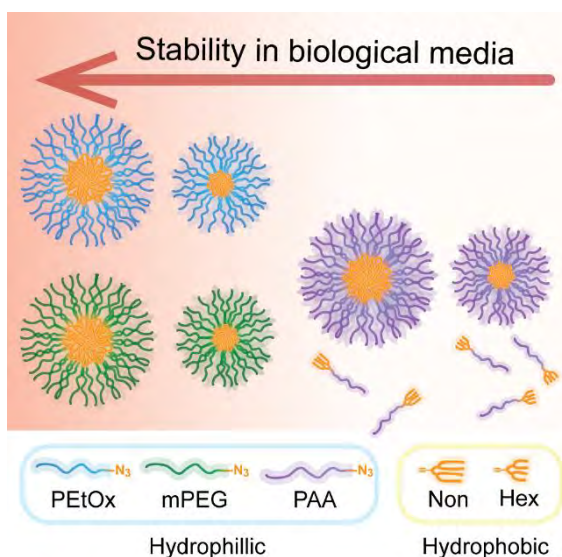
Figure 2.16. Schematic representation of the main conclusions of the interactions of micelles with biological media and cell cultures

MATERIALS AND METHODS

Instrumentation

HPLC: All measurements were recorded on a Waters Alliance e2695 separation module equipped with a Waters 2998 photodiode array detector. All solvents were purchased from Bio-Lab Chemicals and were used as received. All solvents are of highperformance liquid chromatography (HPLC) grade. 1H and 13C *Absorbance and fluorescence spectra*: measurements were recorded on a Tecan Infinite M200Pro device or Agilent Technologies Cary Eclipse Fluorescence Spectrometer. *Dynamic light scattering (DLS):* all measurements were recorded on a Corduran technology VASCOγ – particle size analyzer. *Confocal microscopy*: imaging was performed on a Zeiss LSM 800 confocal microscope, using $63\times$ plan-apochromat oil immersion objective. *Flow cytometry*: analysis was performed using a spectral analyzer (Sony SA3800) flow cytometer, 96/384w.

CMC (experiment performed by Gadi Slor in Tel Aviv University)

Preparation of Diluent. Nile Red stock solution (0.88 mg/ mL in ethanol) was diluted into a phosphate buffer (PB) (100 mM, pH 7.4) to afford a final concentration of 1.25 µM. *Preparation and Measurement of Samples*. The polymer-dendron amphiphile was directly dissolved in the diluent to give a final concentration of 250 µM. Solution was vortexed vigorously until the amphiphile completely dissolved and further sonicated for 15 min in an ultrasonic bath. This solution was consecutively diluted by a factor of 1.5 with the diluent to afford a series of 24 samples. 150 µL of each sample were loaded onto a 96 well plate, and a fluorescence emission scan was performed for each well. In order to determine the amphiphile's critical micelles' concentration (CMC) – the maximum emission of Nile Red (at about 630 nm) was plotted versus the amphiphile's concentration. This procedure was repeated three times for each amphiphile, and mean value is reported as the CMC and the standard deviation as the measurement error.

Enzymatic Degradation (experiment performed by Gadi Slor in Tel Aviv University)

A micellar solution of the tested amphiphile was prepared by directly adding PB (pH 7.4) to solid polymer to a final concentration of 160 µM. The vial was vortexed until full solubility was obtained and then placed in an ultrasonic bath for 15 min. PLE stock solution or PB was added (30 µL into 1470 µLor14µL into 686 µL for HPLC

or fluorescence experiments, respectively, to yield the final PLE concentration of 1.4 µM), and degradation was followed at 37 °C either by monitoring the area under the peak of the parent amphiphile by HPLC or the fluorescence emission at 540 nm. Each experiment was conducted thrice, and the reported values in each time point are the mean and the standard deviation is the error.

Blood Protein Interaction: Micelle Incubation with BSA-Cy5

The interaction between micelles and Cy5-labeled BSA was measured using Förster resonance energy transfer (FRET). Micelles solution in PBS (pH 7.4) at 145.5 µM was mixed with BSA (10% v/v labeled with cyanine 5) at the 5.5 µM final concentration or with the same volume of PBS. Each sample was 60 µL in final volume inside a 96 well plate (flat-bottom, transparent, NUNC). The samples were excited at the 420 nm wavelength, and a fluorescence spectra was collected between 450 and 750 nm, with a 5 nm step. A reading was performed for each well every 15 min for 5 h, with the initial time point being approximately 15 min after BSA addition (or PBS, respectively).

Cytotoxicity with PrestoBlue

The cellular toxicity was assessed using the PrestoBlue assay (ThermoFisher). HeLa cells were seeded at a density of 5000 cells/well in a 96-well plate (Nunc, transparent, flat-bottom plate). After 24 h, micelles were added to the final concentration of 160 µM in full DMEM. The same volume of PBS was added in the negative control, while Triton X-100 0.01% v/v was used as the positive control. The cells were incubated for 24 h at 37 °C 5% CO_2, then PrestoBlue was added 10% v/v and incubated for 1h at 37°C 5% CO_2. Fluorescence was measured in a multimode microplate reader (Infinite M200 Pro from Tecan) by sampling the emission from the bottom well at 600 nm, while exciting at 550 nm. Each sample was taken in three replicates, distributed randomly on each row (using randomizer.org). The signal was normalized using the negative and positive controls between 0 and 100%, respectively.

Micelle Incubation with HeLa Cells (Microscopy)

HeLa cells were seeded at 30000 cells/well density in 8-well LabTek, 200 µL/well, 24 h prior to the experiment. Medium was changed with fresh DMEM (10% FBS), and micelles were diluted 3× to the final concentration of 160 µM on the cells. Samples were imaged in a confocal microscope at 37 °C, 5% CO2. The fluorescence signal with 405 nm excitation 1% (diode laser, 5 mW) was acquired in two channels

representing unimers (446−500 nm) and micelles (526−589 nm), with equal gain. Data analysis was carried out on Fiji ImageJ. Total fluorescence images were obtained by summing unimer and micelle channels, then applying "Cyan hot" lookup table. For ratiometric images, background was removed using a mask obtained from the sum image that was multiplied with unimer and micelle images. Ratiometric images were obtained by dividing the background-removed unimer to micelle images.

Flow Cytometry on HeLa Cells Incubated with Micelles

HeLa cells were seeded in a 24-well plate at 120000 cells/well in 1 mL/well 24 h before the experiment. Micelles were added by diluting 3× to the 160 μM final concentration, for either 1 or 6 h of incubation. Cells were washed 2× with warm PBS, then trypsinized with 250 μL/well for 3−4 min at 37 °C, mixed with 750 μL/well full DMEM, centrifuged 3 min at 180 g, and then resuspended in 1 mL/well warm PBS. The fluorescence spectra with 405 nm excitation was recorded for 8000−10000 cells per sample using a spectral analyzer (Sony SA3800) flow cytometer. For data analysis, the spectral signal was gated in two "channels" representing unimers (420−500 nm) and micelles (550−700 nm).

Encapsulation Stability in the Presence of BSA

Micellar solution of the tested amphiphile was prepared in PBS (176μM). Hydrophobic Cy5 derivative was added directly (2 μL/mL from 2 mM Cy5 solution in EtOH), and solution was thoroughly vortexed. Then, 50 μL of either BSA solution (55 mg/mL in PBS) or PBS were added into 450 μL of the above solution, and solution was vortexed to obtain final concentrations of 160 and 4 μM for amphiphile and Cy5, respectively, and 5.5 mg/mL for BSA. Absorbance of all final solutions was measured at T0, and the emission spectra was recorded every 30 min for 2 h (λEx = 420 nm).

The experiment was performed both by me in Barcelona (Fig. 2.12) and by Gadi Slor in Tel Aviv (including the absorbance measurement before following the stability over a longer time – Fig. 2.13).

Imaging of Cy5 Release Experiments on HeLa Cells

Micelle solution in PBS (480 μM) was mixed with Cy5 solution in ethanol (2 mM) to the final Cy5 concentration 12 μM. Mixture was vortexed and filtered through

nylon 0.45 μm syringe filters (PureTech). Then, each solution was diluted with fresh DMEM (10% FBS) by three fold to final micelle and Cy5 concentration of 160 and 4 μM, respectively. Absorbance of each solution was measured in order to verify similarity in concentrations. Imaging was performed similarly to the cell internalization experiment. One field of view was followed for 1 h for each sample. For 405 nm excitation (5 mW diode laser, 1%), the acquisition was split in three channels representing unimer (400−500 nm), micelle (500−617 nm), and possible FRET fluorescence (656− 700 nm). For total Cy5 fluorescence, 640 nm excitation (5 mW diode laser, 0.2%) was used, with 656−700 nm acquisition. Also, an electronically switchable illumination and detection module (ESID,bright field-like) signal was acquired using a 488 nm (10 mW) diode laser. For image analysis (on Fiji ImageJ), regions of interest were drawn manually either outside the cells or containing cell cytoplasm and membrane, without the nucleus. Mean fluorescence inside cells and median outside cells were plotted using GraphPad Prism.

REFERENCES

(1) Langer, R.; Tirrell, D. A. Designing Materials for Biology and Medicine. *Nature* **2004**, *428* (6982), 487–492. https://doi.org/10.1038/nature02388.

(2) Cabral, H.; Kataoka, K. Progress of Drug-Loaded Polymeric Micelles into Clinical Studies. *Journal of Controlled Release* **2014**, *190*, 465–476. https://doi.org/10.1016/J.JCONREL.2014.06.042.

(3) Torchilin, V. P. Micellar Nanocarriers: Pharmaceutical Perspectives. *Pharmaceutical Research*. January 2007, pp 1–16. https://doi.org/10.1007/s11095-006-9132-0.

(4) Maeda, H.; Wu, J.; Sawa, T.; Matsumura, Y.; Hori, K. Tumor Vascular Permeability and the EPR Effect in Macromolecular Therapeutics: A Review. *Journal of Controlled Release* **2000**, *65* (1–2), 271–284. https://doi.org/10.1016/S0168-3659(99)00248-5.

(5) Satchi-Fainaro, R.; Puder, M.; Davies, J. W.; Tran, H. T.; Sampson, D. A.; Greene, A. K.; Corfas, G.; Folkman, J. Targeting Angiogenesis with a Conjugate of HPMA Copolymer and TNP-470. *Nature medicine* **2004**, *10* (3), 255–261. https://doi.org/10.1038/nm1002.

(6) van der Meel, R.; Lammers, T.; Hennink, W. E. Cancer Nanomedicines: Oversold or Underappreciated? *Expert Opinion on Drug Delivery* **2017**, *14* (1), 1–5. https://doi.org/10.1080/17425247.2017.1262346.

(7) Owen, S. C.; Chan, D. P. Y.; Shoichet, M. S. Polymeric Micelle Stability. *Nano Today* **2012**, *7* (1), 53–65. https://doi.org/10.1016/j.nantod.2012.01.002.

(8) Karimi, M.; Ghasemi, A.; Zangabad, P. S.; Rahighi, R.; Basri, S. M. M.; Mirshekari, H.; Amiri, M.; Pishabad, Z. S.; Aslani, A.; Bozorgomid, M.; Ghosh, D.; Beyzavi, A.; Vaseghi, A.; Aref, A. R.; Haghani, L.; Bahrami, S.; Hamblin,

M. R. Smart Micro/Nanoparticles in Stimulus-Responsive Drug/Gene Delivery Systems. *Chem. Soc. Rev.* **2016**, *45* (5), 1457–1501. https://doi.org/10.1039/C5CS00798D.

(9) Zhou, S.; Shang, Q.; Wang, N.; Li, Q.; Song, A.; Luan, Y. Rational Design of a Minimalist Nanoplatform to Maximize Immunotherapeutic Efficacy: Four Birds with One Stone. *Journal of Controlled Release* **2020**, *328*, 617–630. https://doi.org/10.1016/j.jconrel.2020.09.035.

(10) Shang, Q.; Zhou, S.; Jiang, Y.; Wang, D.; Wang, J.; Song, A.; Luan, Y. Rational Design of a Robust Antibody-like Small-Molecule Inhibitor Nanoplatform for Enhanced Photoimmunotherapy. *ACS Appl. Mater. Interfaces* **2020**, *12* (36), 40085–40093. https://doi.org/10.1021/acsami.0c11156.

(11) Jiang, Y.; Huang, C.; Luan, Y. <p>Lactosylated IR820/DOX Co-Assembled Nanodrug for Synergetic Antitumour Therapy</P>. *IJN* **2020**, *15*, 4431–4440. https://doi.org/10.2147/IJN.S247617.

(12) Stuart, M. a C.; Huck, W. T. S.; Genzer, J.; Müller, M.; Ober, C.; Stamm, M.; Sukhorukov, G. B.; Szleifer, I.; Tsukruk, V. V; Urban, M.; Winnik, F.; Zauscher, S.; Luzinov, I.; Minko, S. Emerging Applications of Stimuli-Responsive Polymer Materials. *Nature materials* **2010**, *9* (2), 101–113. https://doi.org/10.1038/nmat2614.

(13) Movassaghian, S.; Merkel, O. M.; Torchilin, V. P. Applications of Polymer Micelles for Imaging and Drug Delivery. *Wiley Interdisciplinary Reviews: Nanomedicine and Nanobiotechnology* **2015**, *7* (5), 691–707. https://doi.org/10.1002/wnan.1332.

(14) Brooks, W. L. A.; Vancoillie, G.; Kabb, C. P.; Hoogenboom, R.; Sumerlin, B. S. Triple Responsive Block Copolymers Combining PH-Responsive, Thermoresponsive, and Glucose-Responsive Behaviors. *Journal of Polymer Science Part A: Polymer Chemistry* **2017**, *55* (14), 2309–2317. https://doi.org/10.1002/pola.28615.

(15) Gillies, E. R.; Fréchet, J. M. J. PH-Responsive Copolymer Assemblies for Controlled Release of Doxorubicin. *Bioconjugate Chemistry* **2005**, *16*, 361–368. https://doi.org/10.1021/bc049851c.

(16) Müller, S. S.; Fritz, T.; Gimnich, M.; Worm, M.; Helm, M.; Frey, H. Biodegradable Hyperbranched Polyether-Lipids with in-Chain PH-Sensitive Linkages. *Polym. Chem.* **2016**, *7* (40), 6257–6268. https://doi.org/10.1039/C6PY01308B.

(17) Ko, J.; Park, K.; Kim, Y. S.; Kim, M. S.; Han, J. K.; Kim, K.; Park, R. W.; Kim, I. S.; Song, H. K.; Lee, D. S.; Kwon, I. C. Tumoral Acidic Extracellular PH Targeting of PH-Responsive MPEG-Poly(β-Amino Ester) Block Copolymer Micelles for Cancer Therapy. *Journal of Controlled Release* **2007**, *123*, 109–115. https://doi.org/10.1016/j.jconrel.2007.07.012.

(18) Boerman, M. A.; Van der Laan, H. L.; Bender, J. C. M. E.; Hoogenboom, R.; Jansen, J. A.; Leeuwenburgh, S. C.; Van Hest, J. C. M. Synthesis of PH- and Thermoresponsive Poly(2- n -Propyl-2-Oxazoline) Based Copolymers. *Journal of Polymer Science Part A: Polymer Chemistry* **2016**, *54* (11), 1573–1582. https://doi.org/10.1002/pola.28011.

(19) André, X.; Zhang, M.; Müller, A. H. E. Thermo- and PH-Responsive Micelles of Poly(Acrylic Acid)-Block-Poly(N,N- Diethylacrylamide). *Macromolecular Rapid Communications* **2005**, *26*, 558–563. https://doi.org/10.1002/marc.200400510.

(20) Wang, C.; Zhang, G.; Liu, G.; Hu, J.; Liu, S. Photo- and Thermo-Responsive Multicompartment Hydrogels for Synergistic Delivery of Gemcitabine and Doxorubicin. *Journal of Controlled Release* **2017**, *259*, 149–159. https://doi.org/10.1016/J.JCONREL.2016.11.007.

(21) Qiao, J.; Qi, L.; Shen, Y.; Zhao, L.; Qi, C.; Shangguan, D.; Mao, L.; Chen, Y. Thermal Responsive Fluorescent Block Copolymer for Intracellular Temperature Sensing. *Journal of Materials Chemistry* **2012**, *22* (23), 11543–11549. https://doi.org/10.1039/c2jm31093g.

(22) Khatun, Z.; Choi, Y. S.; Kim, Y. G.; Yoon, K.; Nurunnabi, M.; Li, L.; Lee, E.; Kang, H. C.; Huh, K. M. Bioreducible Poly(Ethylene Glycol)–Triphenylphosphonium Conjugate as a Bioactivable Mitochondria-Targeting Nanocarrier. *Biomacromolecules* **2017**, acs.biomac.6b01324. https://doi.org/10.1021/acs.biomac.6b01324.

(23) Sun, B.; Luo, C.; Yu, H.; Zhang, X.; Chen, Q.; Yang, W.; Wang, M.; Kan, Q.; Zhang, H.; Wang, Y.; He, Z.; Sun, J. Disulfide Bond-Driven Oxidation- and Reduction-Responsive Prodrug Nanoassemblies for Cancer Therapy. *Nano Letters* **2018**, acs.nanolett.8b00737. https://doi.org/10.1021/acs.nanolett.8b00737.

(24) Porsch, C.; Zhang, Y.; Montañez, M. I.; Malho, J.-M.; Kostiainen, M. A.; Nyström, A. M.; Malmström, E. Disulfide-Functionalized Unimolecular Micelles as Selective Redox-Responsive Nanocarriers. *Biomacromolecules* **2015**, *16* (9), 2872–2883. https://doi.org/10.1021/acs.biomac.5b00809.

(25) Zhang, P.; Zhang, H.; He, W.; Zhao, D.; Song, A.; Luan, Y. Disulfide-Linked Amphiphilic Polymer-Docetaxel Conjugates Assembled Redox-Sensitive Micelles for Efficient Antitumor Drug Delivery. *Biomacromolecules* **2016**, *17* (5), 1621–1632. https://doi.org/10.1021/acs.biomac.5b01758.

(26) Roy, D.; Cambre, J. N.; Sumerlin, B. S. Future Perspectives and Recent Advances in Stimuli-Responsive Materials. *Progress in Polymer Science* **2010**, *35* (1), 278–301. https://doi.org/10.1016/j.progpolymsci.2009.10.008.

(27) Mu, J.; Lin, J.; Huang, P.; Chen, X. Development of Endogenous Enzyme-Responsive Nanomaterials for Theranostics. *Chemical Society Reviews*. Royal Society of Chemistry 2018, pp 5554–5573. https://doi.org/10.1039/c7cs00663b.

(28) Kumar, V.; Munkhbat, O.; Secinti, H.; Thayumanavan, S. Disassembly of Polymeric Nanoparticles with Enzyme-Triggered Polymer Unzipping: Polyelectrolyte Complexes: Vs. Amphiphilic Nanoassemblies. *Chemical Communications* **2020**, *56* (60), 8456–8459. https://doi.org/10.1039/d0cc03257c.

(29) Samarajeewa, S.; Zentay, R. P.; Jhurry, N. D.; Li, A.; Seetho, K.; Zou, J.; Wooley, K. L. Programmed Hydrolysis of Nanoassemblies by Electrostatic Interaction-Mediated Enzymatic-Degradation. *Chemical communications*

(Cambridge, England) **2014**, *50* (8), 968–970. https://doi.org/10.1039/c3cc46013d.

(30) Kessenbrock, K.; Plaks, V.; Werb, Z. Matrix Metalloproteinases: Regulators of the Tumor Microenvironment. *Cell* **2010**, *141* (1), 52–67. https://doi.org/10.1016/j.cell.2010.03.015.

(31) Hu, Q.; Katti, P. S.; Gu, Z. Enzyme-Responsive Nanomaterials for Controlled Drug Delivery. *Nanoscale* **2014**, *6* (21), 12273–12286. https://doi.org/10.1039/c4nr04249b.

(32) de la Rica, R.; Aili, D.; Stevens, M. M. Enzyme-Responsive Nanoparticles for Drug Release and Diagnostics. *Advanced Drug Delivery Reviews* **2012**, *64* (11), 967–978. https://doi.org/10.1016/j.addr.2012.01.002.

(33) Kataoka, K.; Harada, A.; Nagasaki, Y. Block Copolymer Micelles for Drug Delivery: Design, Characterization and Biological Significance. *Advanced Drug Delivery Reviews* **2012**, *64*, 37–48. https://doi.org/10.1016/j.addr.2012.09.013.

(34) Shi, Y.; Lammers, T.; Storm, G.; Hennink, W. E. Physico-Chemical Strategies to Enhance Stability and Drug Retention of Polymeric Micelles for Tumor-Targeted Drug Delivery. *Macromolecular Bioscience* **2017**, *17* (1), 1600160. https://doi.org/10.1002/mabi.201600160.

(35) Gref, R.; Domb, a.; Quellec, P.; Blunk, T.; Müller, R. H.; Verbavatz, J. M.; Langer, R. The Controlled Intravenous Delivery of Drugs Using PEG-Coated Sterically Stabilized Nanospheres. *Advanced Drug Delivery Reviews* **2012**, *64* (95), 316–326. https://doi.org/10.1016/j.addr.2012.09.008.

(36) Lee, H. Molecular Simulations of PEGylated Biomolecules, Liposomes, and Nanoparticles for Drug Delivery Applications. *Pharmaceutics* **2020**, *12* (6), 533. https://doi.org/10.3390/pharmaceutics12060533.

(37) Caponi, P.-F.; Winnik, F. M.; Ulijn, R. V. Charge Complementary Enzymatic Reconfigurable Polymeric Nanostructures. *Soft Matter* **2012**, *8*, 5127. https://doi.org/10.1039/c2sm07460e.

(38) Sedlacek, O.; Hoogenboom, R. Drug Delivery Systems Based on Poly(2-Oxazoline)s and Poly(2-Oxazine)s. *Advanced Therapeutics* **2019**, 1900168. https://doi.org/10.1002/adtp.201900168.

(39) Luxenhofer, R.; Schulz, A.; Roques, C.; Li, S.; Bronich, T. K.; Batrakova, E. V.; Jordan, R.; Kabanov, A. V. Doubly Amphiphilic Poly(2-Oxazoline)s as High-Capacity Delivery Systems for Hydrophobic Drugs. *Biomaterials* **2010**, *31* (18), 4972–4979. https://doi.org/10.1016/j.biomaterials.2010.02.057.

(40) Zhou, Z.; Munyaradzi, O.; Xia, X.; Green, D.; Bong, D. High-Capacity Drug Carriers from Common Polymer Amphiphiles. *Biomacromolecules* **2016**, *17* (9), 3060–3066. https://doi.org/10.1021/acs.biomac.6b00960.

(41) R. Ramireddy, R.; Raghupathi, K. R.; Torres, D. A.; Thayumanavan, S. Stimuli Sensitive Amphiphilic Dendrimers. *New Journal of Chemistry* **2012**, *36*, 340. https://doi.org/10.1039/c2nj20879b.

(42) Machado, C. A.; Smith, I. R.; Savin, D. A. Self-Assembly of Oligo- and Polypeptide-Based Amphiphiles: Recent Advances and Future Possibilities. *Macromolecules*. American Chemical Society March 12, 2019, pp 1899–1911. https://doi.org/10.1021/acs.macromol.8b02043.

(43) Choi, J.; Moquin, A.; Bomal, E.; Na, L.; Maysinger, D.; Kakkar, A. Telodendrimers for Physical Encapsulation and Covalent Linking of Individual or Combined Therapeutics. *Molecular Pharmaceutics* **2017**, *14* (8), 2607–2615. https://doi.org/10.1021/acs.molpharmaceut.7b00019.

(44) Bolu, B.; Sanyal, R.; Sanyal, A. Drug Delivery Systems from Self-Assembly of Dendron-Polymer Conjugates. *Molecules* **2018**, *23* (7), 1570. https://doi.org/10.3390/molecules23071570.

(45) Photos, P. J.; Bacakova, L.; Discher, B.; Bates, F. S.; Discher, D. E. Polymer Vesicles in Vivo: Correlations with PEG Molecular Weight. *Journal of Controlled Release* **2003**, *90*, 323–334. https://doi.org/10.1016/S0168-3659(03)00201-3.

(46) Ke, P. C.; Lin, S.; Parak, W. J.; Davis, T. P.; Caruso, F. A Decade of the Protein Corona. *ACS Nano* **2017**, *11* (12), 11773–11776. https://doi.org/10.1021/acsnano.7b08008.

(47) Nyström, A. M.; Wooley, K. L. The Importance of Chemistry in Creating Well-Defined Nanoscopic Embedded Therapeutics: Devices Capable of the Dual Functions of Imaging and Therapy. *Accounts of Chemical Research* **2011**, *44* (10), 969–978. https://doi.org/10.1021/ar200097k.

(48) Buzhor, M.; Harnoy, A. J.; Tirosh, E.; Barak, A.; Schwartz, T.; Amir, R. J. Supramolecular Translation of Enzymatically Triggered Disassembly of Micelles into Tunable Fluorescent Responses. *Chemistry – A European Journal* **2015**, *21* (44), 15633–15638. https://doi.org/10.1002/chem.201502988.

(49) Feiner-Gracia, N.; Buzhor, M.; Fuentes, E.; Pujals, S.; Amir, R. J.; Albertazzi, L. Micellar Stability in Biological Media Dictates Internalization in Living Cells. *J. Am. Chem. Soc.* **2017**, *139* (46), 16677–16687. https://doi.org/10.1021/jacs.7b08351.

(50) Gillies, E. R.; Jonsson, T. B.; Fréchet, J. M. J. Stimuli-Responsive Supramolecular Assemblies of Linear-Dendritic Copolymers. *J. Am. Chem. Soc.* **2004**, *126* (38), 11936–11943. https://doi.org/10.1021/ja0463738.

(51) Morgese, G.; Verbraeken, B.; Ramakrishna, S. N.; Gombert, Y.; Cavalli, E.; Rosenboom, J.-G.; Zenobi-Wong, M.; Spencer, N. D.; Hoogenboom, R.; Benetti, E. M. Chemical Design of Non-Ionic Polymer Brushes as Biointerfaces: Poly(2-Oxazine)s Outperform Both Poly(2-Oxazoline)s and PEG. *Angewandte Chemie International Edition* **2018**, *57* (36), 11667–11672. https://doi.org/10.1002/anie.201805620.

(52) Amir, R. J. Enzyme-Responsive PEG–Dendron Hybrids as a Platform for Smart Nanocarriers. *Synlett* **2015**, *26* (19), 2617–2622. https://doi.org/10.1055/s-0035-1560522.

(53) Segal, M.; Avinery, R.; Buzhor, M.; Shaharabani, R.; Harnoy, A. J.; Tirosh, E.; Beck, R.; Amir, R. J. Molecular Precision and Enzymatic Degradation: From Readily to Undegradable Polymeric Micelles by Minor Structural Changes. *J. Am. Chem. Soc.* **2017**, *139* (2), 803–810. https://doi.org/10.1021/jacs.6b10624.

(54) Lübtow, M. M.; Keßler, L.; Appelt-Menzel, A.; Lorson, T.; Gangloff, N.; Kirsch, M.; Dahms, S.; Luxenhofer, R. More Is Sometimes Less: Curcumin and Paclitaxel Formulations Using Poly(2-Oxazoline) and Poly(2-Oxazine)-Based

Amphiphiles Bearing Linear and Branched C9 Side Chains. *Macromolecular Bioscience* **2018**, *18* (11), 1800155. https://doi.org/10.1002/mabi.201800155.

(55) Seo, Y.; Schulz, A.; Han, Y.; He, Z.; Bludau, H.; Wan, X.; Tong, J.; Bronich, T. K.; Sokolsky, M.; Luxenhofer, R.; Jordan, R.; Kabanov, A. V. Poly(2-Oxazoline) Block Copolymer Based Formulations of Taxanes: Effect of Copolymer and Drug Structure, Concentration, and Environmental Factors. *Polymers for Advanced Technologies* **2015**, *26* (7), 837–850. https://doi.org/10.1002/pat.3556.

(56) Hahn, L.; Lübtow, M. M.; Lorson, T.; Schmitt, F.; Appelt-Menzel, A.; Schobert, R.; Luxenhofer, R. Investigating the Influence of Aromatic Moieties on the Formulation of Hydrophobic Natural Products and Drugs in Poly(2-Oxazoline)-Based Amphiphiles. *Biomacromolecules* **2018**, *19* (7), 3119–3128. https://doi.org/10.1021/acs.biomac.8b00708.

(57) Singla, A. K.; Garg, A.; Aggarwal, D. Paclitaxel and Its Formulations. *International Journal of Pharmaceutics* **2002**, *235* (1), 179–192. https://doi.org/10.1016/S0378-5173(01)00986-3.

(58) Shi, Y.; Lammers, T.; Storm, G.; Hennink, W. E. Physico-Chemical Strategies to Enhance Stability and Drug Retention of Polymeric Micelles for Tumor-Targeted Drug Delivery. *Macromolecular Bioscience* **2017**, *17* (1), 1600160. https://doi.org/10.1002/mabi.201600160.

(59) Haider, M. S.; Lübtow, M. M.; Endres, S.; Forster, S.; Flegler, V. J.; Böttcher, B.; Aseyev, V.; Pöppler, A.-C.; Luxenhofer, R. Think Beyond the Core: Impact of the Hydrophilic Corona on Drug Solubilization Using Polymer Micelles. *ACS Appl. Mater. Interfaces* **2020**, *12* (22), 24531–24543. https://doi.org/10.1021/acsami.9b22495.

(60) Cao, C.; Zhao, J.; Chen, F.; Lu, M.; Khine, Y. Y.; Macmillan, A.; Garvey, C. J.; Stenzel, M. H. Drug-Induced Morphology Transition of Self-Assembled Glycopolymers: Insight into the Drug–Polymer Interaction. *Chem. Mater.* **2018**, *30* (15), 5227–5236. https://doi.org/10.1021/acs.chemmater.8b01882.

(61) Vilanova, O.; Mittag, J. J.; Kelly, P. M.; Milani, S.; Dawson, K. A.; Rädler, J. O.; Franzese, G. Understanding the Kinetics of Protein–Nanoparticle Corona Formation. *ACS Nano* **2016**, *10* (12), 10842–10850. https://doi.org/10.1021/acsnano.6b04858.

(62) O'Brien, J.; Lee, S.-H.; Onogi, S.; Shea, K. J. Engineering the Protein Corona of a Synthetic Polymer Nanoparticle for Broad-Spectrum Sequestration and Neutralization of Venomous Biomacromolecules. *J. Am. Chem. Soc.* **2016**, *138* (51), 16604–16607. https://doi.org/10.1021/jacs.6b10950.

(63) Obst, K.; Yealland, G.; Balzus, B.; Miceli, E.; Dimde, M.; Weise, C.; Eravci, M.; Bodmeier, R.; Haag, R.; Calderón, M.; Charbaji, N.; Hedtrich, S. Protein Corona Formation on Colloidal Polymeric Nanoparticles and Polymeric Nanogels: Impact on Cellular Uptake, Toxicity, Immunogenicity, and Drug Release Properties. *Biomacromolecules* **2017**, *18* (6), 1762–1771. https://doi.org/10.1021/acs.biomac.7b00158.

(64) Settanni, G.; Zhou, J.; Suo, T.; Schöttler, S.; Landfester, K.; Schmid, F.; Mailänder, V. Protein Corona Composition of Poly(Ethylene Glycol)- and Poly(Phosphoester)-Coated Nanoparticles Correlates Strongly with the Amino

Acid Composition of the Protein Surface. *Nanoscale* **2017**, *9* (6), 2138–2144. https://doi.org/10.1039/C6NR07022A.

(65) Schöttler, S.; Becker, G.; Winzen, S.; Steinbach, T.; Mohr, K.; Landfester, K.; Mailänder, V.; Wurm, F. R. Protein Adsorption Is Required for Stealth Effect of Poly(Ethylene Glycol)- and Poly(Phosphoester)-Coated Nanocarriers. *Nature Nanotech* **2016**, *11* (4), 372–377. https://doi.org/10.1038/nnano.2015.330.

(66) Liu, B.; Thayumanavan, S. Importance of Evaluating Dynamic Encapsulation Stability of Amphiphilic Assemblies in Serum. *Biomacromolecules* **2017**, *18* (12), 4163–4170. https://doi.org/10.1021/acs.biomac.7b01220.

(67) Teunissen, A. J. P.; Pérez-Medina, C.; Meijerink, A.; Mulder, W. J. M. Investigating Supramolecular Systems Using Förster Resonance Energy Transfer. *Chem. Soc. Rev.* **2018**, *47* (18), 7027–7044. https://doi.org/10.1039/C8CS00278A.

(68) Guo, J.; Zhuang, J.; Wang, F.; Raghupathi, K. R.; Thayumanavan, S. Protein AND Enzyme Gated Supramolecular Disassembly. *J. Am. Chem. Soc.* **2014**, *136* (6), 2220–2223. https://doi.org/10.1021/ja4108676.

(69) Molla, M. R.; Prasad, P.; Thayumanavan, S. Protein-Induced Supramolecular Disassembly of Amphiphilic Polypeptide Nanoassemblies. *J. Am. Chem. Soc.* **2015**, *137* (23), 7286–7289. https://doi.org/10.1021/jacs.5b04285.

(70) Amado Torres, D.; Garzoni, M.; Subrahmanyam, A. V.; Pavan, G. M.; Thayumanavan, S. Protein-Triggered Supramolecular Disassembly: Insights Based on Variations in Ligand Location in Amphiphilic Dendrons. *J. Am. Chem. Soc.* **2014**, *136* (14), 5385–5399. https://doi.org/10.1021/ja500634u.

(71) Rösler, A.; Vandermeulen, G. W. M.; Klok, H.-A. Advanced Drug Delivery Devices via Self-Assembly of Amphiphilic Block Copolymers. *Advanced Drug Delivery Reviews* **2012**, *64*, 270–279. https://doi.org/10.1016/j.addr.2012.09.026.

Chapter 3. Mobility of polymeric micelles inside an *in vitro* tumor-on-a-chip model with dual ECM

The chapter reproduces almost identically the article (in preparation):
Reaching the tumour: mobility of polymeric micelles inside an in vitro tumor-on-a-chip model with dual ECM. Alis R. Olea, Alicia Jurado, Gadi Slor, Shahar Tevet, Silvia Pujals, Roey Amir, Lorenzo Albertazzi (2023)

All experiments presented in this chapter were done by myself, together with the master student Alicia Jurado, except for the tri-block copolymer experiments, which I tested alone.

The synthesis of the first 6 polymeric micelles was performed by Gadi Slor and synthesis of the tri-block copolymers was done by Shahar Tevet, both part of the group of Roey Amir in Tel Aviv University.

INTRODUCTION

In the last seven decades, nanoparticles received increasing attention as possible vehicles to transport drugs in a targeted manner, and serve as drug delivery systems (DDSs) for cancer treatment.[1] Their use promises to alleviate side effects caused by systemic administration and to increase the therapy effectiveness.

Despite the intensive research, only a handfull of DDSs reached the clinic. One of the reasons that makes DDS design very challenging is the lack of comprehensive testing platforms. While *in vivo* experiments using animal models are widely used for mimicking the tumor environment, differences to the human counterparts, the complex protocols as well as ethical issues make the emerging 3D *in vitro* platforms a more attractive tool to mimic the interactions inside the human body and predict the efficacy of the studied DDSs.[2]

Once a DDS enters the human body via intravenous injection, there are several bottlenecks it needs to surpass,[3] which were discussed in detail in **chapter 1**. In the blood circulation, DDS encounters sudden dilution, sheer stress and blood proteins, which can interact by creating a protein corona, leading to clearance by the spleen or kidneys. Then, DDS needs to extravasate at the target site, reaching the tissue barrier: extracellular matrix filtration, high intratumoral pressure, passage through several layers of cells; finally reaching the target cells, where DDS should relase the cargo to perform its intracellular activity.[4]

Although much attention was given to the circulation and cellular internalization steps, there is less focus on the tumor tissue barrier. After extravasation, the nanoparticles would reach dense layers of cells and extracellular matrix (ECM).[5] From a structural view, ECM is a mesh that gives the shape to organs and tissues and directs cellular movement. Yet, from a functional view, recent studies have shown that ECM can filter charged nanoparticles of either sign (positive or negative).[6,7] It can also trap large particles[8] or cause destabilization through hydrophobic interactions (which can cause DDSs to loose their cargo).[5]

Also, the high intratumoral pressure present in some cases can deter the entry of DDSs. It is known that cancer tissues have different, much stiffer microenvironments compared to those of normal tissues, and different matrix-associated protein composition. These features affect cell differentiation, proliferation and migration, as well as gene expression and response to anticancer drugs, contributing to the tumorigenic microenvironment.[9]

Often, the presence of ECM is ignored when testing anticancer formulations. Most 2D cell cultures lack a viable ECM, while animal models can have a different ECM compared to the human environment. However, ECM density was shown to directly affect tumor penetration for different sizes of polymeric micelles *in vivo*.[8] Thus, being able to test the passage of DDSs through tumor ECM would be one more step of the puzzle in aiding the design of effective DDSs. This could be achieved using an *in vitro* platform mimicking the tumor ECM in which to test the interaction with different nanoformulations.

Extracellular matrices around the body have various compositions. Thus, for designing a comprehensive test platform, there are several ECM types that should be taken into account. One of the most important is the basal lamina, which has proven nanoparticle filtration properties.[6] Basal lamina is a thin ECM layer that creates the inner lining of many epithelial, muscle and endothelial tissues, including the wall of blood vessels. Basal lamina is an intertwined mesh of laminin, collagen type IV and heparan sulphate chains, crosslinked by several connecting molecules.[10] The reticular mesh-like structure of basal lamina is very different from the ECM typically found inside tumors. For instance, the desmoplastic tumors such as breast cancer, pancreatic or prostate cancer have an increased deposition of molecules otherwise specific to wound healing sites,[11] resulting in the disorganized ECM of a wound that does not heal. Such molecules include a.o. collagens type I, III and V (which have a fibrilar structure) and hyaluronic acid (especially ones with low molecular weight, which promote inflamation,[12] but also high molecular weight segments which contribute to cancer resistance).[13] These molecules create a high local pressure due to water retention, greatly affecting the flow of nutrients and signaling molecules in the area.[14]

For reconstituting the basal lamina ECM and the intra-tumoral ECM *in vitro*, widely used models are Matrigel – basement membrane extract from Engelbreth-Holm-Swarm murine sarcoma cells;[15,16] and collagen type I. Both are very well researched for their stiffness and microarchitecture formation to correspond to the tumor environment. Moreover, Matrigel is able to exhibit nanoparticle filtration effects based on NPs surface charge, while a simple mix of the basal lamina components cannot recapitulate this feature.[6] Notably, both positively and negatively charged NPs can be retained. Furthermore, size filtration and hydrophobic interactions[5] should be also taken into account. Therefore, a simple testing platform can be obtained, containing both types of ECM models and cellular spheroids, for an easy screening of DDS formulations in their ability to cross the tumor tissue barrier.

In this chapter, we are showcasing the use of a microfluidic chip platform containing dual-ECM and MCF7 spheroids for mimcking the "tumor ECM barrier". Inside this chip, we tested the mobility, ECM interactions and 3D cellular uptake of a small library of 6 polymeric micelles which were thoroughly characterized in **chapter 2**. One-to-one comparison was made between the effect of three common hydrophilic shells (PEG, PEtOx and PAA) on the interactions of polymeric micelles inside a 3D microfluidic chip with a dual-ECM model of breast cancer and MCF7 spheroids. Notably, we measured both the assembly state of the micelles and the diffusion inside ECM at the same time, by using ratiometric imaging and FRAP. We observed differences in the interaction behavior of different micelles with ECM components, especially for the basal lamina model. Lastly, we tested a more stable PAA micelle design, increasing our understanding of the micelle mobility and interactions with ECM.

RESULTS & DISCUSSION

### Experimental setup of a 3D testing platform

As a main focus in our choise of platform design is the intention to have a simple platform to allow higher throughput, yet complex enough to provide three-dimensional information otherwise inaccesible in a 2D cell culture setting. In order to model the tumor ECM barrier in a simple *in vitro* testing platform, we used two ECM types and breast cancer MCF7 spheroids inside a microfluidic device.

Notably, we intended to mimick the tissue barrier without the extravasation step through the endothelial layer which has been addressed by our group in a previous study.[17]

As microfluidic device, we used the commercially available DAX-1 microfluidic chip model from AIM Biotech. DAX-1 has several advantages, especially the ease of reproducibility, being optically transparent (unlike other chips made of PDMS) and having a bottom permeable to CO_2/O_2, making it compatible with live cell culture. Also, the platform is versatile enough to implement our idea of dual ECM, as the chip has three microfluidic channels separated by triangular pillars, which allow filling the channels with separate types of gel (Figure 3.1A). The middle channel is 1.3 mm wide, while both side channels are 0.5 mm wide.

We filled the middle channel with a gel model for basal lamina: reconstituted ECM from Engelbreth-Holm-Swarm murine sarcoma cells. After gelation of the middle channel, we filled one of the side-channels with a gel model for desmoplatic tumors, a mix of rat tail collagen type I and hyaluroinc acid. In this "tumor ECM" gel we embedded MCF7 spheroids as a widely used model for breast cancer (Figure 1B). In order to obtain a collagen gel microarchitecture resembling solid tumors, we performed the gelation of the collagen mix using a final collagen concentration of 2.5 mg/mL at pH 7.4 and 37° C.[18]

After gelation, we used the remaining side-channel for adding the solution of polymeric micelles in cell media (full DMEM, with 10% FBS). After equilibration time overnight, we performed two types of measurements in a confocal microscope: ratiometric imaging for determining the local assembly state of the micelles and fluorescence recovery after photobleaching (FRAP) for measuring unimer and micelle dynamics in different parts of the chip (Figure 3.1).
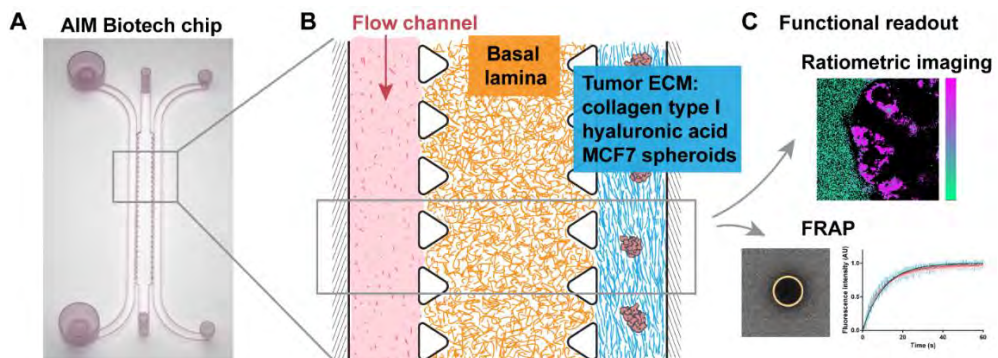

Figure 3.1. Experimental setup. A commercial microfluidic chip from AIM Biotech, with three channels separated by triangular pillars (A) is filled in the middle channel with a model of basal lamina ECM from Engelbreth-Holm-Swarm murine sarcoma cells at 5.25 mg/mL and in the right side-channel with a gel mix of collagen type I (2.5 mg/mL, pH 7.4) and hyaluronic acid (0.8 mg/mL), representing the tumor ECM, in which are embedded spheroids of MCF7 breast cancer cell line (B). The micelle sample is added to the flow channel as a 160µM solution in full DMEM (10% FBS) and allowed to diffuse for 24h before doing a functional readout in the confocal microscope, either as ratiometric imaging or as fluorescence recovery after photobleaching (FRAP) in different locations inside the chip (C).

Chip validation

Before testing micelle's interactions in the dual-ECM chip, we assessed the integrity of the proposed 3D model. In order to validate if the two types of ECM gels are located in the correct compartment after dual-step filling the chip, we labeled each gel mix with either Cy3 or Cy5 dyes using EDC/NHS reaction. This way, all the components of the basal lamina gel and "tumor ECM" mix should be visible. A transversal view inside the gel-filled chip revealed that the two gel types remained in the expected chip compartments, in the middle channel and side-channel respectively, without mixing (Figure 3.2A, B).

Another step to validate the chip model was to assess spheroid viability and growth. We used a live/dead assay with calcein and propidium iodide in order to visualize the viable and dead MCF7 cells respectively inside the chip (Figure 3.2C). We concluded that most cells remained viable. This is supported also by observing the spheroid growth from 0 to 48h inside the chip (Figure 3.2D). Based on the growth images, we decided to use the 24h time point for micelle measurements in the chip, since at 48h the spheroids seem to loose the round shape.
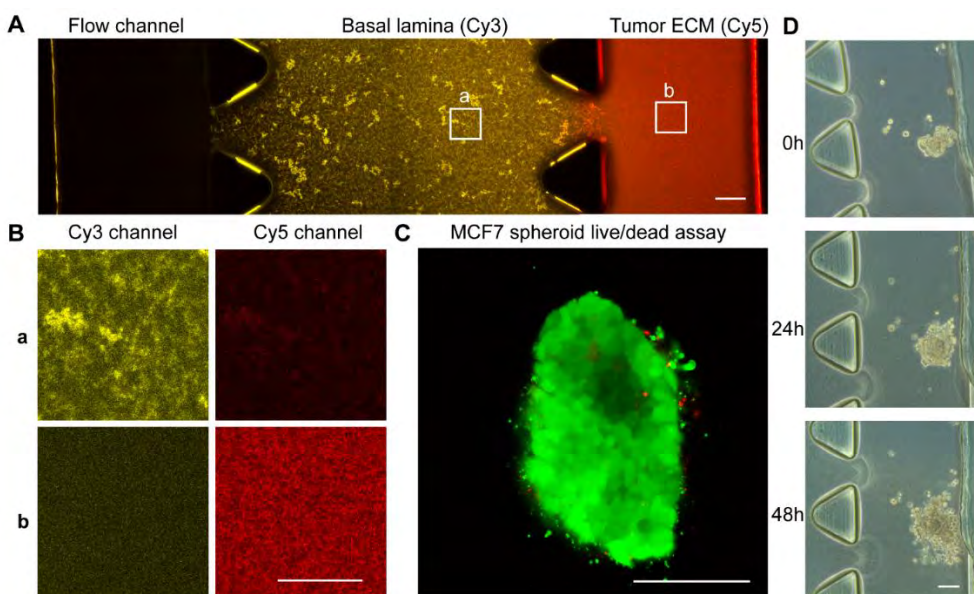
Figure 3.2. Validation of ECM distribution and spheroid viability inside the chip. (A) Overview of ECM distribution inside the chip using Cy3-labeled basal lamina gel (ECM from Engelbreth-Holm-Swarm murine sarcoma cells) and Cy5-labeled tumor ECM model (mix of collagen type I and hyaluronic acid), labeled using

83

EDC/NHS reaction. (B) Zoom into (a) Basal lamina and (b) tumor ECM, showing the fluorescence in Cy3 (yellow) and Cy5 (red) channels. (C) Live/dead assay of MCF7 spheroid inside tumor ECM channel, after 24h inside chip, stained with calcein (green) and propidium iodide (red) (image shown after log transformation). (D) MCF7 spheroid growth inside tumor ECM channel. Scale bar is 100 µm for A, C, D and 50 µm for B.

Micelles characterization

The dual-ECM microfluidic chip model allowed us to compare the penetration capacity of different micelle formulations into a relevant model of tumor extracellular environment, while also comparing the micelle's internalization capacity in 3D spheroids. Figure 3.3 presents a graphical overview of the molecular design of the micelles investigated in this study, the same micelle library described in **chapter 2**.

Briefly, three widely known polymers: polyethylene glycol (PEG), poly-ethyl-oxazoline (PEtOx) and polyacrylic acid (PAA) with similar moelcular weigths were used as the shell forming hydrophilic blocks. The hydrophilic polymers of same molecular weight were clicked together with a hydrophobic dendron with four esterase-cleavable chains of either 6 ("Hex") or 9 carbons ("Non") in length (Figure 3.2). Their synthesis was previously described in detail.[19]

As explained in the previous chapter, an additional important aspect in our choice of micelle design is the fluorescent label 7(diethylamino)coumarin-3-carboxylic acid (7-DEAC) which changes the emission spectra due to excimer formation when dyes are in close proximity inside the micelle.[20,21] The emission peak thus reflects the micelle assembly state: 480 nm for unimer form and ~540 nm for micelle. This allows to visualize if micelles disassemble at different locations inside the chip. Overall, the well-defined structure and the fluorescence reporter mechanism gave us the advantage of distinguishing between the effects of different hydrophilic shells from the hydrophobicity of the micelle core.

The micelle size and charge were assessed by dynamic light scattering (DLS) and Zeta potential measurements using a micelle solution obtained through self-assembly in PBS (pH 7.4) at 80 µM. DLS measurements showed that micelle size is in the

range of 10-30 nm (Table 3.1), which were similar to our previous measuremnets,[19] presented in **chapter 2**.

Based on their dimensions, we would not expect them to be trapped based on size inside the ECM gels, which under current conditions would have the pore size of a few µm.[22] Instead, interactions with ECM would be due to charge or hydrophobicity.

		PEtOx-Hex		PEtOx-Non		PEG-Hex		PEG-Non		PAA-Hex		PAA-Non	
DLS	Mean	SD	Mean	SD	Mean	SD	Mean	SD	Mean	SD	Mean	SD
(nm)	16.56	0.9469	18.47	1.305	16.69	2.599	25.02	3.47	16.22	1.191	11.06	1.656
Z potential	Mean	SD	Mean	SD	Mean	SD	Mean	SD	Mean	SD	Mean	SD
(mV)	-7.55	0.86	-8.95	1.01	-6.99	0.98	-8.81	1.2	-29.7	3.31	-25.2	2.48

Table 3.1. DLS and Z potential measurements of micelle solution in PBS pH 7.4, 80 µM.

For assessing micelle surface charge, we performed Zeta potential measurements. As expected, PEtOx and PEG micelles showed rather neutral surface charges (-7 to -9 mV in PBS), while PAA polymers had a negative surface charge, with an average of -29 mV for PAA-Hex and -25 mV for PAA-Non (Figure 3.3B). Overall, the size and charge of the micelles are consistent with our previous study, allowing us to assess the interactions with the different types of ECM in our chip model.
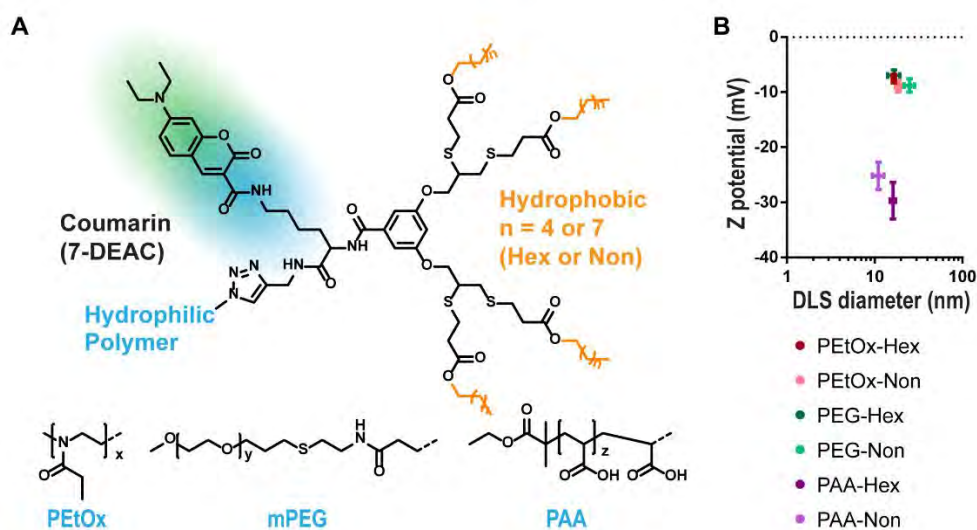
Figure 3.3. Micelle structure and characterization. Chemical structure of amphiphiles formulations with 3 different hydrophilic groups (PEtOx, PEG or PAA) and 2 lengths of the hydrophobic ends ("Hex" or "Non"), labeled with 7-DEAC (A). Zeta potential measurements plotted versus hydrodynamic size by DLS of the 6 micelle formulations are shown for 80μM solutions in PBS, pH 7.4 (B).

Confocal imaging

Once the general micelle characterization was complete and micelles were confirmed to be non-toxic to MCF7 cells in a Presto Blue cytotoxicity assay (Figure 3.4), we moved on to testing micelle distribution and dynamics inside the chip. We filled the "flow channel" with micelle solution (160 μM in full DMEM, 10% FBS) and allowed micelles to distribute inside the chip via passive diffusion during 24h incubation at 37° C, 5% CO_2 . In this case, we avoided the use of a microfluidic pump, since the intention was to mimic the diffusion of nanocarriers inside tumor tissue after the extravasation step.

Using a confocal microscope we imaged the coumarin-labeled amphiphiles inside different parts of the chip with 405 nm excitation. Acquisition was split into two channels that reflect the coumarin spectral shift between unimer and micellar states, as previously explained in **chapter 2**: the unimers channel from 400 to 500 nm and the micelles channel from 500 to 700 nm respectively. As a post-processing step, we summed the two channels to create a "Total fluorescence" image in order to compare

the overall distribution and intensity. Also, we divided the unimer channel by the micelle channel to obtain a "Ratiometric" image, which indicates the spatial distribution of unimers and micelles in different chip locations.
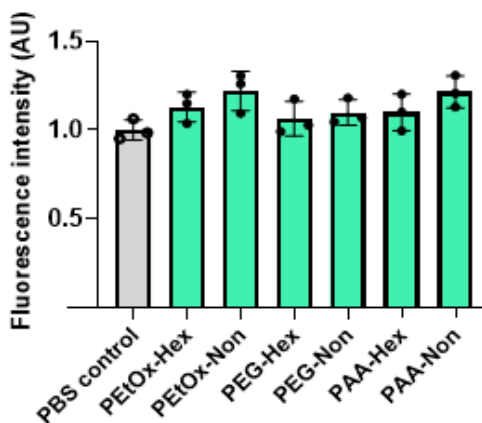
Figure 3.4. Cytotoxicity assay of micelles on MCF7 cells, assessed with Presto Blue.

Total fluorescence in basal lamina

Looking at the total fluorescence images inside the basal lamina, shown as zoom-in images in the top row of Figure 3.5A, as well as overview images of the chip in Figure 3.6, we observed an interesting difference between polymers. The more stable polymers PEtOx-Non and PEG-Non showed a "dark" structure of ECM (which was not labeled), meaning that these micelles were basically avoiding the basal lamina. In contrast, the negatively charged polymers PAA-Hex and PAA-Non showed a "bright" structure of the ECM, which suggests that they bind to the basal lamina mesh and accumulate on it. The local accumulation of PAA polymers onto the basal lamina is also supported by an overall higher fluorescence intensity compared to other chip compartments (Figure 3.5D).

The remaining polymers PEtOx-Hex and PEG-Hex were found to be in between their more stable Nonyl ananlogues and the PAA-based polymers, not showing a repulsion, but a rather homogenous distribution of fluorescent signal with occasional brighter spots (Figure 3.5A, 3.6). In this case, we can assume there is a small degree of interaction with the basal lamina, but not to the point of a visible accumulation onto the mesh structure. Overall, this would mean there is more interaction with the basal lamina ECM for Hexyl compared to Nonyl formulations, probably due to the less stable, and consequelty, more dynamic nature of the Hexyl micelles.

Notably, the small size of the micelles (15-25 nm in diameter) and free unimers (expected to be 5-10 nm) is significantly smaller than the expected pore size of the reconstituted basal lamina mesh (~2 µm).[6] Thus, we can conclude that the observed accumulation was due to ECM interactions instead of size entrapment.

### Ratiometric imaging in basal lamina

In order to differentiate if the interaction that we observed is happening more in the micellar or unimer forms, we checked the ratiometric images (Figure 3.5A bottom row). The PEtOx-Non and PEG-Non showed uniformous micelle conformation (indicated by green color), which could be expected based on being relatively more stable.

On the other hand, PAA polymers had an overall higher unimer/micelle ratio, of ~1.5 for PAA-Non and ~2 for PAA-Hex (Figure 3.5B). In this case, some disassembly is already happening in solution, probably due to their higher tendency for interaction with serum proteins,[19] as discussed in **chapter 2**. The ratio profile in the basal lamina appears more noisy for the PAA micelles/unimers, but without a clear difference in the regions corresponding to bright structures in the total fluorescence image. Thus, we concluded that PAA polymers are binding to the basal lamina in a similar equilibrium state as in media solution (predominantly in unimer form) and that the ECM binding caused further destabilization as the unimer/micelle ratios are higher than the ones in the control media (Figure 3.5D).
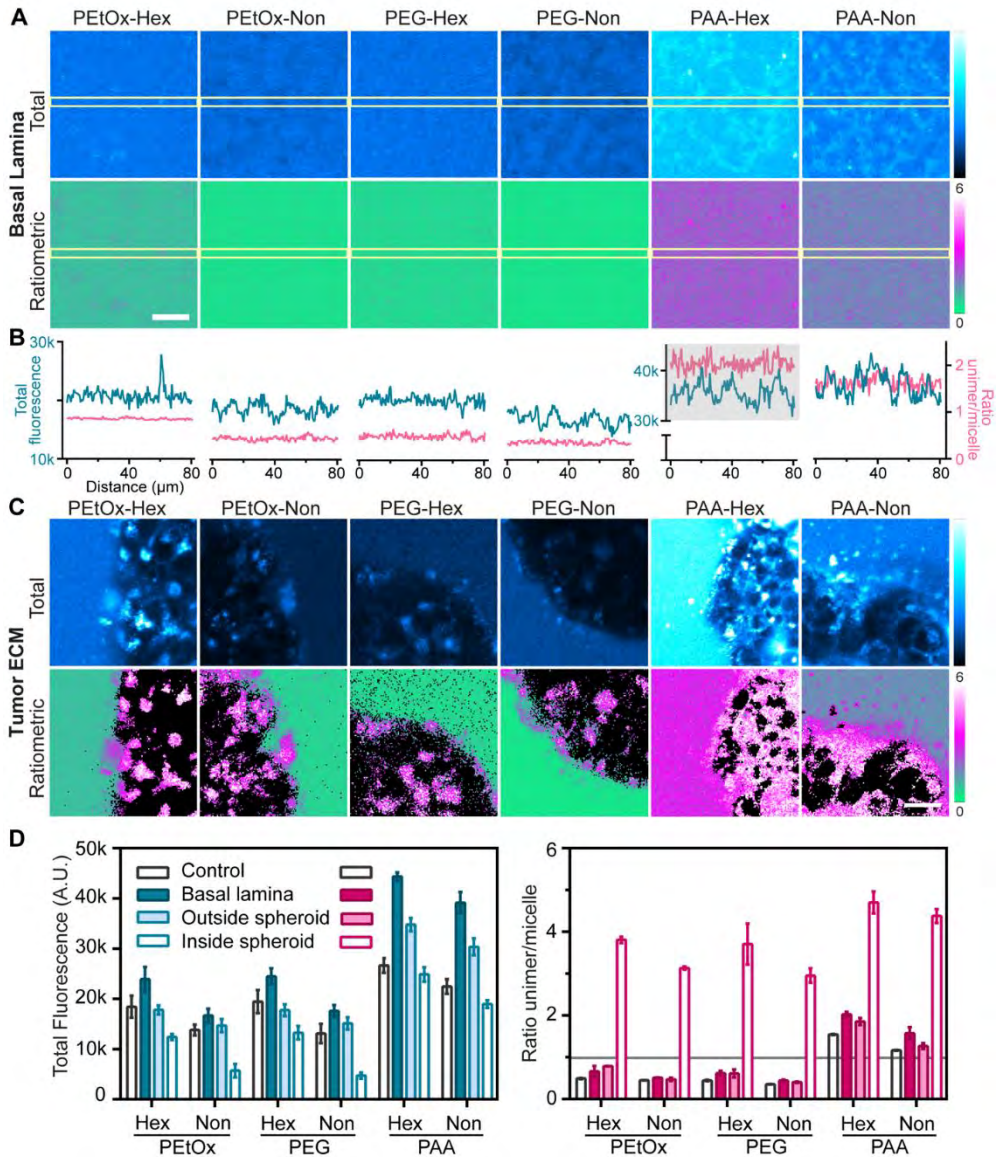
Figure 3.5. Confocal imaging of micelles inside different chip compartments.
Total fluorescence (first row) or ratiometric images of unimer/micelle pixel ratio after background removal (second row) are shown in the basal lamina compartment (A) or at the edge of an MCF7 spheroid (C). Imaging was done after 24h incubation at 160 µM in full DMEM (10% FBS). Scale bars represent 20 µm. Intensity profiles (B) of 3x80 µm rectangles inside the basal lamina compartment are shown for total fluorescence images (blue line) and ratiometric images (pink line). The mean fluorescence intensity or unimer/micelle ratio is quantified for each chip compartment (D): flow channel (control), basal lamina, tumor ECM (outside spheroids) and inside

spheroids (N≥3). A horizontal gray line is drawn for visualization purposes, corresponding to a unimer/micelle ratio if 1.
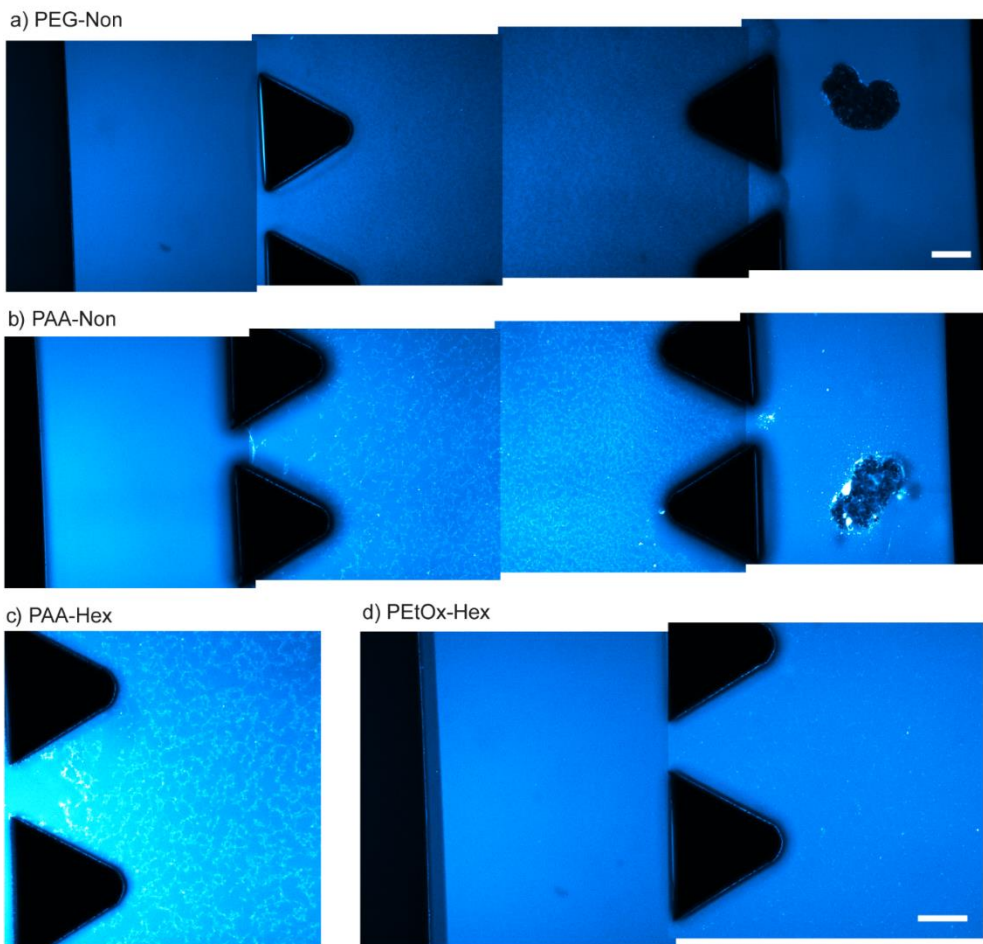
Figure 3.6: Overview images (total fluorescence) of coumarin-labeled micelles inside multigel chip model. The chip contains three channels separated by triangular pillars; the left channel contains only solution of micelles in full DMEM media, the middle channel contains a basal lamina gel model and the right channel contains MCF7 spheroids embedded in a mix of collagen type I and hyaluronic acid. The gel structure inside the middle channel was visible after micelle adition in some cases, either as a "dark" structure for more hydrophobic micelles (a – PEG-Non), or as a bright structure for PAA micelles (b – PAA-Non, c – PAA-Hex). In-between, the less hydrophobic micelles did not reveal the structure, but only a few bright spots when compared to the left channel (d – PEtOx-Hex). Scale bars represent 100 μm.

As for the PEtOx-Hex and PEG-Hex, ratiometric images showed faint traces of increased unimer signal, causing a slightly higher mean ratio in the basal lamina compartment compared to the ratio in solution (Figure 3.5D). Since PEtOx-Hex and PEG-Hex are more stable than PAA micelles, but less stable than their Nonyl analogues, we can asssume that the free unimers in solution are more likely to bind to ECM, while most micelles remain in a stable form in solution.

Overall, basal lamina binding was highly influenced by micelle surface charge, with PAA polymers showing the most binding, and also by micelle stability, with PEtOx-Hex and PEG-Hex interacting more than their Nonyl counterparts.

"Tumor ECM": collagen–HA interactions and MCF7 uptake

In the "tumor ECM" compartment of the chip, MCF7 spheroids were embedded in a mix of collagen type I and hyaluronic acid. Unlike the basal lamina compartment, our "tumor ECM" gel had no visible impact on the total fluorescence signal nor on the micelle distribution, except for PAA polymers which showed an increase in fluorescence, but nearly half compared to the increase observed in the basal lamina compartment (Figure 3.5D). In this case, the PAA micelles might be already destabilized after their passage through basal lamina.

Interestingly, when quantifying the mean unimer/micelle ratio in the "tumor ECM", all Hexyl polymers showed higher ratios (similar to the ones in basal lamina) while Nonyl polymers maintained a ratio close to control. This clearly points to the stabilizing effect of the longer hydrophobic tails leading to less ECM interactions. Overall, the "tumor ECM" gel had little impact on micelle passage.

We found differences however in the uptake behavior into MCF7 spheroids. Using the total fluorescence images, we quantified the mean intensity inside spheroids as an indicator of cellular internalization. Overall, we observed that PEtOx-Hex and PEG-Hex had similar uptake. The more stable PEtOx-Non and PEG-Non showed weaker intensities inside the spheroids, indicating on their lower degree of internalization, while PAA micelles had the highest intensity.

This is consistent with our previous uptake experiments in 2D HeLa cell cultures,[19] described in **chapter 2**, in which we also observed differences in the intracellular distribution, with PAA formulations showing membranary signal, while the others were internalized in endocytic vesicles. The 3D setting inside the chip posed imaging limitations (due to sample thickness, and the gel and spheroid densities), which did

not allow a clear assessment of the intracellular distribution, which seemingly followed the same trend.

Ratiometric images of the spheroids indicated predominant the unimer form inside cells for all polymers, with unimer/micelle ratios above 3. Having only unimers inside the cells is expected for the long incubation time used with the chip (24h). It is not excluded that polymers internalize in micelle form and break down inside the cells, but this process would be fast and difficult to capture in the given conditions.

For PAA containing polymers, the ratio was higher also outside cells due to their lower stablility during a long incubation time in full DMEM. As we showed previously with serum albumin experiments in **chapter 2**, PAA micelles tend to dissociate in solution due to protein interaction.[19]

FRAP

Next, we assessed unimer and micelle dynamics in different chip compartments using fluorescence recovery after photobleaching. Briefly, a circular bleach region of 35.3 µm was exposed to high intensity 405 nm laser, causing local photobleaching of the coumarin labels. The diffusion of amphiphiles outside of the bleached area, being replaced by ones with intact fluorescence from the surronundings, causes a local recovery of fluorescence signal. The signal was recorded using split unimer/micelle channels as explained in the confocal imaging section, in order to obtain the diffusion constants of both unimers and micelles in different chip compartments.

Firstly, looking at the normalized recovery curves shown in Figure 3.7, we can say that all of them had a complete recovery – we did not observe an immobile fraction (including PEtOx-Non and PEG-Non which had a higher signal heterogeneity, but maintained a complete recovery overall, as can be seen in the zoom out in Figure 3.8). This is indicative of the nature of the possible binding, meaning that any occuring interactions were not strong enough to immobilize the bleached molecules for the duration of the FRAP acquisition. Instead, the exchange of bright and dark amphiphiles happened rather fast.

Secondly, we observed a slightly slower recovery rate inside the basal lamina for all formulations, which is reflected in lower diffusion constants (Figure 3.9). Being present in all formulations, we can assume it to be due to geometric hindrance

imposed by the microarchitecture of the basal lamina mesh inside the bleach area. Notably, the bleach area is large enough to contain several ECM pores. However, the Hexyl amphiphiles seem to be affected more than the Nonyl ones and the difference was higher for PAA compared to PEtOx and PEG. In these cases we can assume the slower diffusion is indeed caused by interactions with basal lamina structures.

The FRAP data should be seen as reflecting the overall interactions rather than strictly the diffusion rate. By looking at the difference in size between a free unimer (expected to be 5-10 nm) and a formed micelle (15-25 nm in diameter), one might expect to observe a difference in diffusion rate in the FRAP data. However, one challenging aspect in interpreting the FRAP data is the presence of different types of interactions in our system.

One of these interactions is the dynamic equilibrium of unimers and micelles. The transition between free unimers and the ones assembled into micelles is probably happening very fast, meaning that although we measure separately the unimers and micelles fluorescence, there are probably unimers that get back into micelle form and vice-versa during the FRAP acquisition.

Another factor is the presence of serum proteins (experiments are performed in full DMEM media, with 10% FBS) which is likely influencing the measured diffusion rate. In **chapter 2**, we showed that serum albumin is binding to both unimers and micelles causing destabilization.[19] Thus, we can expect protein-bound unimers to be more bulky and diffusing slower than a free unimer. This means the diffusion constant of a protein-bound unimer can be closer to the one of a micelle with less protein interaction, which is the case for the more stable PEtOx and PEG formulations. For PAA, the charged shell causes a higher interaction with proteins, which can affect both unimers and micelles, being reflected in a clear difference of unimer to micelle diffusion constants.

Next, inside the "tumor ECM", the diffusion was generally similar to the one in solution, indicating that collagen type I and hyaluronic acid posed no hindrance to micelle diffusion. This is in accordance to the results of confocal imaging, where we observed little or no interaction with the collagen I – hyaluronic acid mix.
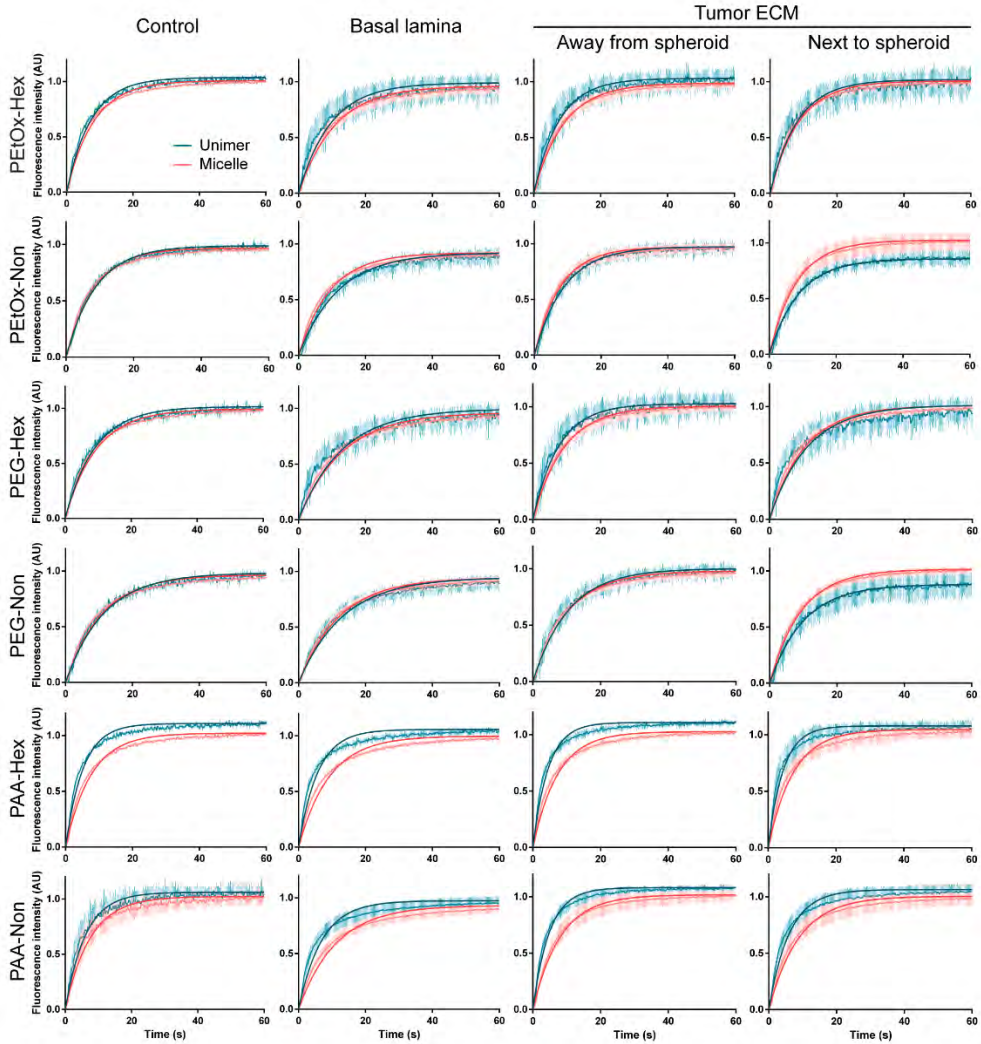
Figure 3.7. FRAP recovery curves. Unimer (blue) and micelle fluorescence (red) are represented as mean and standard deviation (faint lines), with fitted one-component exponential curve (dark lines), shown in different parts of the chip. Control measurements represent micelles in solution (in full DMEM, 10% FBS).
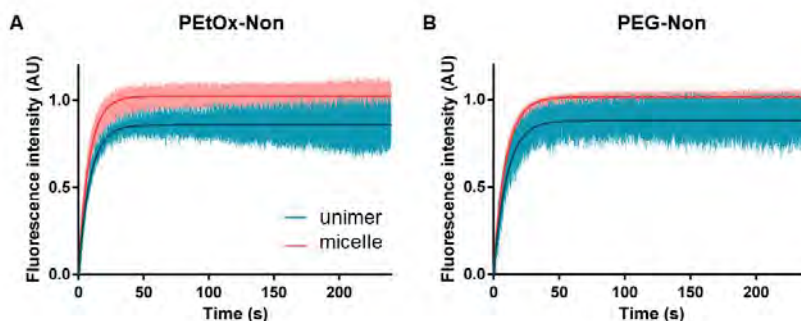
Figure 3.8. Zoom-out of FRAP recovery curves for PEtOx-Non (A) and PEG-Non (B) in collagen-HA next to spheroid, showing the mean fluorescence in the bleach area during the entire post-bleach acquisition time. Graph plotted as mean +/-SD. Unimer signal is shown in blue, while micelle signal is shown in red.

Within the "tumor ECM" compartment, we measured the diffusion close to and away from spheroids in an attempt to check if our MCF7 spheroids are affecting the ECM diffusion, by either stiffening or degrading the matrix in their proximity. However, we did not observe a difference between these locations. Other studies have shown ECM remodelling by tumor cell spheroids,[23] as well as stiffening and hindered diffusion due to collagen deposition by fibroblasts.[24] In this sense, we can conclude that our model was too simple to measure this difference. It could be too little time in the chip (24h) or the spheroid too small (due to limitations given by channel size) to have a visible impact on the ECM conformation. Probably a different cell type or a model containing co-cultures of cancer and stromal cells would be able to recapitulate these features, although with added degrees of complexity. Alternatively, nanoparticle diffusion has been studied in the ECM deposited intercelularly inside spheroids,[25] which could be an interesting approach for future studies.

Our study reveals on polymeric micelles a positive correlation between ECM binding and spheroid cellular uptake, with charged polymers (PAA) showing reversible binding to ECM and higher uptake in MCF7 spheroids. A similar correlation was found by Valente et al. for 10 nm gold nanoparticles of different surface charges[26], highlighting the importance of testing both ECM penetration and cellular uptake in relevant 3D models.
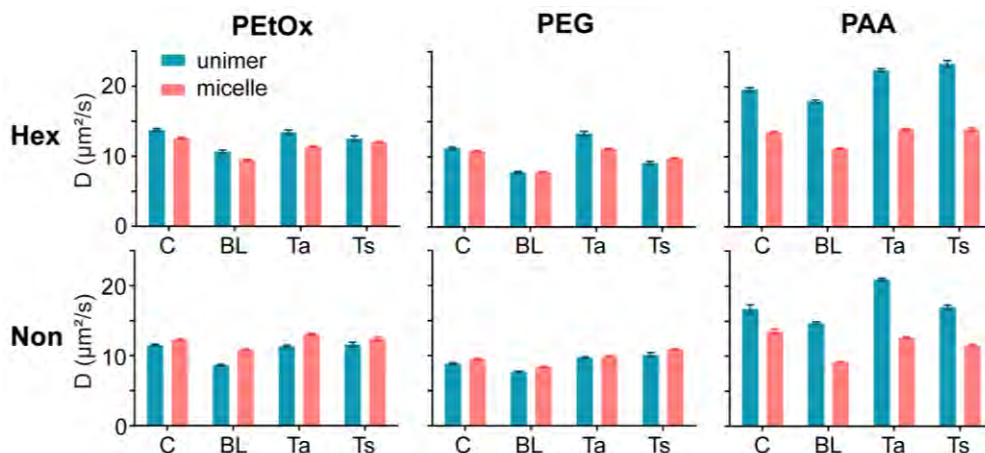
Figure 3.9. Diffusion constants. Unimers (blue) and micelles (red) diffusion constants were calculated from FRAP measurements in different locations inside the chip. Control measurements ("C") were performed in solution, on a glass slide. "BL", "Ta", "Ts" represent basal lamina, tumor ECM away from spheroids and tumor ECM next to spheroids respectively.
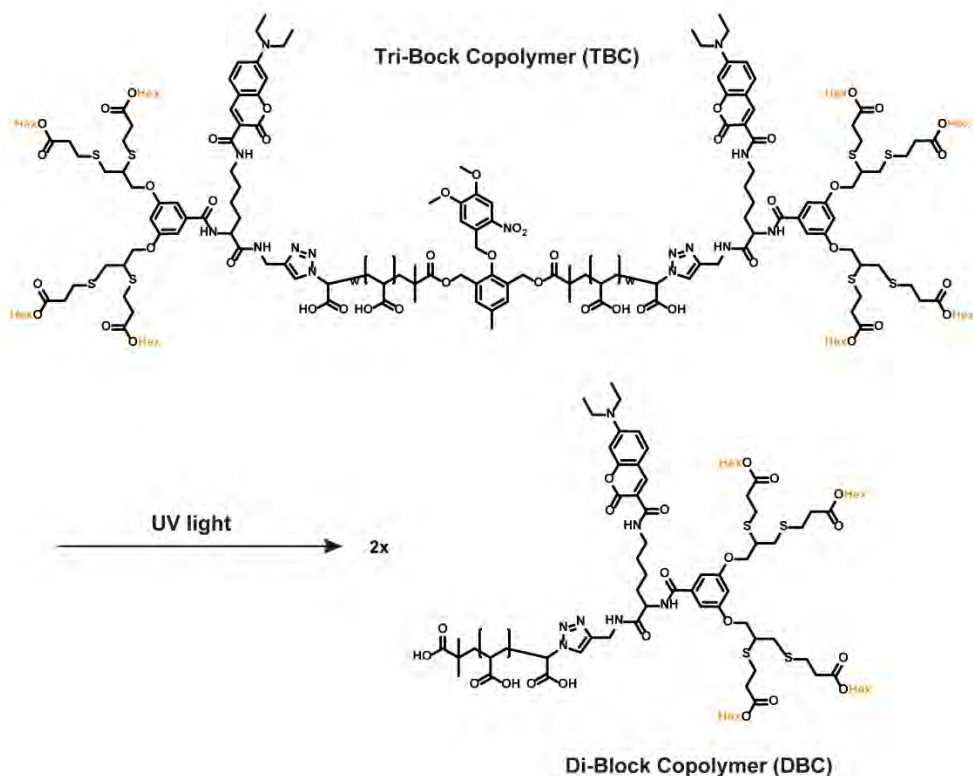
More stable PAA formulations

An important part of the nanocarrier design process is the feedback loop between formulation and testing. The faster the feedback, the easier it is to understand the effects of different parameters and to improve the DDS design.

In this section, we will use the information obtained from the previous measurements to improve the design of our micelles in terms of their ECM interactions. In the previous section, PAA polymers were the ones showing the greatest internalization capacity into MCF7 spheroids, which would make them the most promising polymers for drug delivery. However, PAA polymers interacted more with the basal lamina fibers, which could be due to their low stability in biological media. Thus, we decided to move forward to a more stable design of PAA polymers.

One challenging aspect in designing enzyme-responsive polymeric micelles is that increasing the micelle stability (for instance by using a larger hydrophobic end) leads to decreased enzyme responsiveness.[27] A way to overcome this limitation is by using hydrophobic-hydrophilic-hydrophobic (B-A-B) tri-block copolymer (TBC) design. In this approach, the enzyme-responsive groups can be unlocked on-demand through

an external trigger. The trigger will cut a covalent bond in the middle of the polymer, resulting in two identical di-block copolymers (DBC). While the cleavage into DBC does not affect directly the micelle structure, it causes the enzyme-labile groups to be exposed, thus increasing the sensitivity of the amphiphiles to protein interaction and enzymatic degradation. Consequently, the unimer:micelle equilibrium is affected, increasing the amount of unimers in solution.

Figure 3.10. More stable amphiphile formulations containing PAA as hydrophilic polymer. Tri-block copolymer consists of two PAA-Hex with the hydrophilic ends connected by a UV-cleavable moiety. Upon exposure to UV light, the molecule cleaves forming two di-block copolymers.

In our case, we used as a responsive trigger a UV-cleavable group in the middle of a PAA polymer. This formulation basically contains the equivalent of two previous PAA-Hex copolymers, in the form of "Hex-PAA-Hex", where the PAA contains in the middle the UV-cleavable group (Figure 3.10). This creates a responsive material, designed to trigger the disassembly locally and in a controlled manner. After self-assembly in aqueous environment, the resulting micelles are partially crosslinked and

easily cleavable by UV irradiation to create di-block copolymers (DBC), which are equivalent to PAA-Hex.

We tested the TBC and DBC micelles in the chip multigel model, in the same conditions as previous micelles. In the basal lamina compartment, total fluorescence images showed that both TBC and DBC accumulate onto ECM formations. Interestingly, unlike the previous PAA-Hex, the ratiometric images revealed that TBC were binding more in the form of micelles than unimers. This was not observed for the UV-cleaved DBC, where the ratio was similar to the one in solution (Figure 3.11A,B), which recapitulates the previous PAA-Hex results.
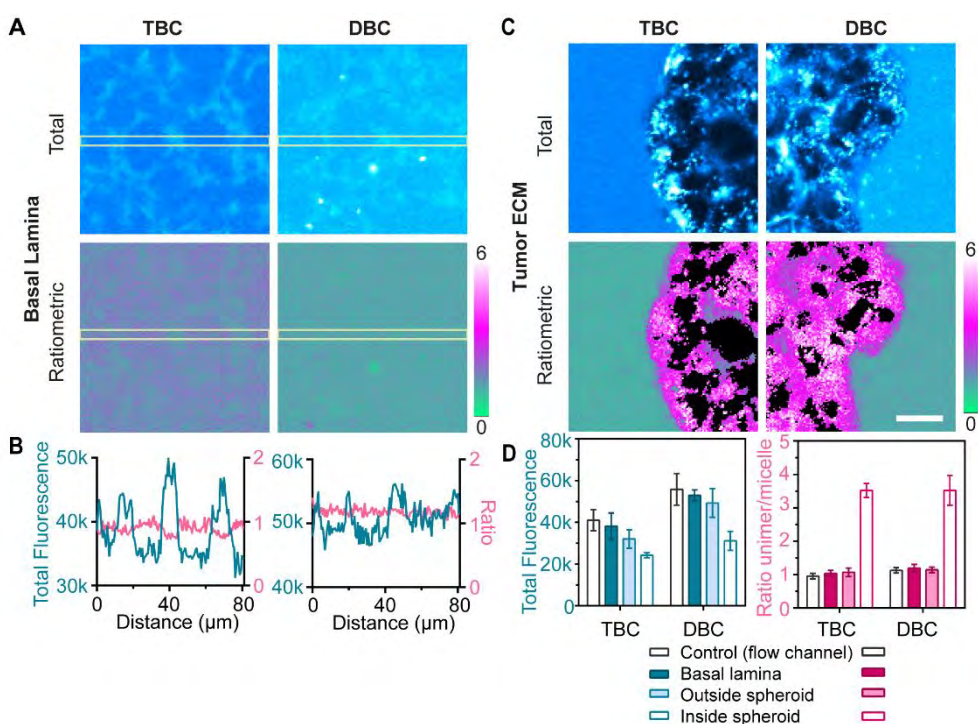
Figure 3.11. Total fluorescence and ratiometric images of more stable amphiphilic formulations inside the dual-ECM chip setup. Tri-block copolymers and the corresponding di-block copolymers are shown in the basal lamina (A), with plotted profiles of rectangular regions 5x20 µm (B) and at the edge of a spheroid in the "tumor ECM" side-channel after 24h incubation (C). Fluorescence intensity mean in different chip locations is shown as bar plot (D).

In the "tumor ECM" chip compartment, we observed a similar behavior to PAA-Hex. There is no observable interaction to the collagen-HA matrix, while internalization

into MCF7 spheroids was relatively high. Inside spheroids the mean unimer:micelle ratio was above 3 for both TBC and DBC (Figure 8C,D), meaning that even the more stable TBC are being disassembled by the cells. When looking at the mean ratio in the other chip compartments, TBC has a ratio of 1, which is something we would expect considering its higher stability. However, there is only a slight increase in the mean unimer:micelle ratio from TBC to DBC. Subsequently, DBC appear more stable than the previous PAA-Hex. Notably, the cleavage from tri-block to di-block compolymers does not affect directly the micelle assembly, but indirectly, by allowing the micelles to dissassemble due to changes in the solution equilibrium or from interactions with proteins.

Next, we performed FRAP measurements to check the dynamics of TBC and DBC inside different chip compartments. In this case, for DBC we observed complete recovey in all locations, which is consistent with previous results of PAA polymers. However, the TBC had lower recovery in basal lamina and close to spheroids, shown by a lower plateau value, indicating the presence of an immobile fraction. Also, the diffusion rate was slightly slower in basal lamina (Figure 3.12).
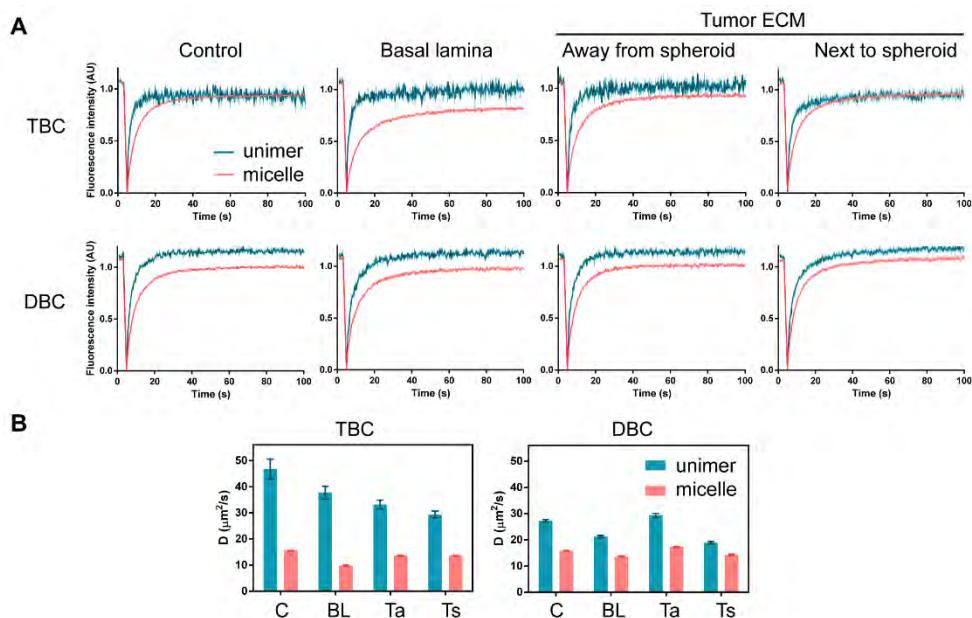
Figure 3.12. Fluorescence recovery after photobleaching of tri-block and di-block copolymers. (A) Fluorescence recovery curves of the first 100s (from the 4 minutes measured), including 10 pre-bleach frames. Curves are shown as mean + SEM of at least 3 measurements per condition, in each compartment of the chip. (B)

Diffusion constants of unimers (blue) or micelles (red) calculated from the FRAP data are shown as bar plot in each compartment of the chip. "C", "BL", "Ta", "Ts" represent control in solution (outside the chip), basal lamina, tumor ECM away from spheroids and tumor ECM next to spheroids respectively.

A possible explanation would be that TBC micelles being crosslinked, the exchange of amphiphiles between micelle form and solution is blocked. Thus, bound micelles in the bleach region will remain dark, while for DBC the bound micelles can still exchange amphiphiles with the solution, regaining their fluorescence. Overall, the TBC predominance of micelles over unimers onto basal lamina mesh and the lower fluorescence recovery are bringing to light a plausible mechanism of mobility accross the attractive forces of ECM: through the fast exchange of unimers between solution and formed micelles.

CONCLUSIONS

In summary, the current chapter presents a simple tumor-on-a-chip model to mimic the tumor tissue barrier, consisting of two types of ECM (reconstituted basal lamina and collagen type I – hyaluronic acid mix) and MCF7 spheroids.

Inside this 3D chip model we tested the distribution and mobility of polymeric micelles, comparing three hydrophilic shells: poly(ethylene glycol), poly(2-ethyl-2-oxazoline), and poly(acrylic acid), combined with two lengths of the dendritic hydrophobic ends (Hexyl or Nonyl). We observed different interaction behaviors inside the basal lamina, correlated with micelle stability: avoidance of basal lamina mesh for the more stable PEtOx-Non and PEG-Non and reversible binding for negatively charged PAA formulations. Spheroid uptake, on the contrary, was best for PAA formulations.

Attempting a more stable PAA design, we tested a responsive UV-cleavable tri-block copolymer micelle. In this case we observed basal lamina binding in predominant micelle form, with slightly decreased mobility, while cellular uptake in a predominant unimer form remained high. This points to the exchange of unimers between solution and formed micelles as an important mechanism for passage through ECM.

Overall, the chapter emphasizes the importance of testing both cellular uptake and delivery through ECM and showcases the use of a simple microfluidic chip for

increasing the understanding of tumor drug delivery systems in a much shorter and efficient feedback loop between formulation and testing.

MATERIALS & METHODS

Chip preparation

The commercial microfluidic chip DAX-1 (AIM Biotech) was filled in the middle channel with ECM from Engelbreth-Holm-Swarm murine sarcoma cells (Sigma Aldrich), 2x diluted in full DMEM (10% FBS, from Thermo Fisher) to a final protein concentration of 5.25 mg/mL. The ECM was allowed to gelate for 15-20 min at 37° C, 5% CO_2, placed on two PDMS supports of 4 mm thickness, one at each end of the chip, inside a Parafilm-sealed Petri Dish. After ECM gelation, the right side channel was filled with collagen-hyaluronic acid mix containing MCF7 spheroids. The mix preparation was adapted from AIM Biotech general protocol v.5.3. Collagen gel was prepared at a final concentration of 2.5 mg/mL gelated inside the chip at pH 7.4 and 37° C, conditions which mimmick tumor environment[18]. Briefly, collagen type I from rat tail acid solution (Corning) was brought to pH 7.4 on ice by pre-mixing with Phenol Red and PBS 10x (both from Sigma Aldrich) as 10% of final volume, then adding sodium hydroxyde 0.5 N (PanReac NaOH pellets dissolved in MilliQ water) until the color changed to faint pink. Hyaluronic acid sodium salt from rooster comb (Sigma Aldrich) dissolved in MilliQ water was added to a final concentration of 0.8 mg/mL. The gel mix was used to resuspend pre-made MCF7 spheroids after 5 min centrifugation at 200 g. MCF7 spheroids were obtained by seeding 1000 cells/well in a 96-well low-attachment NUNC Sphera plate, 48h prior to chip preparation. The right side-channel of the chip was filled with the final mix, then the chip was incubated at 37° C, 5% CO_2 for 30 min using the same Parafilm-sealed Petri Dish setup. After gelation, the left side channel was filled with micelle solution of 160 µM, diluted 3x in full DMEM (from 480µM in PBS, pH 7.4). Micelle solution was then added to the reservoirs on the left side of the chip and allowed to diffuse inside the chip overnight at 37° C, 5% CO_2.

Cell culture reagents

MCF7 cells were cultured in full DMEM medium (Dulbecco's modified Eagle Medium 1x with added 4.5 g/L D-glucose, L-glutamine and pyruvate, from Thermo Fisher), supplemented with 10% fetal bovine serum, heat inactivated (Gibco, Thermo

Fisher) and 1% pennicillin/streptomycin (Biowest). Trypsin 25% EDTA (Thermo Fisher) was used for cell detachment.

Gel labeling

ECM from Engelbreth-Holm-Swarm murine sarcoma cells, 2x diluted in full DMEM (10% FBS) to 5.25 mg protein/mL was mixed with Cyanine3 NHS ester (Lumiprobe, dissolved in DMSO) to a final dye concentration of 19 µM and allowed to react for 1h on ice. Then, the reaction mix was added inside the chip middle channel and allowed to gelate for 15 min at 37° C, 5% CO_2 in a Parafilm sealed Petri Dish. Rat tail collagen type I (at final concentration 2.5 mg/mL and pH 7.4) and hyaluronic acid (0.8 mg/mL) mix was reacted with 10 µM Cyanine5 NHS ester (Lumiprobe, dissolved in DMSO) for 45 min on ice, then added to the right side channel of the chip after the gelation of the middle channel. The collagen-HA mix was allowed to gelate for 30 min at 37° C, 5% CO_2. The remaining side-channel of the chip was filled with PBS (pH 7.4) and the chip was imaged immediately in Zeiss LSM 800 confocal microscope, using 561 nm and 640 nm excitation for Cy3 and Cy5 channels respectively.

Live/dead assay

A chip was prepared containing MCF7 spheroids and allowed to grow for 24h in full DMEM. Using only the flow channel, the chip was first washed with serum-free DMEM, which was then used for all further steps. Then, calcein AM (Sigma Aldrich) solution 10 µM in serum-free DMEM was added to the left side channel of the chip and allowed to distribute inside the chip for 1h at at 37° C, 5% CO_2. Then, the solution was replaced by propidium iodide in serum-free DMEM, for 10 min. A final wash was performed, leaving the chip with serum-free DMEM during imaging in confocal microscope.

Micelle characterization (Zeta potential and DLS)

Micelle solution of 80 µM in PBS (pH 7.4) was measured in triplicate using Malvern Zetasizer Nano ZS for determining the ζ-potential in plastic cuvettes and using dynamic light scattering with low-volume quartz cuvettes for determining the size.

Micelle cytotoxicity

MCF7 cells were seeded in a flat-bottom transparent 96-well plate (Nunc, Thermo Scientific) as 5000 cells/well and allowed to grow for 24h. The supernatant was replaced by 160µM micelle solution in full DMEM (10% FBS). PBS (pH 7.4) or Triton X-100 0.01% v/v in full DMEM were used as negative or positive controls respectively. After 24h, the cells were incubated for 1h with Presto Blue solution (ThermoFisher) as 10% v/v, at 37° C, 5% CO_2 . Florescence was measured using a multimode microplate reader (Infinite M200 Pro, Tecan), with 550 nm excitation, acquiring the signal at well bottom at 600 nm emission. Samples were prepared in triplicate, in randomized order.

Confocal microscopy

Imaging was performed on a Zeiss LSM 800 confocal laser scanning microscope equipped with AxioCam 503c camera (2.8 Mega pixels) and two PTM Multi Alkali detectors, using the Zen 2.3 (blue) software. Images were aquired with a plan apochromat 20x / 0.8 M27 objective and using 37° C, CO_2/O_2 incubation. A diode laser 405 nm (5 mW) at 1% power was used for excitation, while the emission was collected in two different channels: 400-500 nm for unimers and 500-700 nm for micelle fluorescence respectively. The two channels were summed in Fiji ImageJ[28] to obtain the "total fluorescence" images; the unimer signal was divided by the micelle signal after background removal to obtain "ratiometric" images.

FRAP

Fluorescence Recovery After Photobleaching was performed in the same LSM 800 confocal microscope using the 20x objective and the dual channel aquisition. A circular region of 35.3 µm in diameter was used for bleaching, in the center of a 103x103 µm image (zoom 3.1x, 256x256 pixels, 16 bit, unidirectional). A total of 4 minutes experimental time were recorded with 102.4 ms/frame and 405 nm excitation at 1%, including 10 frames pre-bleach and the bleaching time of 3,14 sec localized as 10 iterations with 100% laser power inside the bleach area. An overview image of the area (638.9 µm square, zoom 0.5x) was captured before each FRAP measurement. For control measurements, the same micelle solution in full DMEM at 160 µM was added onto a glass slide with two layers of double-sided sticky tape and coverslip on top, then sealed with nail polish to prevent drying. All FRAP measurements were performed with 37° C and CO_2/O_2 incubation.

Post-processing of FRAP data was done using Fiji ImageJ[28] and easyFRAP[29,30]. The fluorescence inside the bleach area was measured unsing a smaller circle (30 µm in diameter) to avoid measuring any subtle drift. A double normalization of the recovery data was performed with the online easyFRAP tool, correcting for photobleaching during acquisition by using the mean fluorescence of the whole image. Also, we used the assumption that the first post-bleach value in the bleach region is the "background" value. Then, one-component exponential curve fitting was performed in GraphPad Prism (GraphPad Software, San Diego, California, USA), on the normalized data of all repeated measurements, with "Y_0" constrained to "0", after removing the pre-bleach values. Taking the half-time obtained in the fitting, we calculated the diffusion constants using the simplified equation of Soumpasis et al.[31], which assumes instantaneous bleach: $D = 0.224 \cdot r_n^2 / \tau_{1/2}$, where r_n is the nominal radius of the bleach area and $\tau_{1/2}$ is the half-time of fluorescence recovery, while 0.224 is a coefficient numerically determined for aqueous environment.

REFERENCES

(1) Gao, J.; Karp, J. M.; Langer, R.; Joshi, N. The Future of Drug Delivery. *Chem. Mater.* **2023**, *35* (2), 359–363. https://doi.org/10.1021/acs.chemmater.2c03003.

(2) Pozzi, S.; Scomparin, A.; Israeli Dangoor, S.; Rodriguez Ajamil, D.; Ofek, P.; Neufeld, L.; Krivitsky, A.; Vaskovich-Koubi, D.; Kleiner, R.; Dey, P.; Koshrovski-Michael, S.; Reisman, N.; Satchi-Fainaro, R. Meet Me Halfway: Are in Vitro 3D Cancer Models on the Way to Replace in Vivo Models for Nanomedicine Development? *Advanced Drug Delivery Reviews* **2021**, *175*, 113760. https://doi.org/10.1016/j.addr.2021.04.001.

(3) Nichols, J. W.; Bae, Y. H. Odyssey of a Cancer Nanoparticle: From Injection Site to Site of Action. *Nano Today* **2012**, *7* (6), 606–618. https://doi.org/10.1016/j.nantod.2012.10.010.

(4) *New Nanomaterials and Techniques for Tumor-Targeted Systems*; Huang, R., Wang, Y., Eds.; Springer Singapore: Singapore, 2020. https://doi.org/10.1007/978-981-15-5159-8.

(5) Witten, J.; Ribbeck, K. The Particle in the Spider's Web: Transport through Biological Hydrogels. *Nanoscale* **2017**, *9* (24), 8080–8095. https://doi.org/10.1039/C6NR09736G.

(6) Lieleg, O.; Baumgärtel, R. M.; Bausch, A. R. Selective Filtering of Particles by the Extracellular Matrix: An Electrostatic Bandpass. *Biophysical Journal* **2009**, *97* (6), 1569–1577. https://doi.org/10.1016/j.bpj.2009.07.009.

(7) Hansing, J.; Duke, J. R.; Fryman, E. B.; DeRouchey, J. E.; Netz, R. R. Particle Diffusion in Polymeric Hydrogels with Mixed Attractive and Repulsive Interactions. *Nano Lett.* **2018**, *18* (8), 5248–5256. https://doi.org/10.1021/acs.nanolett.8b02218.

(8) Cabral, H.; Matsumoto, Y.; Mizuno, K.; Chen, Q.; Murakami, M.; Kimura, M.; Terada, Y.; Kano, M. R.; Miyazono, K.; Uesaka, M.; Nishiyama, N.; Kataoka, K. Accumulation of Sub-100 Nm Polymeric Micelles in Poorly Permeable Tumours Depends on Size. *Nature Nanotech* **2011**, *6* (12), 815–823. https://doi.org/10.1038/nnano.2011.166.

(9) Lu, P.; Weaver, V. M.; Werb, Z. The Extracellular Matrix: A Dynamic Niche in Cancer Progression. *Journal of Cell Biology* **2012**, *196* (4), 395–406. https://doi.org/10.1083/jcb.201102147.

(10) Travascio, F.; Arends, F.; Lieleg, O. *Composition and Function of the Extracellular Matrix in the Human Body*; IntechOpen, 2016. https://doi.org/10.5772/61601.

(11) Foster, D. S.; Jones, R. E.; Ransom, R. C.; Longaker, M. T.; Norton, J. A. The Evolving Relationship of Wound Healing and Tumor Stroma. *JCI Insight 3* (18), e99911. https://doi.org/10.1172/jci.insight.99911.

(12) Schwertfeger, K. L.; Cowman, M. K.; Telmer, P. G.; Turley, E. A.; McCarthy, J. B. Hyaluronan, Inflammation, and Breast Cancer Progression. *Front. Immunol.* **2015**, *6*. https://doi.org/10.3389/fimmu.2015.00236.

(13) Liu, M.; Tolg, C.; Turley, E. Dissecting the Dual Nature of Hyaluronan in the Tumor Microenvironment. *Front Immunol* **2019**, *10*. https://doi.org/10.3389/fimmu.2019.00947.

(14) Whatcott, C. J.; Han, H.; Posner, R. G.; Hostetter, G.; Von Hoff, D. D. Targeting the Tumor Microenvironment in Cancer: Why Hyaluronidase Deserves a Second Look. *Cancer Discovery* **2011**, *1* (4), 291–296. https://doi.org/10.1158/2159-8290.CD-11-0136.

(15) Kleinman, H. K.; McGarvey, M. L.; Hassell, J. R.; Star, V. L.; Cannon, F. B.; Laurie, G. W.; Martin, G. R. Basement Membrane Complexes with Biological Activity. *Biochemistry* **1986**, *25* (2), 312–318. https://doi.org/10.1021/bi00350a005.

(16) Kleinman, H. K.; Martin, G. R. Matrigel: Basement Membrane Matrix with Biological Activity. *Seminars in Cancer Biology* **2005**, *15* (5), 378–386. https://doi.org/10.1016/j.semcancer.2005.05.004.

(17) Feiner-Gracia, N.; Glinkowska Mares, A.; Buzhor, M.; Rodriguez-Trujillo, R.; Samitier Marti, J.; Amir, R. J.; Pujals, S.; Albertazzi, L. Real-Time Ratiometric Imaging of Micelles Assembly State in a Microfluidic Cancer-on-a-Chip. *ACS Appl. Bio Mater.* **2021**, *4* (1), 669–681. https://doi.org/10.1021/acsabm.0c01209.

(18) Aref, A. R.; Huang, R. Y.-J.; Yu, W.; Chua, K.-N.; Sun, W.; Tu, T.-Y.; Bai, J.; Sim, W.-J.; Zervantonakis, I. K.; Thiery, J. P.; Kamm, R. D. Screening Therapeutic EMT Blocking Agents in a Three-Dimensional Microenvironment. *Integr Biol (Camb)* **2013**, *5* (2), 381–389. https://doi.org/10.1039/c2ib20209c.

(19) Slor, G.; Olea, A. R.; Pujals, S.; Tigrine, A.; De La Rosa, V. R.; Hoogenboom, R.; Albertazzi, L.; Amir, R. J. Judging Enzyme-Responsive Micelles by Their Covers: Direct Comparison of Dendritic Amphiphiles with Different Hydrophilic Blocks. *Biomacromolecules* **2021**, *22* (3), 1197–1210. https://doi.org/10.1021/acs.biomac.0c01708.

(20) Buzhor, M.; Harnoy, A. J.; Tirosh, E.; Barak, A.; Schwartz, T.; Amir, R. J. Supramolecular Translation of Enzymatically Triggered Disassembly of Micelles into Tunable Fluorescent Responses. *Chemistry – A European Journal* **2015**, *21* (44), 15633–15638. https://doi.org/10.1002/chem.201502988.

(21) Feiner-Gracia, N.; Buzhor, M.; Fuentes, E.; Pujals, S.; Amir, R. J.; Albertazzi, L. Micellar Stability in Biological Media Dictates Internalization in Living

Cells. *J. Am. Chem. Soc.* **2017**, *139* (46), 16677–16687. https://doi.org/10.1021/jacs.7b08351.

(22) Lieleg, O.; Baumgärtel, R. M.; Bausch, A. R. Selective Filtering of Particles by the Extracellular Matrix: An Electrostatic Bandpass. *Biophysical Journal* **2009**, *97* (6), 1569–1577. https://doi.org/10.1016/j.bpj.2009.07.009.

(23) Lee, B.; Konen, J.; Wilkinson, S.; Marcus, A. I.; Jiang, Y. Local Alignment Vectors Reveal Cancer Cell-Induced ECM Fiber Remodeling Dynamics. *Sci Rep* **2017**, *7*, 39498. https://doi.org/10.1038/srep39498.

(24) Kihara, T.; Ito, J.; Miyake, J. Measurement of Biomolecular Diffusion in Extracellular Matrix Condensed by Fibroblasts Using Fluorescence Correlation Spectroscopy. *PLoS One* **2013**, *8* (11). https://doi.org/10.1371/journal.pone.0082382.

(25) Pilz, M.; Kwapiszewska, K.; Kalwarczyk, T.; Bubak, G.; Nowis, D.; Hołyst, R. Transport of Nanoprobes in Multicellular Spheroids. *Nanoscale* **2020**, *12* (38), 19880–19887. https://doi.org/10.1039/D0NR01986K.

(26) Valente, K. P.; Suleman, A.; Brolo, A. G. Exploring Diffusion and Cellular Uptake: Charged Gold Nanoparticles in an in Vitro Breast Cancer Model. *ACS Appl. Bio Mater.* **2020**, *3* (10), 6992–7002. https://doi.org/10.1021/acsabm.0c00872.

(27) Slor, G.; Amir, R. J. Using High Molecular Precision to Study Enzymatically Induced Disassembly of Polymeric Nanocarriers: Direct Enzymatic Activation or Equilibrium-Based Degradation? *Macromolecules* **2021**, *54* (4), 1577–1588. https://doi.org/10.1021/acs.macromol.0c02263.

(28) Schindelin, J.; Arganda-Carreras, I.; Frise, E.; Kaynig, V.; Longair, M.; Pietzsch, T.; Preibisch, S.; Rueden, C.; Saalfeld, S.; Schmid, B.; Tinevez, J.-Y.; White, D. J.; Hartenstein, V.; Eliceiri, K.; Tomancak, P.; Cardona, A. Fiji: An Open-Source Platform for Biological-Image Analysis. *Nat Methods* **2012**, *9* (7), 676–682. https://doi.org/10.1038/nmeth.2019.

(29) Rapsomaniki, M. A.; Kotsantis, P.; Symeonidou, I.-E.; Giakoumakis, N.-N.; Taraviras, S.; Lygerou, Z. EasyFRAP: An Interactive, Easy-to-Use Tool for

Qualitative and Quantitative Analysis of FRAP Data. *Bioinformatics* **2012**, *28* (13), 1800–1801. https://doi.org/10.1093/bioinformatics/bts241.

(30) Koulouras, G.; Panagopoulos, A.; Rapsomaniki, M. A.; Giakoumakis, N. N.; Taraviras, S.; Lygerou, Z. EasyFRAP-Web: A Web-Based Tool for the Analysis of Fluorescence Recovery after Photobleaching Data. *Nucleic Acids Research* **2018**, *46* (W1), W467–W472. https://doi.org/10.1093/nar/gky508.

(31) Soumpasis, D. M. Theoretical Analysis of Fluorescence Photobleaching Recovery Experiments. *Biophys J* **1983**, *41* (1), 95–97.

Chapter 4. Imaging the dynamics and stability of single-chain polymeric nanoparticles in a multi-gel tumor-on-a-chip

This chapter represents preliminary data and reproduces almost literally parts of the article manuscript (*in the process of submission*):

Imaging dynamics and stability of single-chain polymeric nanoparticles in a multi-gel tumor-on-a-chip, Linlin Deng, Alis R. Olea, Silvia Pujals, Anja Palmans, Lorenzo Albertazzi (2023)

All cellular and chip experiments in this chapter were performed by myself. Particle synthesis and characterization was done by Linlin Deng.

INTRODUCTION

The concept of 'macromolecules' was postulated by Staudinger in 1922, leading after one century of research to the development of modern polymeric materials and their wide array of applications.[1] Nowadays, polymer chemists have a massive synthetic toolbox available for producing polymeric nanoparticles with specific size, shape and functionalization.[2–4] A relatively new class of synthetic nanocarriers are the single-chain polymeric nanoparticles (SCPNs) which have great potential in nanomedicine as bio-inspired nanostructures.[5–7] An individual polymeric chain is self-folding in aqueous environment into nano-sized SCPNs in the size range of many proteins (5–20 nm),[8] which is 10 times smaller than most polymeric nanoparticles. NPs size is one of the critical factors influencing the blood survival time, biodistribution, ECM penetration and cellular uptake.[9] For instance, smaller nanoparticles showed increased penetration into hypovascular tumors.[11]

Due to the small size of SCPNs and their design that allows easy tunability of different molecular moieties, an increasing body of research has been recently driven towards their biological applications. For instance, SCPNs have been designed for controlled drug delivery,[12,13] cellular imaging[14] and bioorthogonal catalysis.[15–17]

Self-folding in aqueous environment is driven by the hydrophobic, hydrophilic and supramolecular interactions of the polymers comprising the SCPNs structure and leads to the formation of a hydrophobic pocket.[18,19] Many types of hydrophobic molecules can thus be encapsulated inside the SCPNs, including lipophilic drugs, fluorophores or catalysts. Although SCPNs research has shown great success up to date, the studies are mainly done in physiological buffers or in 2D cell cultures,[20–22] lacking the complexity of the *in vivo* environment.

Thus, in order to deepen the understanding of SCPNs interactions within a tumor environment, we can make use of *in vitro* 3D platforms. Several aspects would be interesting to assess in a 3D platform including SCPNs interaction with ECM and cellular uptake efficiency. During the passage through ECM and cellular internalization it is important to investigate the folding state of the SCPNs. SCPNs stability is very important for shielding the molecular cargo, such as in the case of an active catalyst, as well as to prevent drug release before the target location is reached. A great strategy for tracking SCPNs stability is through the use of responsive fluorophores covalently bound to the SCPN backbone. Such a fluorophore is Nile

Red, which changes the fluorescence emission spectra in response to local polarity,[23] being very suitable to probe the folding state of SCPNs.

In this chapter, we used a microfluidic chip containing two types of ECM and 3D cancer cells MCF7 spheroids (explained in detail in **chapter 3**) for comparing a set of Nile Red decorated SCPNs differing in hydrophobicity, supramolecular stacking, hydrophilic moiety, and surface charge. Fluorescence recovery after photobleaching (FRAP) was applied to assess their dynamics through ECM and spectral imaging of Nile Red as a reporter mechanism for SCPNs intramolecular hydrophobicity and folding state. We observed a set of stable SCPNs formulations in their passage through ECM, which displayed interesting differences both in spheroid uptake and conformational stability after being internalized by 3D cancer cells.

RESULTS & DISCUSSION

For comparing SCPNs formulations we used the fluorescent dye Nile Red, covalently attached to the SCPNs backbone. Nile Red signal is responsive to the hydrophobicity of its environment. A more hydrophobic environment causes a decrease in intensity and a spectral shift to the left. Inside SCPNs, Nile Red acts as a sensor for the folding state of the particle: in a folded SCPN, Nile Red localizes in the hydrophobic pocket of the SCPNs core, while inside a partially unfolded SCPN the hydrophobicity decreases significantly from the exposure of Nile Red to the outer environment, causing a spectral shift (Fig. 4.1A,B).

For a comparative study of SCPNs formulations it is important to assess both ECM penetration and cellular uptake in 3D. In this sense, we used the dual-ECM microfluidic chip model described in detail in **chapter 3** (Fig. 4.1C,D). In brief, the commercial microfluidic chip DAX1 from AIM Biotech consists of three channels separated by triangular pillars. The middle channel was filled with reconstituted basement membrane (5.25 mg protein/mL). The right side-channel was filled with a mix of collagen type I (gelated at 2.5 mg/mL, pH 7.4, 37° C), hyaluronic acid (0.8 mg/mL) and MCF7 spheroids of 100 µm in diameter on average. The left side-channel of the chip was used for adding SCPNs solution (3 mg/mL in full DMEM), which was allowed to diffuse overnight through the ECM-filled channels, without the use of a pump which could damage the integrity of the ECM gels.

ECM penetration and 3D spheroids uptake inside the chip were assessed in a confocal microscope setup for different SCPNs formulations. Fluorescence recovery after photobleaching (FRAP) was used to assess SCPNs dynamics in each chip compartment, while spectral imaging of Nile Red fluorescence was employed to reveal the local SCPNs folding state (Fig. 4.1E).
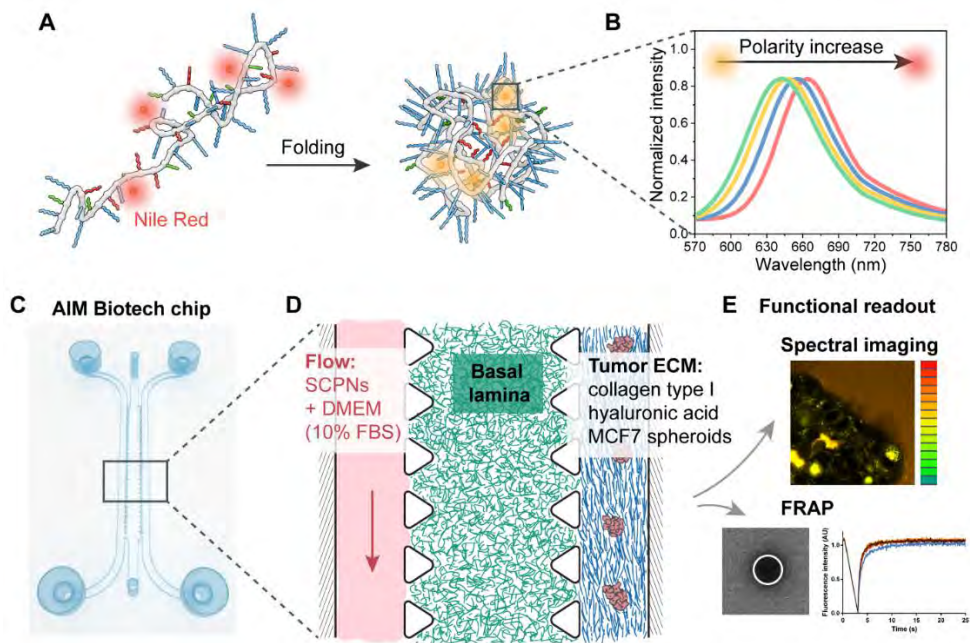
Figure 4.1. Experimental setup. SCPNs can self-fold in aqueous environment. Nile Red dye was covalently attached to SCPNs backbone, as a fluorescent reporter for SCPNs hydrophobicity and folding state (A, B). For testing SCPNs behavior in a 3D tumor environment we used the commercial microfluidic chip DAX1 from AIM Biotech (C), which contains three channels separated by triangular pillars. The middle channel was filled with reconstituted basal lamina ECM. The right side-channel was filled with a mix of collagen type I, hyaluronic acid and MCF7 spheroids, representing the tumor ECM. SCPNs solution in full DMEM (10% FBS) was added to the remaining side-channel (D). SCPNs behavior was assessed both as ECM penetration and spheroid uptake. As a functional readout, we used spectral imaging for assessing local SCPNs folding state and FRAP for evaluating the dynamics in different compartments of the chip (E).

SCPNs structure design

A small library of polymers microstructures was prepared with different hydrophobic, hydrophilic and charged groups (Fig. 4.2). The hydrophobic group is the trigger for SCPNs self-folding in aqueous environment and is responsible for the creation of the hydrophobic pocket. We used n-dodecylamine (dodecyl) or the supramolecular moieties benzene-1,3,5-tricarboxamide (BTA) to compare the effect of hydrophobic interactions of the dodecyl with the BTA supramolecular stacking via three-fold hydrogen bonding interactions. For comparability, the percentages of dodecyl and BTA were adjusted for their hydrophobicity, since BTA contains three aliphatic chains while dodecyl has only one.[28] Also, the same hydrophilic moiety jeffamine M-1000 (Jef) was used for the comparison of hydrophobic blocks, while maintaining the polymerization number to 200. Three polymers were prepared: 20% dodecyl, 78% jeffamine, 2% Nile Red (**Dod-Jef 200**); 7% BTA, 91% jeffamine, 2% Nile Red (**BTA-Jef 200**) and 5% BTA, 15% dodecyl, 77% Jeffamine, 3% Nile Red (**BTA-Dod-Jef 200**). The first two polymers **Dod-Jef 200** and **BTA-Jef 200** had equivalent hydrophobicity, while the composite **BTA-Dod-Jef 200** was more hydrophobic.

In a folded SCPN, the surface-located hydrophilic moiety can have a decisive effect on the environment interactions and cellular fate of SCPNs. We chose to compare the effect of three hydrophilic moieties: jeffamine M-1000, zwitterion 4-((3-aminopropyl)dimethylammonio)butane-1-sulfonate and D-(+)-Glucosamine. Both jeffamine and zwitterion are highly hydrophilic moieties which create a layer or trapped water molecules on the particle surface through hydrogen bonding and eectrostatic interactions, which contribute to an antifouling effect.[29] On the other hand, glucose is a molecule in high demand for cancer cells which binds to the overexpressed glucose receptors GLUTs on the cancer cell surface and can enhance the particle uptake.[30] For comparison, we used 20% dodecyl as hydrophobic group, 78% hydrophilic group and 2% Nile Red. In this case, a lower polymerization number was used (100) due to aggregation issues for bigger polymers, thus obtaining other three polymers: **Dod-Jef 100**, **Dod-Zwit 100** and **Dod-Glc 100**. Notably, we were able to address a size comparison between **Dod-Jef 100** and **Dod-Jef 200**.

Surface charge was shown to be of critical importance for the passage of nanoparticles through ECM, for cellular uptake and the intracellular fate. To study how the surface charge affects SCPNs passage through ECM and 3D cellular interactions, we prepared positively charged SCPNs containing (3-aminopropyl)triphenylphosphonium (TPP) and negatively charged SCPNs with a

carboxylic acid (COOH) group. In order to ensure sufficient water solubility and surface charge, polymers were prepared containing 50% charged polymer, 48% jeffamine and 2% Nile Red: **TPP+-Jef 200**, **COO--Jef 200** and **COO--Jef 100**. The latter was added to aid in assessing the effect of different polymer sizes between polymers with different degree of polymerization. Importantly, all polymers maintain their self-folding capacity when dissolving in aqueous environment due to the random distribution of hydrophilic, hydrophobic and charged groups.
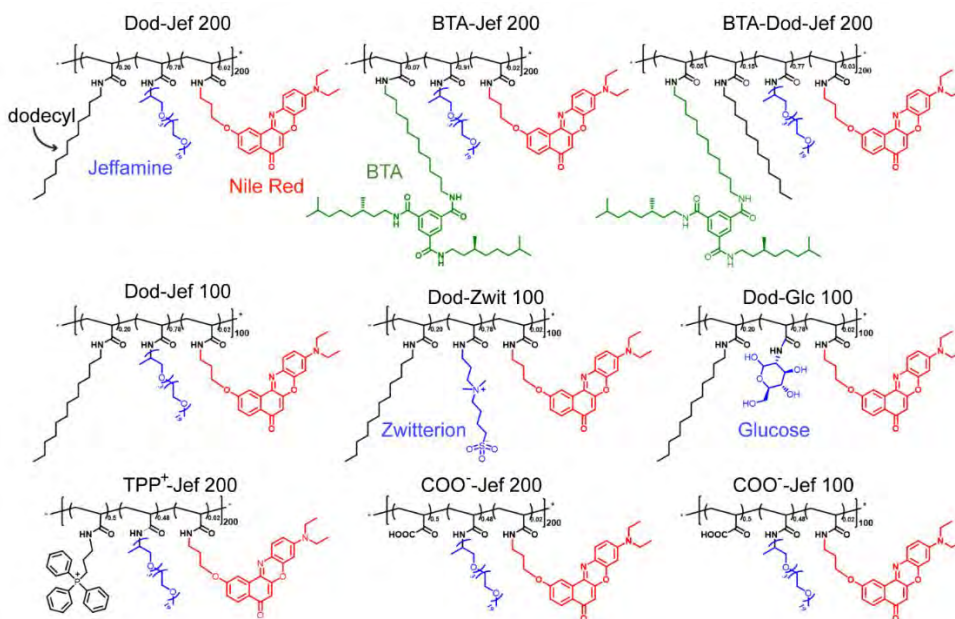

Figure 4.2. Chemical structures of SCPNs amphiphilic polymers. Polymers contained Nile Red and different hydrophobic, hydrophilic and charged groups. As hydrophobic groups, polymers were compared containing dodecyl (Dod-Jef 200), BTA (BTA-Jef 200) or both (BTA-Dod-Jef 200). As hydrophilic group, polymers with jeffamine (Dod-Jef 100), zwitterion (Dod-Zwit 100) and glucose (Dod-Glc 100) were compared. Charged polymers with a fixed hydrophilic jeffamine differed in charge, with pozitively charged TPP (TPP+-Jef 200) and negatively charged carboxylic acid (COO--Jef 200 and COO--Jef 100), with degree of polymerization 100 or 200.

For the purpose of the current chapter, we mention that folded SCPNs had sizes between 2-10 nm in hydrodynamic radius measured by DLS. In Zeta potential measurements performed in water, charged polymers showed surface charges of +31.3 mV and -29.4 mV for TPP+-Jef and COO--Jef respectively.

SCPNs penetration and mobility inside ECM

The advantage of having two types of ECM inside the chip is to be able to assess SCPNs penetration, interaction and mobility within each ECM gel in the presence of tumor spheroids. First, we assessed visually the penetration through each gel type after 24h incubation inside the chip. The SCPNs distributed freely inside both basal lamina and collagen-HA mix, indicating a high stability of the chosen polymer library and minimal interactions with ECM structures. Observable darker regions were present in the basal lamina in the case of larger polymers (DP 200), representing the structure of basal lamina mesh (Fig. 3A). For smaller polymers this was not visible probably due to the size difference. A few aggregates could be seen for **Dod-Glc 100**, however their presence throughout the chip indicates that aggregation happened in solution rather than through ECM interactions.
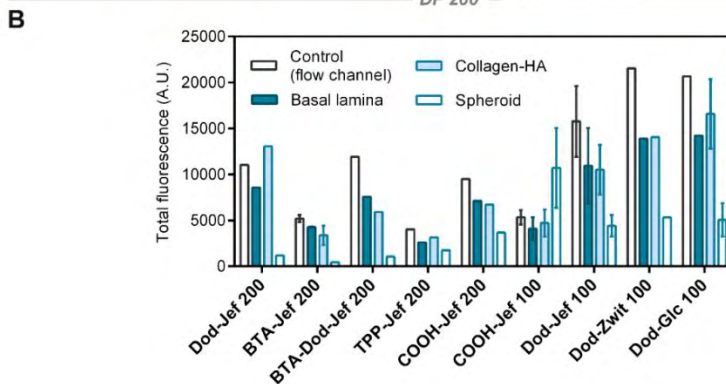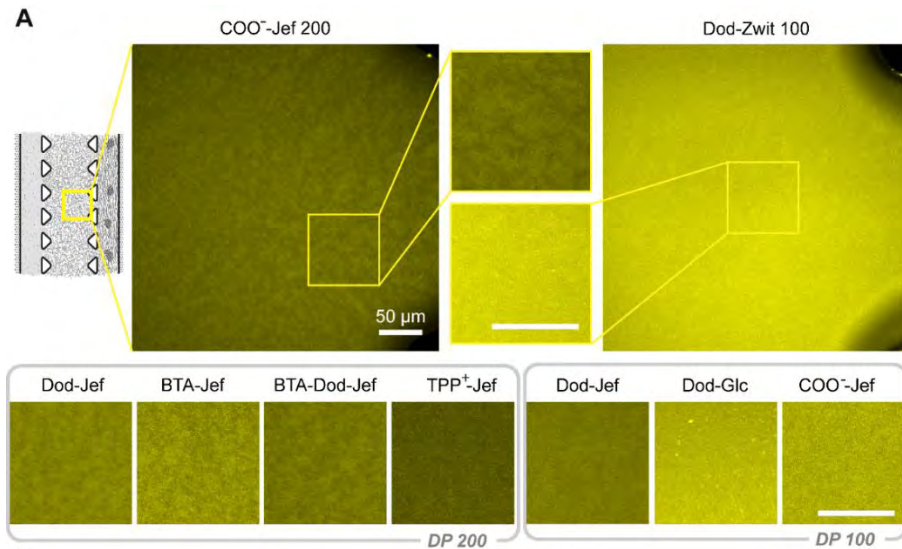
Figure 4.3. SCPNs penetration through ECM. (A) Overview and zoom confocal images of SCPNs formulations (labeled with Nile Red) at 1.5 mg/mL inside the middle channel of the chip, containing basal lamina reconstituted gel. Scale bars represent 50 μm. "DP" represents degree of polymeryzation, of either 100 or 200 for different polymers. Contrasts for BTA-Jef, TPP-Jef and COOH-Jef 100 were enhanced separately. (B) Quantification of the mean fluorescence signal in different compartments of the chip.

Unlike the PAA micelles discussed in **chapter 3**, which showed an attraction to the basal lamina mesh, in this case the SCPNs were avoiding basal lamina, a behavior similar to the highly stable PEtOx-Non and PEG-Non micelles.

For a more thorough comparison, we quantified the mean fluorescence intensity in different compartments of the chip (Fig. 4.3B). Generally, the fluorescent signal decreased from solution (flow channel) to basal lamina and collagen-HA gel, which is due to the increasing density of gel fibers compared to solution. Also, the quantification is indicative of the lack of interactions of the polymer library with either ECM model.

Further investigation on SCPNs mobility inside each ECM compartment was done using FRAP. The recovery of fluorescence after photobleaching can indicate whether SCPNs are binding to ECM, whether this possible binding is stable (in the case of an incomplete recovery which indicates an immobile fraction) and whether the ECM strcture causes diffusion hindrance. Generally, the observed recovery of fluorescence was complete for all polymers (Fig. 4.4), indicating the lack of an immobile fraction, with the exeption of a very small decrease in plateau value for **Dod-Zwit 100** and **Dod-Glc 100** which may be due to the presence of a few aggregates trapped in the gel pores.

Furthermore, the diffusion coefficient can be calculated from the FRAP recovery curves. All SCPNs had a fast diffusion in solution, with some small differences over DP. Calculated diffusion coefficients in solution were in the range of 25-35 $\mu m^2/s$ and 40-50 $\mu m^2/s$ for polymers with DP 200 and DP 100 respectively. The variability in diffusion rate suggests an impact of polymer microstructure on diffusion. Specifically, polymers containing BTA (**BTA-Jef 200** and **BTA-Dod-Jef 200**) had somewhat slower diffusion than dodecyl-based polymers (**Dod-Jef 200**). BTA supramolecular stacking inside the SCPNs causes an elongated pearl-necklace type

conformation,[31] which in turn increases the surface to volume ratio and the number of water molecules attached to the polymer surface.

Interestingly, polymers have shown a lower diffusion constant in the basal lamina gel irrespective of polymer composition. This is probably due to the microarchitecture of basal lamina as a reticular mesh, as well as smaller pore sizes, compared to collagen I which is arranged in a more loosely spaced fibrillar manner.[32] The FRAP bleach
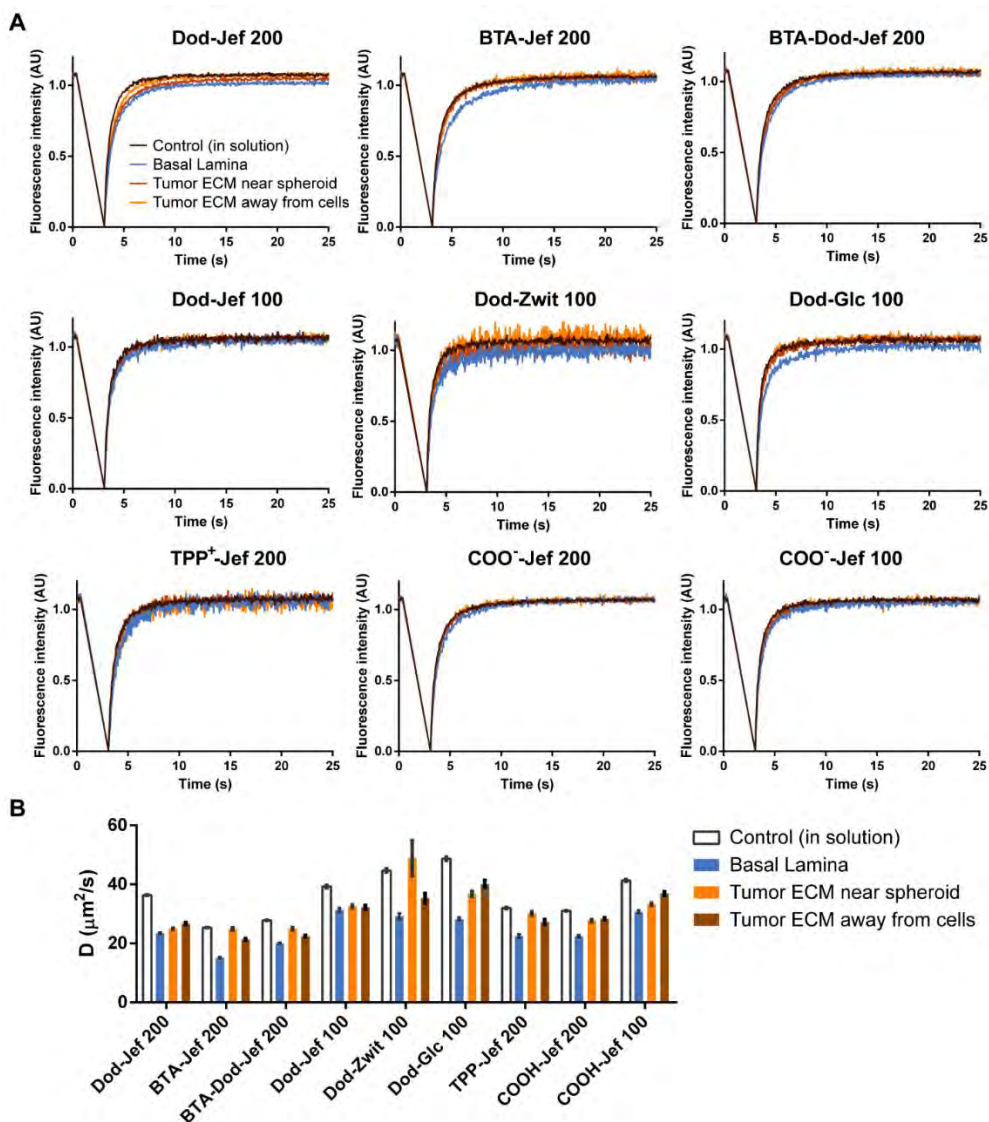
Figure 4.4. FRAP recovery curves (A) and calculated diffusion constants (B) of SCPNs in different regions inside the chip: in basal lamina, in tumor ECM next to spheroid or away from spheroid and control measurements in solution (outside chip).

area is large enough to contain several basal lamina pores, thus adding geometric confinement as a diffusion limiting factor.

In an attempt to assess the effect of MCF7 cells onto ECM filtering capabilities, we performed FRAP measurements in the collagen-HA side-channel both next to and away from spheroids. However, as discussed in **chapter 3**, our model might be too simplistic to identify such differences. In some cases it appears that SCPNs can move slightly slower near a spheroid (**Dod-Glc 100** or **COO⁻-Jef 100**) or faster (**Dod-Zwit 100**). Further evaluations in more suitable models would be required in order to draw any solid conclusions in this sense.

3D cellular uptake

The small library of polymers microstructures was then evaluated for their ability to enter the MCF7 spheroids embedded in the "tumor ECM" (collagen type I and HA mix) in the chip side-channel, after 24h incubation. We observed very different behaviors of MCF7 uptake (Fig. 4.5).

Hydrophobic formulations (**Dod-Jef 200**, **BTA-Jef 200** and **BTA-Dod-Jef 200**) showed a generally low uptake in MCF7 spheroids. Among them, the **Dod-Jef 200** polymer seemed to enter slightly more than the ones containing BTA, suggesting that BTA supramolecular stacking is slightly detrimental to cellular uptake. Probably the stacking of BTA creates a more tightly packed structure, with higher stability, which is less accessible to cellular interactions.

In contrast, charged polymers behaved better, showing more intracellular signal. Both positively charged and negatively charged polymers (**TPP⁺-Jef 200** and **COO⁻-Jef 200** respectively) had a clear intracellular distribution throughout the spheroid, indicating that polymer surface charge plays a crucial role in directing cellular uptake.

Polymers with different hydrophilic moiety (**Dod-Jef 100**, **Dod-Zwit 100** and **Dod-Glc 100**) had a similar good uptake, with clear signal inside cell cytoplasm or intracellular vesicles.

A striking difference however was between polymers with different DP. Both **Dod-Jef** and **COO⁻-Jef** had a much higher uptake for DP 100 compared to DP 200. By far the highest intracellular signal of all polymers was for **COO⁻-Jef 100**. This indicates that smaller SCPNs are preferred over larger polymers.

Yet, this could be partly due to the increased molar concentration of the smaller polymers, as a result of maintaining a constant mass concentration (1.5 mg/mL) as a necessary step in comparing polymers of different DP. A direct comparison of the cellular uptake and the calculated molar concentrations of the polymers is added in Appendix (Supplem. fig. 4.1). Notably, the Nile Red intensity is firstly dependent on the fluorophore concentration and secondly is influenced by the hydrophobicity of the environment – intensity decreases in a less hydrophobic environemnt. For this reason, an exact comparison and rationalization of Nile Red intensity is difficult in our case. A more comprehensive comparison is needed in future experiments having a fixed molar concentration of polymers and Nile Red dye. [Such a comparison has already been performed at the time of writing the thesis and is included in the article *in submision*.]

SCPNs spectral imaging

After comparing SCPNs internalization into spheroids, we further assessed their stability inside spheroids using spectral imaging. SCPNs folding state can be evaluated through the spectral emission of covalently-bound Nile Red, which is sensitive to the local hydrophobicity. In a folded SCPN, Nile Red locates in a hydrophobic pocket, giving an emission spectra peak of ~630 nm. Through spectral imaging we obtained spatially defined Nile Red spectra inside each compartment of the chip: in flow channel (solution), in basal lamina, in collagen-HA "tumor ECM" and inside spheroids. To assess local variability, we measured the spectra within 10 small circles inside each compartment of interest, plotting the mean spectra +/- SD in Figure 4.5B.

Interestingly, the spectra obtained in solution (in flow channel), in basal lamina and in the "tumor ECM" were fully overlapping. This signifies that ECM interactions do not affect SCPNs folding in any way, polymers being very stable inside both ECM models.

When reaching the tumor cells, the spectra changed dramatically. Inside spheroids, Nile Red fluorescence showed a shift to the left, reflecting a more hydrophobic environment. In particular, the charged and more hydrophilic formulations had the most substantial spectral change, probably due to the localization of Nile Red into more hydrophobic compartments of the cell, together with the unfolding of the SCPNs structure (Fig. 4.5A,B).

Inside the spheroid, both negatively charged (**TPP$^+$-Jef 200**) and positively charged polymers (**COO$^-$-Jef**) showed a substantial blue-shift of the spectra, changing the peak from 655 to 630 nm. Furthermore, **COO$^-$-Jef** had a broad shoulder in the distribution among lower wavelengths (570-610 nm). We should consider that both charged polymers have no hydrophobic moiety. They are less structured in solution and more unstable in the contact with cellular components. During cellular uptake, the conformation probably opens causing Nile Red to interact with more hydrophobic biomolecules.

A similar broad distribution in the lower wavelengths, but to a lesser extent happened for **Dod-Jef 100**, **Dod-Zwit 100** and **Dod-Glc 100**. Among the hydrophilic polymers, **Dod-Zwit 100** had also a change in the peak from 640 to 630 nm and the largest "shoulder" distribution in lower wavelenths, followed closely by **Dod-Glc 100**. In this case, the peak had almost no change, being already close to 630 nm in solution as a result of the dodecyl content which confers stability.
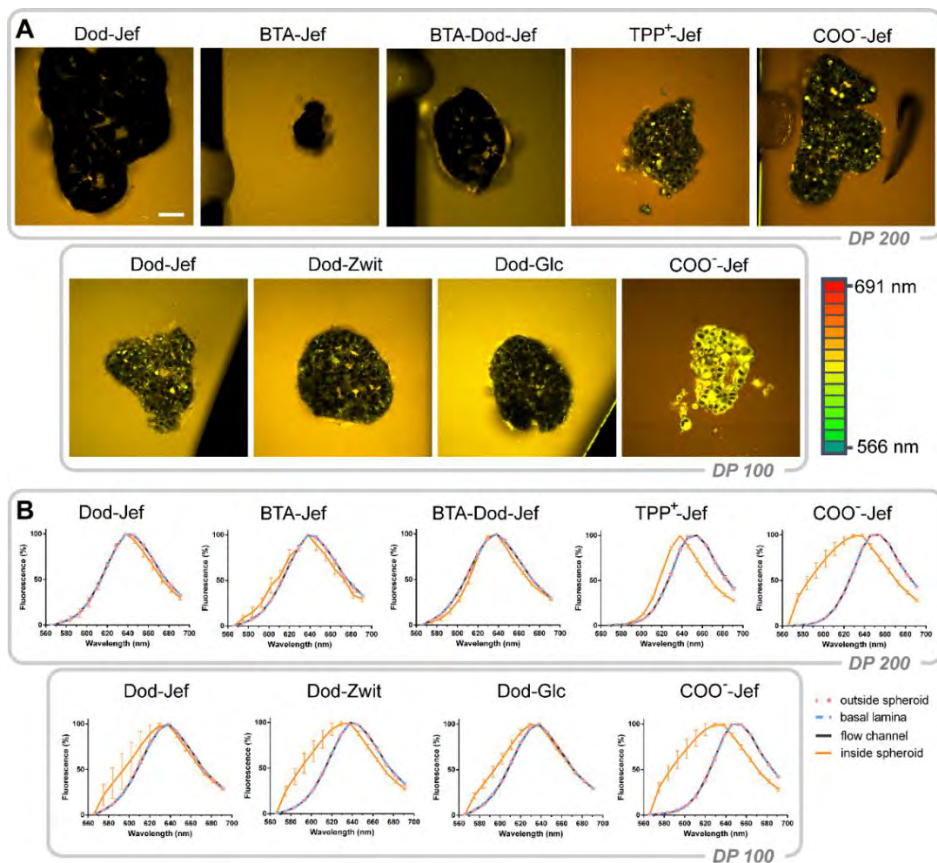
Fig. 4.5. Spectral imaging in tumor side-channel. (A) Spectral images of MCF7 spheroids incubated with Nile Red-containing SCPNs, excited with 561nm laser and having the emission split into a spectral acquisition consisting of 15 channels. Scale bar represents 50 µm. Contrast was adjusted individually for BTA-Jef and TPP-Jef. (B) Mean spectra of 10 separate circles in each region of the chip: outside spheroid, in basal lamina, in flow channel (overlapping curves) and inside spheroid.

Unlike the more hydrophilic polymers, the larger hydrophobic polymers (**Dod-Jef 200**, **BTA-Jef 200** and **BTA-Dod-Jef 200**) had no substantial change in emission spectra inside spheroids. We might attribute this however to the very little signal from low spheroid uptake.

When observing 3D spheroids an important and tricky task is to distinguish between intracellular and intercellular signal. For the more hydrophobic polymers (**Dod-Jef 200**, **BTA-Jef 200** and **BTA-Dod-Jef 200**), an interesting aspect was the appearance of bright structures within and around the spheroid, sometimes similar to a halo. These structures had a spectral profile similar to solution. What we might be seeing in this case is a partitioning of the polymers into the intercellular space where cells deposited ECM molecules.

Similarly, the advantage of combining spectral measurements with imaging is to be able to distinguish localized signal heterogeneities. Interestingly, for **Dod-Jef 100** and **Dod-Zwit 100** there were regions inside the spheroid with different spectra, shown in green and yellow in Figure 4A and presented as individual curves in Supplementary figure 4.2. By visually assessing the shape of these regions, we can approximate that the ones with a similar spectra to solution (more hydrophilic) are in fact intercellular, representing regions of ECM deposited by cells. Such intercellular spheroid ECM has been used recently as a model to study the penetration and diffusion of nanoparticles by Pilz et al. (2020)[33] and could be an interesting focus for future experiments.

CONCLUSIONS

In summary, we used a simple microfluidic chip containing dual ECM and MCF7 spheroids to assess the ECM penetration, mobility, cellular uptake and stablility of a small library of SCPNs. We compared two hydrophobic moieties with or without supramolecular stacking (BTA and dodecyl), three types of hydrophilic moieties

(jeffamine, zwitterion and glucose) and two charged groups (TPP^+ and COO^-) inside Nile Red-labeled SCPNs. All polymer formulations were able to pass ECM unhindered and maintaining the same spectra as in solution, indicating the increased stability of SCPNs folded structure. Important differences were observed in spheroid uptake, where more hydrophobic polymers had very little uptake, while the more hydrophilic and especially the charged polymers had high uptake. Interestingly, charged polymers had a substantial spectral shift inside cells indicating an open conformation. In contrast, the bigger and more hydrophobic formulations maintained the same folded structure inside spheroids. Overall, these results are an important proof-of-concept that a simple tumor-on-a-chip platform can give valuable information on SCPNs behavior in a more realistic setting.

MATERIALS & METHODS

SCPNs preparation

Lyophilized SCPNs synthesized by Linlin Deng (group of Anja Palmans, TUE) were dissolved in PBS (pH 7.4) inside a vial covered with aluminum foil. PBS (pH 7.4) was added on top of the powder at room temperature to a final concentration of 3 mg/mL. The vials were placed in an oven at 80° C for 10 min, then they were shaken by hand until complete dissolution and placed back in the oven for 10 min. Gently they were placed at room temperature, covered in aluminum foil and allowed to cool down overnight.

Cell culture

MCF7 breast cancer cell line was cultured in full DMEM media (Dulbecco's Modified Eagle Medium containing 4.5 g/L D-glucose, L-glutamine and pyruvate, from Thermo Fisher), with 10% FBS (Gibco, ThermoFisher), heat inactivated. 1% penicillin/streptomycin (Biowest) was added to cell media. For cell detachment, trypsin 25% EDTA (ThermoFisher) was used. MCF7 cells were seeded in ultra-low-attachment U-shaped 96-well plates (Corning) as 1000 cells/well and allowed to grow for 24h at 37° C 5% CO_2 before being added to the chip.

Chip preparation

ECM gel from Engelbreth-Holm-Swarm murine sarcoma cells (Sigma Aldrich) was thawed at 4° C overnight. On ice, the gel was diluted 2x in full DMEM (10% FBS), to a final protein concentration of 5.25 mg/mL, then added to the middle channel of the DAX-1 chip (AIM Biotech). The chip was placed on two PDMS supports of 1 cm height inside a Petri Dish sealed with Parafilm and allowed to gelate for 15-20 min at 37° C 5% CO_2. For the chip side channel, a collagen solution was prepared according to AIM Biotech general protocol v5.3. In brief, collagen type I from rat tail acid solution (Corning) for a final concentration of 2.5 mg/mL was mixed on ice with Phenol Red in PBS 10x (pH 7.4) (Sigma Aldrich) as 10% v/v, then the pH was adjusted to 7.4 (faint pink color) using NaOH 0.5N (pellets from PanReac dissolved in MilliQ water). Hyaluronic acid from rooster comb (as sodium salt, from Sigma Aldrich, dissolved in MilliQ water) was added for a final concentration of 0.8 mg/mL. Then, pre-formed MCF7 spheroids were gathered from the ultra-low-attachment 96-well plate, centrifuged gently (5 min at 200 g) and resuspended using the gel mix. The right side-channel of the chip was filled with the spheroid collagen-HA mix and was allowed to gelate for 30 min at 37° C 5% CO_2 inside a Parafilm-sealed Petri Dish. After gelation, SCPNs solution (in PBS) diluted 2x in full DMEM (10% FBS) to 1.5 mg/mL was added to the left side-channel of the chip and to the corresponding media reservoirs. The solution was allowed to diffuse overnight inside the chip at 37° C 5% CO_2.

Confocal microscopy

SCPNs in chip were imaged using a Zeiss LSM 780 confocal microscope, built on an inverted XYZ motorized Zeiss Axio Observer Z1. A wide-lens 40x water immersion objective (C-Apochromat/VIS-IR/

Korr FCS/Korr 0.13-0.17), NA 1.2, was used together with a thermal chamber for incubation at 37° C. HEPES buffer (5%) was added in the chip to avoid pH changes. Imaging and partial image analysis were performed using LSM Zen Black 2.1 software. Further image adjustments were performed using Fiji ImageJ.[24]

FRAP

A circle of 17.5 μm in diameter was used as a bleach region in the center of a 100 μm x 25 μm rectangular image. Bleaching was performed with 561 nm laser at 100% laser power using 20 iterations. Fluorescence recovery was measured for 1 min at a frame rate of 40 ms/frame, including 10 frames pre-bleach.

Text files were exported from LSM Zen Black software containing fluorescence intensity in the bleach region and in the whole image. FRAP data was analysed using the online tool easyFRAP.[25,26] EasyFRAP requires as input the mean intensity along time in three areas: the bleach area, the "whole cell" and the "background". We used the whole image as "whole cell", except for measurements next to spheroid, where very dark or very bright areas corresponding to the spheroid itself were manually excluded. For "background" we used the first value after bleach, making the assumption that bleach was complete. Double normalized curves were exported from easyFRAP and plotted in GraphPad Prism (GraphPad Software, San Diego, California, USA). A one-component exponential curve was fitted to obtain a more accurate halftime, using "Y_0" constrained to "0". Halftimes ($\tau_{1/2}$) were then used in a simplified diffusion equation from Soumpasis et al.[27] to calculate the diffusion constant: $D = 0.224 \cdot r_n^2 / \tau_{1/2}$, where r_n is the nominal bleach radius and 0.224 is a coefficient numerically determined for aqueous environment.

Spectral imaging

For spectral imaging, the LSM780 system contained three internal detectors, two PMTs and a 32 PMT GaAsP array. We used a detection interval between 565 and 700 nm with binning into 15 channels. The sample was excited with 561nm DPSS laser at 2% power. From the resulting image, for quantifying the spectral signal, 10 small circles were drawn into each compartment of interest. Mean and individual curves of fluorescence intensity were plotted using GraphPad Prism. Figures were assembled in Adobe Illustrator.

REFERENCES

(1)   Karki, S.; Gohain, M. B.; Yadav, D.; Ingole, P. G. Nanocomposite and Bio-Nanocomposite Polymeric Materials/Membranes Development in Energy and Medical Sector: A Review. *International Journal of Biological Macromolecules* **2021**, *193*, 2121–2139. https://doi.org/10.1016/j.ijbiomac.2021.11.044.

(2)   Hickey, J. W.; Santos, J. L.; Williford, J.-M.; Mao, H.-Q. Control of Polymeric Nanoparticle Size to Improve Therapeutic Delivery. *Journal of Controlled Release* **2015**, *219*, 536–547. https://doi.org/10.1016/j.jconrel.2015.10.006.

(3)   Cao, S.; Shao, J.; Xia, Y.; Che, H.; Zhong, Z.; Meng, F.; van Hest, J. C. M.; Abdelmohsen, L. K. E. A.; Williams, D. S. Molecular Programming of Biodegradable Nanoworms via Ionically Induced Morphology Switch toward Asymmetric Therapeutic Carriers. *Small* **2019**, *15* (38), 1901849. https://doi.org/10.1002/smll.201901849.

(4)   Feng, L.; Zhu, C.; Yuan, H.; Liu, L.; Lv, F.; Wang, S. Conjugated Polymer Nanoparticles: Preparation, Properties, Functionalization and Biological Applications. *Chem. Soc. Rev.* **2013**, *42* (16), 6620. https://doi.org/10.1039/c3cs60036j.

(5)   Hamelmann, N. M.; Paulusse, J. M. J. Single-Chain Polymer Nanoparticles in Biomedical Applications. *Journal of Controlled Release* **2023**, *356*, 26–42. https://doi.org/10.1016/j.jconrel.2023.02.019.

(6)   Liu, Y.; Pujals, S.; Stals, P. J. M.; Paulöhrl, T.; Presolski, S. I.; Meijer, E. W.; Albertazzi, L.; Palmans, A. R. A. Catalytically Active Single-Chain Polymeric Nanoparticles: Exploring Their Functions in Complex Biological Media. *J. Am. Chem. Soc.* **2018**, *140* (9), 3423–3433. https://doi.org/10.1021/jacs.8b00122.

(7)   Collot, M.; Schild, J.; Fam, K. T.; Bouchaala, R.; Klymchenko, A. S. Stealth and Bright Monomolecular Fluorescent Organic Nanoparticles Based on Folded Amphiphilic Polymer. *ACS Nano* **2020**, *14* (10), 13924–13937. https://doi.org/10.1021/acsnano.0c06348.

(8)   Aiertza, M. K.; Odriozola, I.; Cabañero, G.; Grande, H.-J.; Loinaz, I. Single-Chain Polymer Nanoparticles. *Cell. Mol. Life Sci.* **2012**, *69* (3), 337–346. https://doi.org/10.1007/s00018-011-0852-x.

(9)   Li, S.-D.; Huang, L. Pharmacokinetics and Biodistribution of Nanoparticles. *Mol. Pharmaceutics* **2008**, *5* (4), 496–504. https://doi.org/10.1021/mp800049w.

(10)   Liu, C.; Jiang, X.; Gan, Y.; Yu, M. Engineering Nanoparticles to Overcome the Mucus Barrier for Drug Delivery: Design, Evaluation and State-of-the-Art. *Medicine in Drug Discovery* **2021**, *12*, 100110. https://doi.org/10.1016/j.medidd.2021.100110.

(11) Sykes, E. A.; Dai, Q.; Sarsons, C. D.; Chen, J.; Rocheleau, J. V.; Hwang, D. M.; Zheng, G.; Cramb, D. T.; Rinker, K. D.; Chan, W. C. W. Tailoring Nanoparticle Designs to Target Cancer Based on Tumor Pathophysiology. *Proc. Natl. Acad. Sci. U.S.A.* **2016**, *113* (9). https://doi.org/10.1073/pnas.1521265113.

(12) Kröger, A. P. P.; Paulusse, J. M. J. Single-Chain Polymer Nanoparticles in Controlled Drug Delivery and Targeted Imaging. *Journal of Controlled Release* **2018**, *286*, 326–347. https://doi.org/10.1016/j.jconrel.2018.07.041.

(13) Cheng, C.-C.; Huang, S.-Y.; Fan, W.-L.; Lee, A.-W.; Chiu, C.-W.; Lee, D.-J.; Lai, J.-Y. Water-Soluble Single-Chain Polymeric Nanoparticles for Highly Selective Cancer Chemotherapy. *ACS Appl. Polym. Mater.* **2021**, *3* (1), 474–484. https://doi.org/10.1021/acsapm.0c01220.

(14) Bajj, D. N. F.; Tran, M. V.; Tsai, H.-Y.; Kim, H.; Paisley, N. R.; Algar, W. R.; Hudson, Z. M. Fluorescent Heterotelechelic Single-Chain Polymer Nanoparticles: Synthesis, Spectroscopy, and Cellular Imaging. *ACS Appl. Nano Mater.* **2019**, *2* (2), 898–909. https://doi.org/10.1021/acsanm.8b02149.

(15) Sathyan, A.; Croke, S.; Pérez-López, A. M.; de Waal, B. F. M.; Unciti-Broceta, A.; Palmans, A. R. A. Developing Pd(II) Based Amphiphilic Polymeric Nanoparticles for pro-Drug Activation in Complex Media. *Mol. Syst. Des. Eng.* **2022**, *7* (12), 1736–1748. https://doi.org/10.1039/D2ME00173J.

(16) Chen, J.; Wang, J.; Bai, Y.; Li, K.; Garcia, E. S.; Ferguson, A. L.; Zimmerman, S. C. Enzyme-like Click Catalysis by a Copper-Containing Single-Chain Nanoparticle. *J. Am. Chem. Soc.* **2018**, *140* (42), 13695–13702. https://doi.org/10.1021/jacs.8b06875.

(17) Zhang, Y.; Tan, R.; Gao, M.; Hao, P.; Yin, D. Bio-Inspired Single-Chain Polymeric Nanoparticles Containing a Chiral Salen Ti [IV] Complex for Highly Enantioselective Sulfoxidation in Water. *Green Chem.* **2017**, *19* (4), 1182–1193. https://doi.org/10.1039/C6GC02743A.

(18) ter Huurne, G. M.; de Windt, L. N. J.; Liu, Y.; Meijer, E. W.; Voets, I. K.; Palmans, A. R. A. Improving the Folding of Supramolecular Copolymers by Controlling the Assembly Pathway Complexity. *Macromolecules* **2017**, *50* (21), 8562–8569. https://doi.org/10.1021/acs.macromol.7b01769.

(19) Huurne, G. M. ter; Palmans, A. R. A.; Meijer, E. W. Supramolecular Single-Chain Polymeric Nanoparticles. *CCS Chem* **2019**, 64–82. https://doi.org/10.31635/ccschem.019.20180036.

(20) Deng, L.; Albertazzi, L.; Palmans, A. R. A. Elucidating the Stability of Single-Chain Polymeric Nanoparticles in Biological Media and Living Cells. *Biomacromolecules* **2022**, *23* (1), 326–338. https://doi.org/10.1021/acs.biomac.1c01291.

(21) Chen, J.; Wang, J.; Li, K.; Wang, Y.; Gruebele, M.; Ferguson, A. L.; Zimmerman, S. C. Polymeric "Clickase" Accelerates the Copper Click Reaction of Small Molecules, Proteins, and Cells. *J. Am. Chem. Soc.* **2019**, *141* (24), 9693–9700. https://doi.org/10.1021/jacs.9b04181.

(22) Hamelmann, N. M.; Paats, J.-W. D.; Paulusse, J. M. J. Cytosolic Delivery of Single-Chain Polymer Nanoparticles. *ACS Macro Lett.* **2021**, *10* (11), 1443–1449. https://doi.org/10.1021/acsmacrolett.1c00558.

(23) Deye, J. F.; Berger, T. A.; Anderson, A. G. Nile Red as a Solvatochromic Dye for Measuring Solvent Strength in Normal Liquids and Mixtures of Normal Liquids with Supercritical and near Critical Fluids. *Anal. Chem.* **1990**, *62* (6), 615–622. https://doi.org/10.1021/ac00205a015.

(24) Schindelin, J.; Arganda-Carreras, I.; Frise, E.; Kaynig, V.; Longair, M.; Pietzsch, T.; Preibisch, S.; Rueden, C.; Saalfeld, S.; Schmid, B.; Tinevez, J.-Y.; White, D. J.; Hartenstein, V.; Eliceiri, K.; Tomancak, P.; Cardona, A. Fiji: An Open-Source Platform for Biological-Image Analysis. *Nat Methods* **2012**, *9* (7), 676–682. https://doi.org/10.1038/nmeth.2019.

(25) Rapsomaniki, M. A.; Kotsantis, P.; Symeonidou, I.-E.; Giakoumakis, N.-N.; Taraviras, S.; Lygerou, Z. EasyFRAP: An Interactive, Easy-to-Use Tool for Qualitative and Quantitative Analysis of FRAP Data. *Bioinformatics* **2012**, *28* (13), 1800–1801. https://doi.org/10.1093/bioinformatics/bts241.

(26) Koulouras, G.; Panagopoulos, A.; Rapsomaniki, M. A.; Giakoumakis, N. N.; Taraviras, S.; Lygerou, Z. EasyFRAP-Web: A Web-Based Tool for the Analysis of Fluorescence Recovery after Photobleaching Data. *Nucleic Acids Research* **2018**, *46* (W1), W467–W472. https://doi.org/10.1093/nar/gky508.

(27) Soumpasis, D. M. Theoretical Analysis of Fluorescence Photobleaching Recovery Experiments. *Biophys J* **1983**, *41* (1), 95–97.

(28) ter Huurne, G. M.; de Windt, L. N. J.; Liu, Y.; Meijer, E. W.; Voets, I. K.; Palmans, A. R. A. Improving the Folding of Supramolecular Copolymers by Controlling the Assembly Pathway Complexity. *Macromolecules* **2017**, *50* (21), 8562–8569. https://doi.org/10.1021/acs.macromol.7b01769.

(29) Shahkaramipour, N.; Tran, T. N.; Ramanan, S.; Lin, H. Membranes with Surface-Enhanced Antifouling Properties for Water Purification. *Membranes (Basel)* **2017**, *7* (1), 13. https://doi.org/10.3390/membranes7010013.

(30) Patra, M.; Awuah, S. G.; Lippard, S. J. Chemical Approach to Positional Isomers of Glucose-Platinum Conjugates Reveals Specific Cancer Targeting through Glucose-Transporter-Mediated Uptake in Vitro and in Vivo. *J Am Chem Soc* **2016**, *138* (38), 12541–12551. https://doi.org/10.1021/jacs.6b06937.

(31) Hosono, N.; A. Palmans, A. R.; W. Meijer, E. "Soldier–Sergeant–Soldier" Triblock Copolymers: Revealing the Folded Structure of Single-Chain Polymeric Nanoparticles. *Chemical Communications* **2014**, *50* (59), 7990–7993. https://doi.org/10.1039/C4CC02789B.

(32) Tomasetti, L.; Liebl, R.; Wastl, D. S.; Breunig, M. Influence of PEGylation on Nanoparticle Mobility in Different Models of the Extracellular Matrix. *European Journal of Pharmaceutics and Biopharmaceutics* **2016**, *108*, 145–155. https://doi.org/10.1016/j.ejpb.2016.08.007.

(33) Pilz, M.; Kwapiszewska, K.; Kalwarczyk, T.; Bubak, G.; Nowis, D.; Hołyst, R. Transport of Nanoprobes in Multicellular Spheroids. *Nanoscale* **2020**, *12* (38), 19880–19887. https://doi.org/10.1039/d0nr01986k.

(34) Schmeichel, K. L.; Bissell, M. J. Modeling Tissue-Specific Signaling and Organ Function in Three Dimensions. *Journal of Cell Science* **2003**, *116* (12), 2377–2388. https://doi.org/10.1242/jcs.00503.
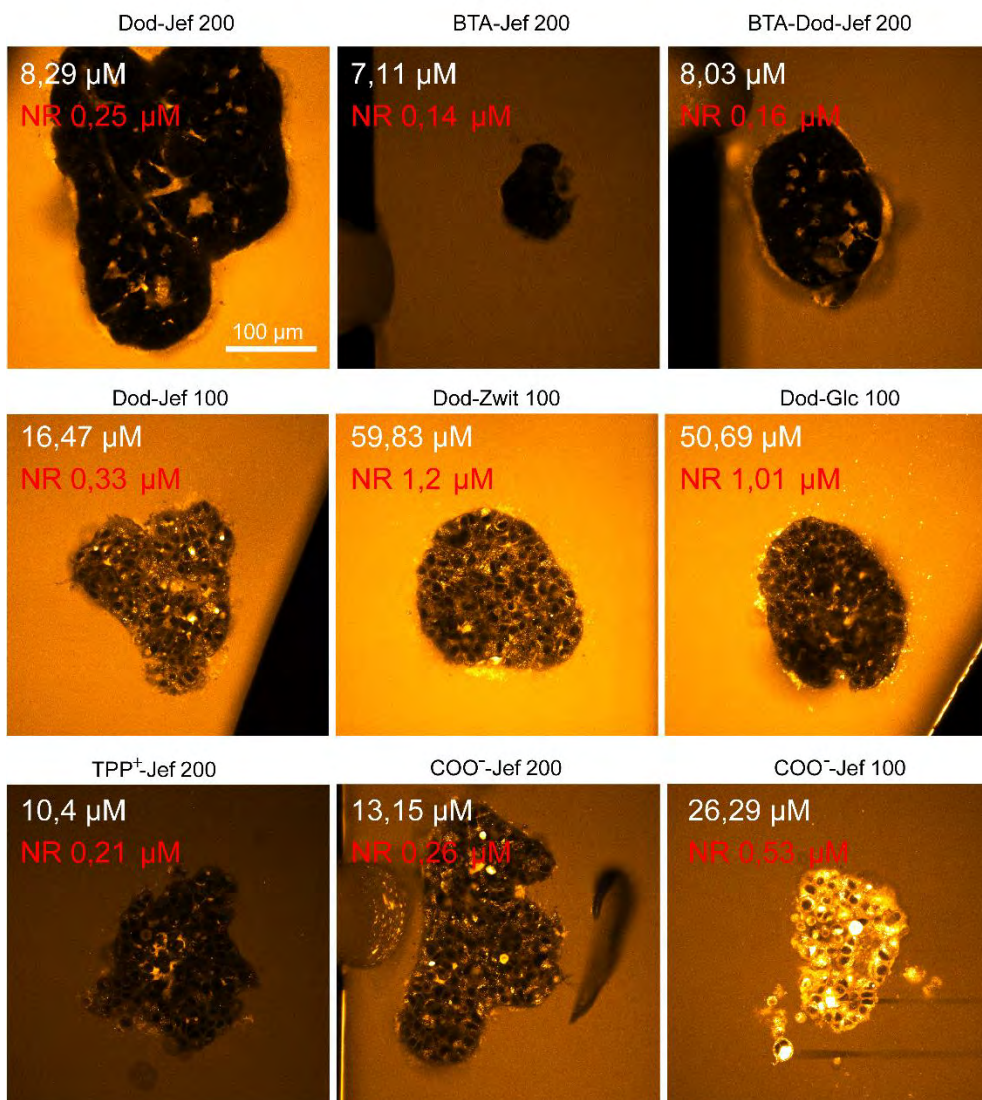
Supplementary figure 4.1. MCF7 spheroid uptake with calculated molar concentrations and partial Nile Red concentration ("NR") for each polymer. Mass concentration was kept constant at 1.5 mg/mL. Scale bar is 100 µm.
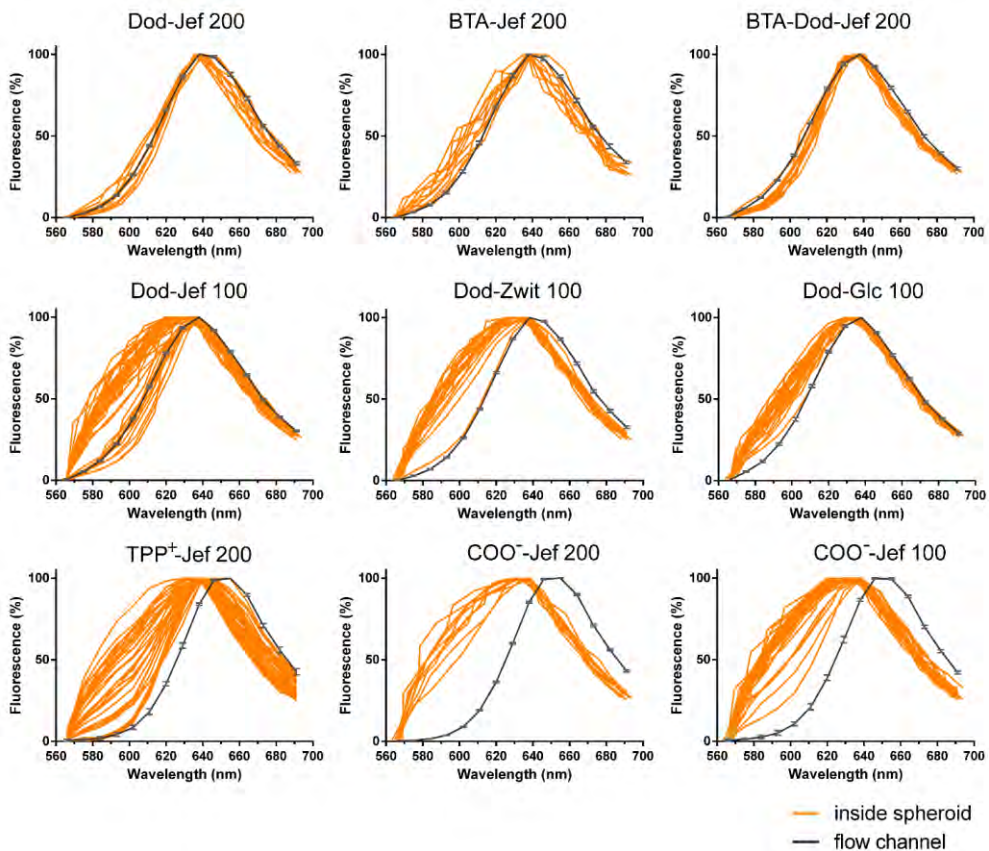
Supplementary figure 4.2. SCPNs spectra of Nile Red fluorescence shown as individual localized measurements

Conclusions and Future Perspectives

In this thesis we have addressed the need for nanocarrier testing platforms by proposing a simple microfluidic chip combined with smart imaging techniques for assessing nanocarrier interactions inside tumor tissue. The platform addresses both the passage through the extracellular matrix and the cellular uptake in a 3D setting, highlighting the importance of addressing both of them in the rational design of nanocarriers. Furthermore, we propose the use of fluorescence reporter tools and imaging techniques such as spectral imaging, FRET and FRAP as important tools in assessing the local stability and mobility of nanocarriers.

Before delving into more complex environments, we performed a thorough analysis of a set of polymeric micelles, focusing on their stability and interactions inside biological media. We compared three widely used hydrophilic shells (PEtOx, PEG and PAA), together with two lengths of a dendritic hydrophobic core for assessing their effect onto micellar properties. Among the three polymers, PAA-based micelles were the most unstable in the presence of BSA, while PEtOx and PEG had similar stability. Furthermore, BSA experiments showed the stabilizing effect of the longer dendritic core, while basic micelle properties such as size and CMCs remained very similar for the two dendron types.

Cellular uptake in 2D HeLa cultures revealed important differences in internalization behavior: the PAA amphiphiles localized mostly onto cellular membranes and had an increased uptake over the other two, which localized in endocytic vesicles. The hydrophobic end also affected cellular uptake – the higher stability of the nonyl amphiphiles correlated with lower internalization.

Furthermore, we performed disencapsulation experiments using a hydrophobic dye as drug model. Intriguingly, increased micellar stability does not imply slower cargo release. Instead, the cargo leakage from formed micelles of PEtOx and PEG was faster compared to the release PAA micelle disassembly, revealing the crucial role played the hydrophilic moiety into the micellar packing of hydrophobic dugs.

Then, micelle characterization was taken further through the development of a simple microfluidic chip containing two types of ECM (basal lamina and collagen with hyaluronic acid as „tumor ECM") and breast cancer MCF7 spheroids. The chip setup was validated, showing clear delimitation of the component gels and good cellular viability. Inside the chip, different micelle interactions were observed in basal lamina, from binding for PAA-based amphiphiles to avoidance of ECM structure for the more stable nonyl micelles of PEtOx and PEG. However, ECM interactions were only transient, as shown by FRAP measurements. PAA also had the highest cellular uptake into MCF7 spheroids. For this reason, we continued the study with a more stable tri-

block copolymer design, which hinted that mobility through ECM is partly based on unimer exchange.

In the last chapter, single chain polymeric nanoparticles were tested inside the chip using Nile Red as fluorescence reporter for the particle folding state. The SCPNs library was very stable through ECM passage. However, spheroid uptake differed, being very low for the more hydrophobic polymers and showing a consistent increase for the hydrophilic and charged polymers. Interestingly, charged SCPNs did not interact with ECM structure, while being well uptaken by cells, which suggests that SCPNs folding has a shielding effect which allows fast passage through the tissue.

In the context of the THERACAT consortium, the current work is only the basis on which further investigations can be conducted. A highly interesting aspect for future experiments is the nanocatalyst activity in the dual-ECM chip, for instance by using „implantable" nanocatalysts in the collagen channel and adding an activatable prodrug or prodye to the flow channel. Such experiments can improve our understanding of the requirements needed for the nanocarrier and nanocatalyst to meet in the highly complex tumor environment.

Furthermore, the consortium has the advantage of bringing together an array of different nanocarrier and nanocatalyst types, which are otherwise difficult to compare on their own. Through our testing platform they become comparable in their ability to cross different ECM types and to be uptaken by the cells. In future experiments we expect to add several nanocarrier types besides polymeric micelles and SCPNs. This is a general drawback in nanocarrier research, which can be tackled by implementing more standardized testing platforms mimicking various aspects of the tumor microenvironment.

On the other hand, the medical field currently progresses towards personalized medicine, with higher specificity diagnosis, as well as more specialized nano-drug formulations. In this sense, it is a logical step to design specialized lab-on-a-chip testing platforms for nanocarrier development. For example, in our case the MCF7 spheroids in the chip can be replaced by triple-negative breast cancer cells 4T1 or EMT6 for a more disease-specific result. Another improvement point would be to include testing nanocarrier mobility inside spheroid-secreted ECM which occurs naturally inside and around the spheroid, but which requires an adaptation of the testing method to smaller volume, for instance by using FCS.

All in all, our platform mimicking the tumor ECM is versatile enough to adapt for testing different nanocarrier types and more specific disease models, while remaining simple enough for a relatively fast experimental preparation.

List of Publications

Published:

- Slor G, Olea AR, Pujals S, Tigrine A, De La Rosa VR, Hoogenboom R, Albertazzi L, Amir RJ. *Judging Enzyme-Responsive Micelles by Their Covers: Direct Comparison of Dendritic Amphiphiles with Different Hydrophilic Blocks.* Biomacromolecules. 2021 Mar 8;22(3):1197-1210. doi: 10.1021/acs.biomac.0c01708.

In preparation:

- <u>Alis R. Olea</u>, <u>Alicia Jurado</u>, Gadi Slor, Shahar Tevet, Silvia Pujals, Roey Amir, Lorenzo Albertazzi, *Reaching the tumour: mobility of polymeric micelles inside an in vitro tumor-on-a-chip model with dual ECM* (2023)
- <u>Linlin Deng</u>, <u>Alis R. Olea</u>, Silvia Pujals, Anja Palmans, Lorenzo Albertazzi, *Imaging dynamics and stability of single-chain polymeric nanoparticles in a multi-gel tumor-on-a-chip* (2023)

Previous to PhD work:

- Feiner-Gracia N, Olea RA, Fitzner R, El Boujnouni N, van Asbeck AH, Brock R, Albertazzi L. *Super-resolution Imaging of Structure, Molecular Composition, and Stability of Single Oligonucleotide Polyplexes.* Nano Lett. 2019 May 8;19(5):2784-2792. doi: 10.1021/acs.nanolett.8b04407.
- Baranov MV, Olea RA, van den Bogaart G. *Chasing Uptake: Super-Resolution Microscopy in Endocytosis and Phagocytosis.* Trends Cell Biol. 2019 Sep;29(9):727-739. doi: 10.1016/j.tcb.2019.05.006.
- Wallbrecher R, Ackels T, Olea RA, Klein MJ, Caillon L, Schiller J, Bovée-Geurts PH, van Kuppevelt TH, Ulrich AS, Spehr M, Adjobo-Hermans MJW, Brock R. *Membrane permeation of arginine-rich cell-penetrating peptides independent of transmembrane potential as a function of lipid composition and membrane fluidity.* J Control Release. 2017 Jun 28;256:68-78. doi: 10.1016/j.jconrel.2017.04.013.

List of acronyms and abbreviations

5FU: 5-fluorouracil

7-DEAC: 7-(diethylamino)coumarin-3-carboxylic acid

BOOM: bioorthogonal organometallic reactions

BSA: bovine serum albumin

BTA: benzene-1,3,5-tricarboxamide

CMC: critical micelle concentration

COOH: carboxylic acid

Cy3: cyanine 3

Cy5: cyanine 5

D: diffusion constant

DBC: di-block copolimer

DDS: drug delivery system

DMEM: Dulbecco's Modified Eagle Medium

Dod: n-dodecylamine

DP: degree of polymerization

ECM: extracellular matrix

EHS: Engelbreth-Holm-Swarm sarcoma

EPR: enhanced permeability and retention effect

ESID: electronically switchable illumination and detection module

FBS: fetal bovine serum

FCS: fluorescence correlation spectroscopy

FRAP: fluorescence recovery after photobleaching

FRET: fluorescence resonance energy transfer

Glc: D-(+)-Glucosamine

GLUT: glucose transporter

HA: hyaluronic acid

Hex: hexyl

HPLC: high-performance liquid chromatography

IFP: tumor interstitial fluid pressure

Jef: jeffamine

Non: nonyl

NPs: nanoparticles

OOAC: organ-on-a-chip

PAA: poly(acrylic acid)

PB: phosphate buffer

PBS: phosphate buffer saline

PDMS: polydimethylsiloxane

PEG: poly(ethylene glycol)

PEtOx: poly(2-ethyl-2-oxazoline)

PLE: porcine liver esterase

RHAMM: receptor for hyaluronan mediated motility

SCPNs: single-chain polymeric nanoparticles

SEM: standard error of the mean

SPT: single particle tracking

TBC: tri-block copolimer

TPP: (3-aminopropyl)triphenylphosphonium

VEGF: vascular endothelial growth factor

Zwit: zwitterion 4-((3-aminopropyl)dimethylammonio)butane-1-sulfonate

Acknowledgements

Now, to the earthly people...

I would like to thank first of all to my supervisors, both Lorenzo and Silvia, who supported me throughout this journey, who had patience with me, who guided me and offered their best feedback and personal example, and most of all believed in my potential even though sometimes I wasn't the most easy-to-supervise student (especially during the pandemics and afterwards). Grazie mille Lorenzo for taking me on this journey, with a super-nice grant, with a great team of people, and for helping me keep on track! Moltes gracies Silvia for your continous support, for useful advice and for being also for me the catalan mum.

I am very grateful for being part of the wonderful THERACAT team! It was super nice to meet all of you, I learned a lot and I hope to keep in touch in our future paths. It would have been nicer to have all the meetings in person, but life is unpredictable. In particular, thank you so much Linlin!! It was very nice collaborating with you! I wish that life will smile to you. Thank you Anja for being always nice and supportive. Many many thanks to Roey and Gadi for the very nice collaboration! Thank you Daniel and Africa for the enthusiastic collaborative ideas (which would have worked differently without the pandemics) and thank you all THERACATs and Rosa for the great experiences and science-driven discussions.

A big big THANK YOU to the Nanoscopy team! Madhura, Edgar, Teo, the last ones standing in Barcelona and the Eindhoven team, Roger, Manos, Laura, Ana, Marrit, Cristina and newcomers and students: Thank you all, guys! Madhura, you were the best peer and one of the most joyful persons I know. Thank you for all tea-time discussions, trecking and zumba classes! Edgar, thank you for being so helpful many times, for your always calm presence (and for the GoT prognostics discussions); I still think you can be a great professor. Thank you Teo, my fellow romanian, mulțumesc că mi-ai fost aproape de atât de multe ori! Thanks Adri for being so super-professional while in the lab and supportive mommy afterwards! Thanks Maria for

our shared memories (and milk) since I was a master student in the lab. Thanks Pietro for the physicist take on things and for the nice outings. Thank you Natalia, first for your encouragement to re-join the lab in the PhD position, for being the best supervisor before that and for your pioneering work in our group in every research aspect – you were a role-model for all of us. And from the students, thank you Kamila, Sofia and Gaia for the lovely times spent together. Alicia, my dear student, thank you – it was wonderful working with you! You reminded me why I like research ☺

Thank you to all IBEC staff (sorry for not naming you all, although you deserve it) for your constant work to keep things going smoothly and for your smile on the corridors! In the microscopy unit, thank you Judith for your helpful tips and thank you Elena Rebollo for the super-useful introduction in spectral microscopy in the csic.

Mulțumesc familiei mele pentru suport și înțelegere, în special lui Radu și lui Daria. Îi mulțmesc lui Tata Mare pentru nenumăratele discuții despre fenomenele biologice. Îi mulțumesc lui Nadi pentru aproape doi ani de babysitting, în care am reușit să finalizez teza.

Îi mulțumesc lui Claudiu Bratu care m-a călăuzit pe plan personal ca să pot trece peste vremuri grele și care m-a învățat că, cu sau fără doctorat, atunci când mergi la piață ești doar un cumpărător de castraveți.

Thank you all,

Alis

Funding Acknowledgements